

THE ZURICH ENVIRONMENTAL STUDY (*ZENS*)  
OF GALAXIES IN GROUPS ALONG THE COSMIC WEB. II.  
GALAXY STRUCTURAL MEASUREMENTS AND THE CONCENTRATION OF  
MORPHOLOGICALLY-CLASSIFIED SATELLITES IN DIVERSE ENVIRONMENTS<sup>†</sup>

A. CIBINEL<sup>1,\*</sup>, C. M. CAROLLO<sup>1,\*</sup>, S. J. LILLY<sup>1</sup>, F. MINIATI<sup>1</sup>, J. D. SILVERMAN<sup>2</sup>, J. H. VAN GORKOM<sup>3</sup>, E. CAMERON<sup>1</sup>, A. FINOGENOV<sup>4</sup>, P. NORBERG<sup>5</sup>, A. PIPINO<sup>1</sup>, C. S. RUDICK<sup>1</sup>, T. LU<sup>1</sup>, Y. PENG<sup>1</sup>

SUBMITTED TO APJ

ABSTRACT

We present structural measurements of galaxies in the  $z \sim 0.06$  groups investigated in the *Zurich Environmental Study* (*ZENS*), a program aimed at establishing how galaxy properties in the local Universe depend on four different environmental parameters. Galaxy structure is quantified both non-parametrically and parametrically, through modeling of the two-dimensional surface brightness profiles of the galaxies. Structural parameters are also derived for main subgalactic components, i.e., bulges, disks and bars. We calibrate all parametric and non-parametric structural measurements on a common grid, correcting for observational biases due to PSF blurring and surface brightness effects as a function of galaxy size, magnitude, steepness of radial light profile and ellipticity. We use the galaxy bulge-to-total ratios, in combination with the calibrated non-parametric structural estimators, to implement a quantitative morphological classification scheme that maximizes purity in the resulting morphological samples. These structural measurements will be used for a number of scientific studies. In this paper, we focus on how the concentration  $C$  of *satellite* galaxies depends on galaxy mass for each separate Hubble type, and on group halo mass, group-centric distance and large-scale structure density. At galaxy masses  $M \geq 10^{10} M_{\odot}$ , the concentration of disk satellites is found to increase, with increasing stellar mass, separately within each morphological bin of bulge-to-total ratio, implying that the known increase in concentration with increasing stellar mass for disk satellites is due, at least in part, to an increase in galaxy central stellar density at constant bulge-to-total ratio. The correlation between concentration and galaxy stellar mass becomes progressively steeper for later morphological types. Disk-satellite concentration shows no significant dependence on either large-scale structure density or projected group-centric distance. In contrast, at constant galaxy stellar mass above  $10^{10} M_{\odot}$ , the mass of the group halo appears to have an impact on the concentration of disk-dominated satellites being 10% more concentrated in  $M_{\text{GROUP}} > 10^{13.4} M_{\odot}$  groups than similar galaxies in lower mass groups.

*Subject headings:* surveys - galaxies: groups - galaxies: formation - galaxies: evolution - galaxies: structure

1. INTRODUCTION

We present the methodology used to derive structural measurements for the galaxies investigated in the *Zurich Environmental Study* (*ZENS*) (Carollo et al. 2012, hereafter Paper I). This paper specifically reports the application of the adopted methodology to the first-epoch data for 769 galaxies in 79 of the total 141 *ZENS* groups. The resulting measurements are published in the *ZENS* global catalog that we have published electronically in Paper I.

*ZENS* is designed to address the question of what environmental scale is most relevant for influencing the properties of different galaxy populations. Several definitions of environment have been commonly employed in the literature to study the relation between environment and galaxy evolution: the density of galaxies calculated out to a fixed or an adaptive distance (e.g. Dressler 1980; Hogg et al. 2003; Cooper et al. 2005; Baldry et al. 2006), the mass of the host group or cluster (Weinmann et al. 2006; Kimm et al. 2009), the distance from the group/cluster center (Whitmore & Gilmore 1991; Balogh et al. 1997; Lewis et al. 2002; De Propris et al. 2003; Hansen et al. 2009) or the location into larger structures such as cosmic filaments or superclusters (Einasto et al. 2007; Porter et al. 2008). Recently, the ability to separate galaxies into centrals and satellites within their host group halos has produced mounting evidence that the environmental influence on the star-formation properties of galaxies may peak for *satellite* galaxies (van den Bosch et al. 2008; Peng et al. 2010, 2012); in fact, these studies suggest that most of the environmental effects observed as a function of other environmental quantities may be ascribed to a mixture of affected satellites and unaffected centrals. Key questions are how the different definitions

\* E-mail: cibinel@phys.ethz.ch, marcella@phys.ethz.ch

<sup>1</sup> Institute of Astronomy, ETH Zurich, CH-8093 Zurich, Switzerland

<sup>2</sup> Institute for the Physics and Mathematics of the Universe (IPMU), University of Tokyo, Kashiwa-shi, Chiba 277-8568, Japan

<sup>3</sup> Department of Astronomy, Columbia University, New York, NY 10027, USA

<sup>4</sup> Max-Planck-Institut für extraterrestrische Physik, D-84571 Garching, Germany

<sup>5</sup> Institute for Computational Cosmology, Department of Physics, Durham University, South Road, Durham DH1 3LE, UK

<sup>†</sup> Based on observations collected at the European Southern Observatory, La Silla Chile. Program ID 177.A-0680

of environment relate to one another, and what is their relative importance for different galaxy populations (e.g. Blanton & Berlind 2007; Wilman et al. 2010; Peng et al. 2012; Muldrew et al. 2012; Woo et al. 2012).

In our ZENS effort, we aim at helping clarifying which of the many environments that a galaxy experience has a larger impact on its evolution. We do so by using the same sample of suitably selected nearby galaxies to investigate the dependence of their properties, at fixed stellar mass, on four environment measurements: the host group halo mass, the radial segregation within the group, the large scale density field on which the group halos reside, and the galaxy rank within its group halo, i.e., whether it is the central or a satellite galaxy within the gravitational potential of its host group.

This paper focuses on the quantification of robust galaxy structural and morphological properties, which provide key information on the life histories of galaxies. The presence and properties of massive disks and spheroids highlight the occurrence of relatively slow and dissipative gas accretion (White & Rees 1978; Fall & Efstathiou 1980) or mergers (e.g. Toomre 1977; Barnes 1988; Schweizer et al. 1990; Naab & Burkert 2003), respectively. Inner cores or cusps (Ferrarese et al. 1994; Lauer et al. 1995; Carollo et al. 1997a,b; Côté et al. 2007; Kormendy et al. 2009) and tidal debris (Malin & Carter 1980, 1983; Forbes & Thomson 1992; van Dokkum 2005; Tal et al. 2009; Janowiecki et al. 2010) also trace the degree of dissipation involved in the evolution of galaxies (not surprisingly with some debate, Mihos & Hernquist 1994, 1996; Kawata et al. 2006; Feldmann et al. 2008; Hopkins et al. 2009). Bars and pseudo-bulges are smoking guns for either secular evolution processes (Kormendy 1979; Combes et al. 1990; Courteau et al. 1996; Norman et al. 1996; Wyse et al. 1997; Carollo 1999; Carollo et al. 1997c, 1998, 2001; Debattista et al. 2004, 2006; Kormendy & Kennicutt 2004; Fisher & Drory 2008), or possibly for early bulge formation through instabilities in the proto-disks (Immeli et al. 2004; Carollo et al. 2007; Dekel et al. 2009a,b). A robust determination of galaxy morphology and of its link to the surrounding environment is hence of paramount importance to the understanding of which physical processes drive galaxy evolution.

Determining galaxy structure is however notoriously not a trivial task. Visual morphological classification is still a widely adopted method (e.g. Lintott et al. 2008; Nair & Abraham 2010), despite its subjectivity and failure to provide quantitative measurements for different components, which are necessary to trace galaxy assembly over cosmic time. For these reasons numerous publications have been devoted to the development of methods and software for the automated quantification of structure on large galaxy samples. There are a number of approaches to the problem which can be broadly divided into two categories: those which employ parametric descriptors for the galaxy morphology, namely a set of analytical profiles used to model the bulge, disk, or bar component (e.g. Simard et al. 2002; Peng et al. 2002; de Souza et al. 2004) and those which instead use the observed properties of the light distribution, such as the degree of asymmetry, isolation of bright pixels or decompositions into a set of basis functions (e.g. Abraham et al. 1996; Conselice 2003; Refregier 2003; Lotz et al. 2004; Scarlata et al. 2007). The two methods have different

strengths: parametric decomposition is useful to obtain measurements of characteristic sizes and to have an estimate of the relative importance of the bar, disk and bulge components; it also easily includes the effects of seeing. Non-parametric estimators well describe the inhomogeneities in the light distributions of real galaxies, which typically display irregular, non axis-symmetric features generated by recent star-formation, dust or galaxy interactions.

Both parametric and non-parametric measurements suffer however from a number of observational biases, which must be corrected for in order to perform comparisons between galaxies of different properties, and observed in different conditions. In particular, in ground-based surveys, the effect of atmospheric seeing is one of the major complications. Several studies have shown the strong impact of the seeing on the photometric and structural properties of galaxies, not only in the inner regions of galaxies, but also out to several radii corresponding several FWHM of the Point Spread Function (PSF) (e.g. Schweizer 1979; Franx et al. 1989; Saglia et al. 1993; Trujillo et al. 2001; Graham 2001).

Another factor which affects the derivation of structural parameters is the inclination angle at which a galaxy is observed. The overlap, in projection, of multiple subcomponents, as well as physical factors such as the non-uniform distribution of inter-stellar dust – which causes a higher attenuation of short-wavelength light in the central regions of edge-on galaxies than in similar face-on galaxies (e.g. Driver et al. 2007; Shao et al. 2007) – can substantially bias the measurements of sizes, bulge-to-disk ratios, concentration and even stellar masses (e.g., Maller et al. 2009; Graham & Worley 2008; Bailin & Harris 2008).

Finally, the background sky makes the detection of faint components difficult, a fact which introduces severe biases in the measurements of the galaxy properties, especially magnitudes and sizes (e.g. Disney 1976; Impey & Bothun 1997). The strength of the bias depends on galaxy size, inclination and stellar light profile. Although a number of widely-used measurement techniques, such as the computation of Kron aperture fluxes (Kron 1980) or the extrapolation of model galaxy surface brightness profiles (Sersic 1968), can help recover light below the isophotal limit, significant systematic biases remain in the low surface brightness regimes specific to each survey (e.g. Graham et al. 2005; Cameron & Driver 2007, 2009; Häussler et al. 2007).

In ZENS we attempt *to correct*, when possible, all measurements of galaxy structure for systematic biases as a function of PSF-size, and also galaxy magnitude, size, axis ratio and radial shape of the light profile. We also quantify the size of systematic biases in regimes of parameter space where the (statistical) recovery of the intrinsic information is not achievable, e.g., at small galaxy sizes and low surface brightnesses.

The paper is organized as follows. In Section 2 we briefly review the specifications and definitions for the four environments under scrutiny in ZENS. We then devote the first part of the paper to an overview of the structural measurements carried out on the ZENS galaxy sample. These measurements include isophotal analyses and bar detection/quantification (Section 3), analytical surface brightness fits and bulge+disk decompositions

(Section 4), and derivation of non-parametric structural indices (concentration, Gini, asymmetry,  $M_{20}$ , smoothness; Section 5). In Section 6 we thoroughly investigate the sources of error in these measurements and derive a correction scheme that recovers the intrinsic structural parameters. In Section 7 we present the morphological classification of the ZENS galaxies, based on a quantitative partition of the structural parameter space in regions that are associated with elliptical, bulge-dominated disks, intermediate bulge-to-total ratio disks, late-type disks and irregular galaxies. In the same Section we also discuss the statistics of the structural properties for the various morphological classes. Appendices A-B present additional details on the tests performed on the analytical surface-brightness fits and supplementary information for the derivation of the corrections for the structural parameters. Stamp images for galaxies in the different morphological classes are found in Appendix C. In the final part of the paper we use the corrected structural measurements to study, at constant stellar mass, the concentration of satellite galaxies as a function of Hubble type and environment (Section 8). We summarize the paper in Section 9.

This second ZENS publication is complemented by a companion paper (Cibinel et al. 2012a, hereafter Paper III), in which we present the photometric properties of our galaxy sample and to which we refer for details on, e.g., the derivation of galaxy stellar masses that we use in this and other ZENS papers. The effects of local and large scale environments on central and satellite galaxies are explored in a series of forthcoming papers based on the ZENS database: in Lu et al. 2012 (Paper IV) we study the variation of morphology and star-formation activity in satellite galaxies across the different environments; Rudick et al. 2012a (Paper V) focuses on the resolved colors of bulges and disks for central and satellite galaxies; an analysis of the properties of the ZENS merging systems is discussed in Pipino et al. 2012 (Paper VI); the impact of environmental effect on the radial profiles of disk galaxies is presented Rudick et al. 2012b, (Paper VII); in Cibinel et al. 2012b (Paper VIII) we discuss the relation between environment and bars in disk galaxies and finally in Carollo et al. 2012b (Paper IX) we compare sizes and surface mass densities for both the entire galaxies and also the bulge and disk components in the four environments explored in ZENS.

The following cosmological parameters are adopted in all the ZENS publications:  $\Omega_m = 0.3$ ,  $\Omega_\Lambda = 0.7$  and  $h = 0.7$ . Unless otherwise specified, magnitudes are in the AB system, and galaxy sizes are *semi-major* axis measurements. All derived luminosities are corrected for Galactic extinction using the maps of Schlegel et al. 1998.

## 2. A BRIEF SUMMARY OF ZENS

### 2.1. Data and sample

ZENS is based on a sample of 1630 galaxies, members of 141 galaxy groups extracted from the 2-degrees Field Galaxy Redshift Survey (2dFGRS) (Colless et al. 2001, 2003), and specifically from the Percolation-Inferred Galaxy Group (2PIGG) catalogue (Eke et al. 2004a). The 141 ZENS groups are a random selection of the 2PIGG groups which are found in the very thin redshift slice  $0.05 < z < 0.0585$  and have at least 5 con-

firmed members, down to a magnitude  $b_J = 19.45$ . New  $B$ - and  $I$ -band images were acquired for these groups with the WFI camera mounted at the Cassegrain focus of the MPG/ESO 2.2m Telescope at La Silla, over several observing runs between 2005 and 2009. We describe here the structural analysis that we have performed on the WFI  $B$  and  $I$  images for a first set of 769 galaxies in the 79 first-epoch ZENS groups (see Paper I for details).

### 2.2. The four environments investigated in ZENS

For each ZENS galaxy, Paper I discusses and publishes four estimates of environment: the group halo mass, the distance from the center of the group, the rank within the group (i.e., whether the galaxy is the central or a satellite) and the location on the large scale structure (LSS). In particular:

(1) Group masses  $M_{GROUP}$  are derived from the total group luminosities by assuming a mass-to-light ratio calibrated with mock catalogs (Eke et al. 2004b).

(2) The ranking of galaxies in centrals and satellites factors in the errors on the galaxy stellar masses, and includes a test of self-consistency requiring that a bona-fide central galaxy must, simultaneously, be consistent with being the most massive galaxy of the group, be located within a projected distance  $< 0.5R_{200}$  from the mass weighted center of the group (with  $R_{200}$  the characteristic size of the group, as defined in Paper I), and have a relative velocity within one standard deviation from the group velocity.

(3) The centers of the groups, on which the projected radial positions of satellite galaxies within the groups rely, are identified with the locations of the central galaxies. We operationally divide the ZENS group sample into *relaxed* and *unrelaxed* groups, depending on whether a bona-fide central galaxy can be found, according to the prescription above. In Paper I we discuss the observational biases which may hamper the identification of the central galaxy in groups which are in fact dynamically relaxed. We therefore use our group classification scheme mostly to test that our results are not affected by the inclusion/exclusion of the unrelaxed groups from our studies, although we keep an eye on the possibility that there may be a physical origin, related to the dynamical evolution of the host groups, for differences observed in otherwise similar galaxies that inhabit the two classes of groups.

(4) The LSS density at the ZENS group locations is defined using an Nth nearest-neighbor analysis which adopts the groups (not the galaxies) as the tracers of the LSS density. Specifically, we define  $\delta_{LSS} = \frac{\rho_{LSS}(z) - \rho_m}{\rho_m}$ , with  $\rho_{LSS}(z)$  the density of 2dFGRS groups in a projected circular area defined by the comoving distance of the 5th nearest-neighboring group around the ZENS group, and  $\rho_m$  is the mean projected density calculated over the global 2dFGRS area at the given redshift. Our choice results in identical  $\delta_{LSS}$  values for all galaxy members of any given group, and avoids the problems that are associated with using Nth-nearest neighboring galaxy algorithms (see Paper I, and also Peng et al. 2012).

### 2.3. Galaxy stellar mass completeness limits for ZENS

In Paper III we discuss the mass completeness limits of ZENS which is determined by the 2dFGRS apparent

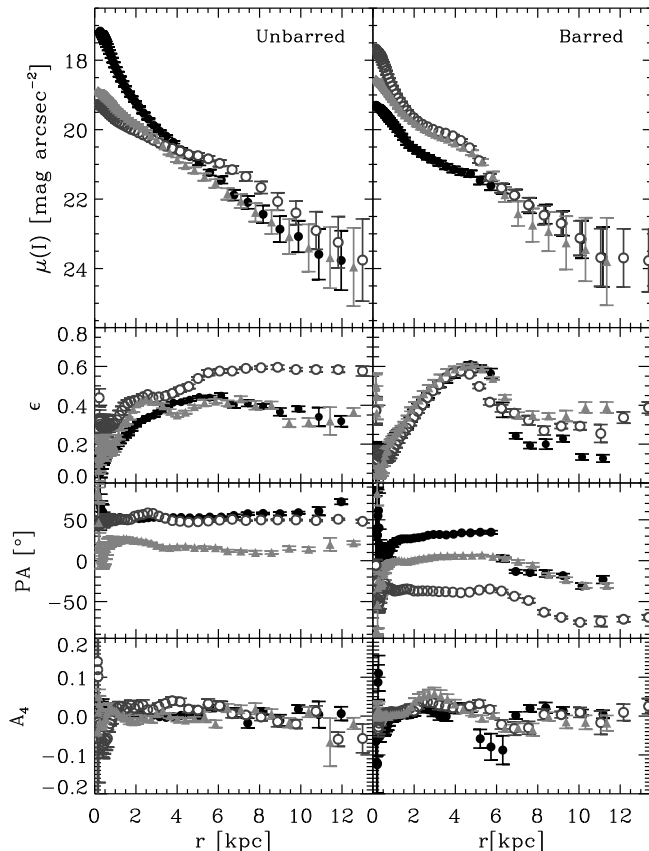


**Figure 1.** From top to bottom, the panels show the radial profiles of  $I$ -band surface brightness, ellipticity, position angle and the high order Fourier coefficient  $A_4$  for three example of ZENS disk galaxies classified as non-barred (left) and barred (right). Different symbols and gray shades are used to distinguish the profiles for the three individual galaxies.

magnitude selection. The strongest constraints are set by passively evolving galaxies, which have the larger mass-to-light ratio, for which the 85% completeness is reached above  $10^{10} M_{\odot}$ . This is the mass completeness threshold that we adopt for passive elliptical and S0 galaxies. Progressively more actively star forming galaxies have progressively lower mass completeness thresholds; given the good correlation between star formation rate and morphological type (see Paper III), the following mass completeness thresholds are adopted for the remaining morphological classes:  $10^{9.82} M_{\odot}$ ,  $10^{9.78} M_{\odot}$  and  $10^{9.48} M_{\odot}$  respectively for bulge-dominated spirals, intermediate bulge-to-total disk galaxies, and late-type disk (or irregular) galaxies.

### 3. QUANTIFICATION OF GALAXY STRUCTURE. I. AN ISOPHOTAL ANALYSIS

Surface brightness profiles and isophotal parameters were obtained with the IRAF ELLIPSE routine. This well-tested algorithm fits the intensity at a given radius with the Fourier series  $I(\theta) = I_0 + \sum (A_n \cos n\theta + B_n \sin n\theta)$  (Jedrzejewski 1987). Here  $I_0$  is the mean intensity within the isophote, and  $A_n$ ,  $B_n$  the high harmonic coefficients which quantify isophotal deviations from perfect ellipticity. We truncated the series after the fourth order, so that, for each isophote, the fits return the mean intensity, position angle (PA), ellipticity

( $\epsilon$ ), and the amplitude of the fourth-order coefficients  $A_4$  and  $B_4$ . The coefficient  $A_4$  has been extensively used in the past to measure ‘boxiness’ ( $A_4 < 0$ ) and ‘diskyness’ ( $A_4 > 0$ ) of the isophotes (e.g., Bender et al. 1988, Franx et al. 1989, Naab et al. 1999).

In running ELLIPSE, we allowed the position angle and ellipticity to vary freely with radius, and limited wanderings of the isophotal center to within 3 pixels from the center of the innermost isophotes. The PA and ellipticity determined by the SEXTRACTOR algorithm (Bertin & Arnouts 1996) served as initial guesses for the ELLIPSE algorithm. The semi-major axis of adjacent isophotes was increased in logarithmic radial steps of 0.1, in order to increase the signal-to-noise ratio when measuring the external isophotes. We allowed the code to perform a two iteration 3-sigma clipping of the discrepant pixels during the fits, and terminated the fitting procedure when  $> 50\%$  of the pixels in a given step of the calculation were flagged as discrepant.

The procedure was applied independently to the  $I$  and  $B$  images, and returned independent surface brightness profiles in each of the two passbands. We also derived surface brightness profiles in the  $B$  filter using the isophotal parameters derived from the  $I$  images; this returned more reliable surface brightness profiles also at the shorter wavelength for those galaxies whose  $B$  light distributions were too irregular (because of dust absorption and star formation knots) for a reliable measurement directly on the  $B$  images.

#### 3.1. Bar identification and quantification of bar strength

Changes in the radial profiles of PA and ellipticity are used as a first diagnostics to identify bars in the (disk) galaxies. The presence of a bar produces a characteristic signature on the isophotes shapes: within the bar region the ellipticity increases smoothly to a maximum value with almost constant PA, and then drops abruptly at the end of the bar, where also the PA changes substantially.

We inspected the  $I$ -band ellipticity and position angle radial profiles of the disk galaxies in our sample (S0 and later, see Section 7 for the definition of the morphological types). We classified a disk galaxy as barred if its ellipticity grows to an absolute maximum greater than 0.2, and shows a variation in ellipticity and PA greater than  $0.1$  and  $10^\circ$ , respectively. In the bar region, we furthermore request that the PA profile is flat within  $\pm 20^\circ$ . The size of the bar,  $a_{bar}$ , was defined to be the semi-major axis associated with the maximum value of the ellipticity profile, subject to the condition that it has to be at least twice the FWHM of the PSF, which is typically  $\sim 1''$ . Note that galaxies with bar sizes smaller than this threshold are not considered as barred systems. Therefore, our final sample of barred disks provides a conservative lower limit to the total number of such galaxies in the entire sample. Illustrative examples of the isophotal parameters profiles for a random selection of ZENS galaxies classified as barred and non-barred are shown in Figure 1.

The above mentioned criteria are widely used in the search for bars (e.g. Knapen et al. 2000, Menéndez-Delmestre et al. 2007 or Sheth et al. 2008) and are shown to provide robust results, but they can fail in identifying a bar if, e.g., the bar has a similar PA to that of the disk (see e.g., Menéndez-Delmestre et al. 2007). For this rea-



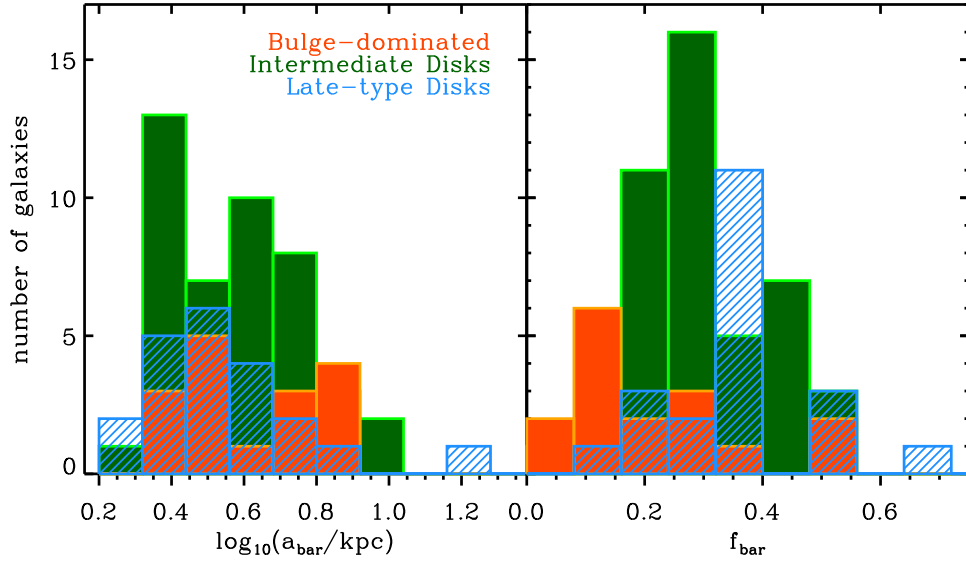


**Figure 2.** Distribution of bar semi-major axes (left) and strengths (right) for the ZENS galaxies which are classified as barred. Histograms are colored differently according to the disk galaxy type hosting the bar: orange=S0/bulge-dominated spirals; green=intermediate-type disks; blue=late-type disks.

son, we also visually inspected all the disk galaxies and those which clearly showed a bar structure – and had an ellipticity profile consistent with it, but no drop in PA – were included in the barred sample as well. Combining the ELLIPSE fitting method with the visual validation we concluded that  $\sim 10\%$  (i.e., 83 out of 717) of disk galaxies have a clear bar signature.

To quantify the bar strength we used the definition of Abraham & Merrifield 2000, i.e.,

$$f_{\text{bar}} = \frac{2}{\pi} \left[ \arctan \left( \frac{b}{a} \right)_{\text{bar}}^{-\frac{1}{2}} - \arctan \left( \frac{b}{a} \right)_{\text{bar}}^{+\frac{1}{2}} \right], \quad (1)$$

where  $(\frac{b}{a})_{\text{bar}}$  is the intrinsic axial ratio of the bar. The bar strength ranges from zero to unity for unbarred galaxies and infinitely strong bars, respectively. The intrinsic axial ratio was derived from the observed one using the transformation of Abraham et al. (1999), i.e.,

$$\left( \frac{b}{a} \right)_{\text{bar}}^2 = \frac{1}{2} (X - \sqrt{X^2 - 4}), \quad (2)$$

with

$$X = \sec^2 i [2 \cos^2 \phi \sin^2 \phi \sin^4 i + (b/a)_{\text{inner}}^2 (1 - \sin^2 \phi \sin^2 i)^2 + (b/a)_{\text{inner}}^{-2} (1 - \cos^2 \phi \sin^2 i)^2].$$

Here  $i$  is the inclination angle obtained from the minor and major axis of the galaxy considered as whole ( $i = \arccos(b/a)_{\text{out}}$ ),  $(b/a)_{\text{inner}}$  is the observed axis ratio of the bar and  $\phi$  is the twist angle between the bar and galaxy semi-major axis. For our sample we computed  $(b/a)_{\text{inner}}$  at the bar semi-major axis  $a_{\text{bar}}$  and we used the values of ellipticity and PA obtained from SEXTRAC-

TOR (Bertin & Arnouts 1996) to calculate  $(b/a)_{\text{out}}$  and  $\phi$ .

Figure 2 shows the distribution of bar strength and bar sizes measured in the first-epoch ZENS samples of bulge-dominated galaxies (including both S0 and bulge-dominated spirals), intermediate-type and late-type disk galaxies. Note that the median bar strength increases with Hubble type, changing from a value of  $\langle f_{\text{bar}} \rangle = 0.17^{+0.04}_{-0.02}$  for S0 or bulge-dominated spirals, to  $\langle f_{\text{bar}} \rangle = 0.29^{+0.02}_{-0.01}$  for intermediate-type disks and  $\langle f_{\text{bar}} \rangle = 0.36^{+0.03}_{-0.03}$  for late-type disk galaxies. Conversely, bars in early-type galaxies are more extended than those in late-type disks:  $\langle a_{\text{bar}} \rangle = 3.8^{+0.77}_{-0.27}$  kpc for S0 and bulge-dominated spirals,  $\langle a_{\text{bar}} \rangle = 3.7^{+0.24}_{-0.18}$  kpc for intermediate-type disks and  $\langle a_{\text{bar}} \rangle = 3.4^{+0.31}_{-0.18}$  for late-type disks. The correlation between bar properties and Hubble types has been investigated in a number of works in the literature whose results are consistent with our measurements. A weakening of bars in early type galaxies, for example, has been reported before by e.g. Laurikainen et al. (2007); Buta et al. (2005); Barazza et al. (2008); Aguerri et al. (2009). Using a local sample of known morphological type, Erwin (2005) showed that the bar size is larger in S0-Sab galaxies than in disk-dominated galaxies, consistently with the difference we observe in the ZENS galaxy sample.

Note that no split in galaxy stellar mass was applied to our sample of barred galaxies. It is well established however that galaxy mass is a fundamental factor affecting most galaxy properties, including the incidence of bars (e.g. Sheth et al. 2008; Cameron et al. 2010; Nair & Abraham 2010b). It is thus possible that some of the presented statistics on bar properties in the ZENS samples are induced by the different ranges of stellar mass

represented in the subsamples of disk galaxies of varying bulge-to-total ratios. We postpone to a forthcoming paper (Cibinel et al 2012b, in prep.) a detailed ZENS analysis of the bar fraction, at constant galaxy mass, in diverse environments.

#### 4. QUANTIFICATION OF GALAXY STRUCTURE. II. PARAMETRIC CHARACTERIZATION

Two dimensional fits to the surface-brightness distributions of all first-epoch ZENS galaxy images were carried out with the Galaxy Image 2d (GIM2D) software package (Marleau & Simard 1998, Simard et al. 2002). We used a single Sérsic profile to describe the total galaxy light distribution, i.e.:  $\Sigma_b = \Sigma_e \exp\{-k_n[(r/R_e)^{1/n} - 1]\}$  where  $\Sigma_e$  is the surface intensity at the half-light radius  $R_e$  and the parameter  $k_n$  is set to  $k_n = 1.9992n - 0.3271$ .

For the ZENS galaxies which are not classified as ellipticals (in Section 7), we also performed two-components, bulge+disk decompositions of the two-dimensional galaxy light distributions. For this purpose we assumed a Sérsic profile for the bulge and a perfectly exponential disk represented by  $\Sigma_d = \Sigma_0 \exp(-r/h)$ , with  $\Sigma_0$  the central surface intensity and  $h$  the disk scale length. Pure exponential models, with no bulge component, were furthermore generated for galaxies classified as late-type disks. Table 1 summarizes the range of values between which the model parameters were allowed to vary.

GIM2D convolves the theoretical models with the PSF before fitting them to the galaxy images. We modeled the PSF of each of the ZENS group with a two-dimensional gaussian having FWHM equal to the mean of the full-widths measured on several unsaturated stars over the ZENS fields. During the fitting procedure, the code was allowed to re-compute the initial parameters from the image moments and to fit the sky background level in each individual postage stamp galaxy image; the postage stamps were sized proportionally to the SExtractor Petrosian radius of the galaxies, and set to be equal to 3 times the Petrosian radius. On a set of simulations calibrated on the GEMS survey (Rix et al. 2004), fixing the background to a locally defined value during the GIM2D fit was shown to improve the performances for low surface brightness galaxies (Häussler et al. 2007). Our alternative approach was to enable the local sky subtraction and to quantify any systematic bias in the GIM2D fits using a large set of artificial galaxy images which are specifically tailored to the ZENS observations (Section 6). The sky pixels were identified as those pixels in the galaxy postage stamps that were located outside an aperture equal to 1.5 times the SExtractor Petrosian radii of the galaxies. Bright star-forming clumps were masked during the fitting procedure. Finally, although GIM2D offers an option to correct for the effects of the disk optical thickness – which consists in adding to the disk total magnitude a geometric factor  $2.5 \times \log(a/b)$  where  $a/b$  is the axis ratio – we decided not to use this feature, and disks were assumed to be optically thin in order to fit the actually observed light distribution without a prior assumption about the dust distribution.

##### 4.1. Details of the variable- $n$ single Sérsic fits and $n = 1$ pure exponential fits

To be able to detect color gradients, for the variable- $n$  single Sérsic fits as well as for the  $n = 1$  pure exponential models, the  $B$ - and  $I$ -band images were fitted independently without imposing the structural parameters of one filter to the other band. The position angles and ellipticity derived from the  $B$ - and  $I$ -band images agree well, with differences being limited to  $15^\circ$  and 0.15, respectively. In only 2% of the galaxies we find differences which are larger than this, with a maximum change in ellipticity  $\sim 0.2$  and a maximum change in position angle  $\sim 30^\circ$ . Generally speaking, we thus conclude that the single component fits are robust and strong twists between the  $B$ - and  $I$ -band isophotes are not a problematic issue when performing independent fits for the two passbands.

To verify the validity of the GIM2D single-component fits, we ran on all the GIM2D models the task **ELLIPSE**, keeping the isophotes fixed at the radii, position angle and ellipticity of the **ELLIPSE** fits to the real galaxy images described in Section 3. The comparison between the total magnitudes and the **ELLIPSE** profiles derived for the GIM2D models and those derived for the real galaxies, as well as the inspection of the residual images between the GIM2D models and the real galaxies, enabled us to reject unphysical GIM2D models.

Overall, we could obtain reliable Sérsic fits for 94% of the  $B$ -band images and 95% of those in the  $I$ -band. An even higher fraction of successful fits is obtained for the pure exponential models of late-type disks (99%). The distribution of stellar masses (from Paper III), sizes and morphological types for the 5% of ZENS galaxies with no single Sérsic fits is shown in Figure A5 and Table 3 of Appendix A. In this Appendix we also present, for the subset of ZENS galaxies for which the information is publicly available from the NYU-VAGC (Blanton et al. 2005), a comparison of our estimates of the Sérsic parameters with those published in this other catalogue; the comparison shows a good agreement between our *uncorrected* measurements and the previously published data. We show below that, in some regimes of parameter space, these measurements require nonetheless further corrections to be cleaned by observational biases.

##### 4.1.1. Comparison between $B$ - and $I$ -band models

The comparison between the structural parameters obtained from the single Sérsic fits with variable- $n$  in the two available passbands is shown in the left and central plots of Figure 3. The single component fits in the two different pass-bands generally provide consistent measurements with little scatter. In particular, half-light radii measured in the two pass-bands are in very good agreement with each other. The  $I$ -band fits, however, result in slightly steeper profiles: at this wavelength galaxies have  $n$  indices which are bigger by  $\sim 15\%$  with respect to those measured in the  $B$ -band.

Another difference is observed between  $I$ - and  $B$ -band disk scalelengths of large late-type galaxies, as derived from the pure exponential fits (right-hand side plot in Figure 3): disk scalelengths  $h$  derived from  $n = 1$  fits to relatively large late-type disk galaxies are smaller at the longer wavelength by  $\sim 10$ –20%. We have checked that the  $I$  magnitude distribution of these late-type disks is not biased towards faint values that would raise concerns on surface brightness detections. As we show in

**Table 1**  
Range of allowed values for the parameters of the GIM2D fits.

Parameter	Double Component Fits			Single Sérsic Fits			Pure Exponential Fits		
	initial guess	min	max	initial guess	min	max	initial guess	min	max
$m_{T,B} / m_{T,I}$ (mag)	18/16.5	21.5/20	13/12	18/16.5	21.5/20	13/12	18/16.5	21.5/20	13/12
$B/T$	0.5	0	1	1	1	1	0	0	0
$R_{e,bulge}$ (kpc)	2.3	0.5	20	2.3	0.5	30	-	-	-
$\epsilon_{bulge}$	0.5	0	0.7	0.5	0	1.0	-	-	-
$\phi_{bulge}$ ( $^{\circ}$ )	45	-180	180	45	-180	180	-	-	-
$h$ (kpc)	2.3	0.5	20	-	-	-	2.3	0.5	20
$i_{disk}$ ( $^{\circ}$ )	45	0	90	-	-	-	45	0	90
$\phi_{disk}$ ( $^{\circ}$ )	45	-180	180	-	-	-	45	-180	180
$\Delta x$ (pixels)	0	-2	2	0	-2	2	0	-2	2
$\Delta y$ (pixels)	0	-2	2	0	-2	2	0	-2	2
$n$	2.1	0.2	10	2.1	0.2	10	-	-	-

**Note.** — Permitted ranges for the variation of model parameters used in the GIM2D fits. From top to bottom: total galaxy magnitude in  $B$  and  $I$  bands, bulge-to-total ratio ( $B/T$ ), bulge half-light radius, bulge ellipticity, bulge position angle, disk scale length, disk inclination angle, disk position angle,  $x$  and  $y$  galaxy center offset from the SEXTRACTOR center (further refined by using the IRAF `imcntr` task), and Sérsic index. The precise values for the range of the bulge and disk radii change slightly according to the galaxy redshift; the listed values refer to the median redshift for the ZENS sample of galaxies.

detail in Section 6.3, the  $I$ -band GIM2D sizes that we derive for relatively large,  $n \sim 1$  galaxies are not severely affected by observational biases. We thus interpret this result as mostly due to a genuine color gradient in large late-type disks. Note that the average difference in the  $I$  and  $B$  disk scalelengths in the pure exponential fits of late-type disk galaxies is consistent with a similar difference reported for a sample of local late-type galaxies by de Jong (1996) and Barden et al. (2005).

Together, the larger  $h$  values from  $n = 1$  fits and smaller Sérsic indices from variable- $n$  fits of late-type disks in the  $B$ -band relative to the  $I$ -band are consistent with being the joint result of the segregation of young stars in the galaxy outskirts and, also, of light absorption from the center of the galaxies by interstellar dust, as discussed in a number of observational and theoretical works (e.g. Byun et al. 1994; Beckman et al. 1996; Cunow 2001; Möllenhoff et al. 2006).

The more pronounced variation of disk scalelength in the pure exponential fits with respect to the half-light radius in the Sérsic fits for the late-type galaxies can be readily understood: whereas in the variable- $n$  single Sérsic fits a lower central concentration of light can be modeled with a smaller value of the Sérsic index  $n$  and a relatively small change in the effective radius, fixing the index to  $n = 1$  in the pure exponential fits forces an increase of the characteristic scalelength in order to obtain a milder radial decline in surface brightness in the  $B$  band. This is consistent with the fact that the largest variation in  $n$  values between the  $B$ - and  $I$ -band variable- $n$  Sérsic fits to late-type disks are observed for those galaxies which also have the largest variations in scalelength  $h$  when fitted with an  $n = 1$  profile.

Finally we note that a self-consistent correction for dust effects would require radiative transfer simulations of the light scattered and re-emitted by the dust grains (e.g. Byun et al. 1994; Cunow 2001; Tuffs et al. 2004); this is beyond the scope of this paper. Moreover it remains difficult to disentangle dust effects from genuine radial segregation in the stellar populations. For these reasons, instead of attempting a correction for dust ab-

sorption, we choose the empirical approach of employing the less dust-sensitive  $I$ -band data as the fiducial reference for our structural measurements, and to discuss separately possible dust-reddening effects, when relevant, e.g., in studying color profiles, star formation rates (see Paper III).

#### 4.2. Details of the bulge+disk decompositions

Double component, bulge+disk decompositions were also performed on both the  $B$ - and  $I$ -band images of all galaxies which are not classified as ellipticals or irregulars (Section 7). For the  $I$ -band, our reference filter for structural measurements, no a priori constraints on the bulge and disk parameters were imposed during the fitting procedure, except for the wide limits listed in Table 1. In the  $B$  filter, each galaxy was instead fitted in four different ways: a) by performing a separate decomposition to the  $B$ -band letting the structural parameters completely unconstrained (unconstrained model fit, hereafter  $UF$ ), b) by fixing the disk and bulge position angles, ellipticity and inclination to those of the  $I$ -band (constrained model fit number one, hereafter  $C1$ ), c) by also fixing the bulge half-light radius and Sérsic index  $n$  (constrained model  $C2$ ) and d) by keeping all the parameters tied to those of  $I$ -band except for the  $B/T$  and total flux (constrained model  $C3$ ). In all the models we allowed a maximum wandering of 2 pixels for the disk and bulge components from the SEXTRACTOR center.

There are clear advantages and disadvantages in performing either independent or constrained fits to the two bands: by fixing the  $B$ -band structural parameters to the  $I$ -band, one ensures that bulge and disk colors are measured consistently over the same regions; this however prevents the detection of structural differences and color gradients. For this reason we decided to adopt a mixed approach to determine the bulge and disk parameters to the  $B$ -band.

First, not all models returned by the GIM2D fits are physically-meaningful bulge+disk decompositions. We hence adopted a filtering scheme to reject unreliable or unphysical models to all GIM2D models, i.e., the fiducial

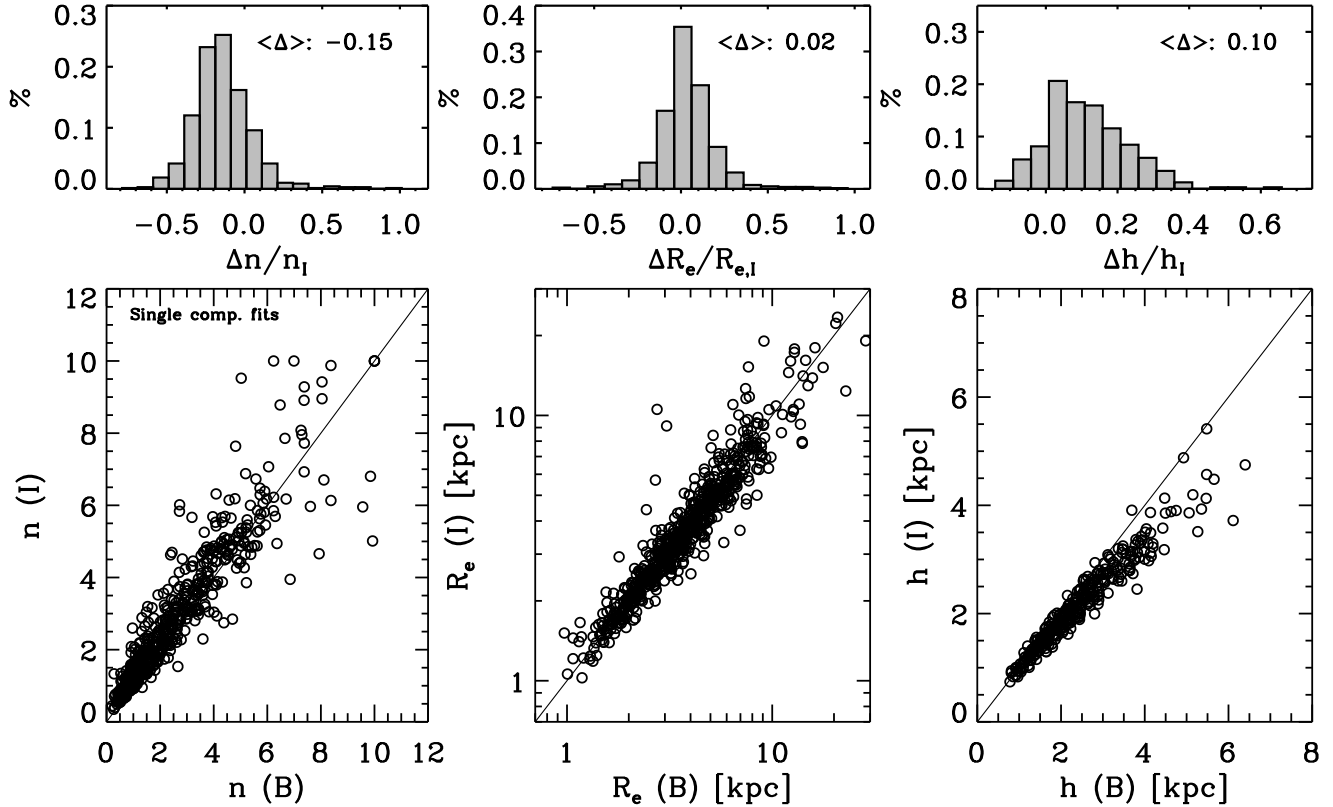


**Figure 3.** Comparison between half-light radii (left) and Sérsic indices (center) obtained from the GIM2D single Sérsic fits to the  $I$ - and  $B$ -band data. The upper histograms show the distributions of the parameter differences in the two filters ( $B$ -band minus  $I$ -band), normalized to the  $I$ -band measurements. The median value of the structural variation between the  $I$ - and  $B$ -band is given inside these upper panels. Values are presented for the *uncorrected* GIM2D measurements, i.e., before applying our correction scheme for systematic biases described in Section 6.3. The rightmost panels show the comparison between the disk scalelengths obtained from the pure exponential fits in the two pass-bands to galaxies classified as late-type disks. In the  $I$ -band, variable- $n$  Sérsic fits result in  $\sim 15\%$  larger  $n$  values than those measured for the same galaxies in the  $B$ -band. Furthermore, the  $I$ -band scalelengths of  $n = 1$  pure exponential fits to relatively large late-type disks are  $\sim 10 - 20\%$  smaller than those derived from similar fits to the  $B$ -band images.

$I$ -band models for each galaxy, and the four versions of the  $B$ -band models. Our filtering scheme is discussed in Appendix A.

We then followed a quantitative procedure to select, amongst the physically-valid alternatives for the  $B$  bulge+disk fits for each galaxy, our fiducial (i.e., in our judgement, the most reliable) bulge+disk  $B$ -band decomposition. In brief, we required that all  $B$ -band disk and bulge fits always have bulge and disk position angles, disk inclinations and bulge axis ratios consistent, within a sensible range<sup>8</sup>, to those of the  $I$ -band fits. When this was achieved with unconstrained fits to the  $B$  band images, these unconstrained fits were retained as a fair description of the  $B$  bulge+disk decompositions. This choice maximizes the detection of possible wavelength-dependent structural differences and color gradients. For galaxies in which such a consistency requirement was not achieved with the unconstrained  $B$  fits, we adopted as for the  $B$ -band fits those which satisfied such requirement with the minimum number of  $B$  parameters tied to the  $I$ -band fit parameters (i.e., in order of priority, the  $C1$ ,  $C2$  and  $C3$  fits).

<sup>8</sup> The allowed ranges of variations for  $B$  and  $I$  bulge and disk position angles, disk inclination angles and bulge ellipticities were respectively  $15^\circ$ ,  $15^\circ$  and  $0.15$ .

In cases where both the  $C1$  and  $UF$  models were in principle both potentially good representations of the bulge+disk properties of considered galaxy, we applied the following decision scheme: if the two models gave disk and bulge size,  $B/T$  and Sérsic indices within  $2.5\sigma$  of the dispersion measured around the identity from all the model falling in this latter category, then both models were validated as reliable, and we adopted as our fiducial bulge+disk parameter estimates the mean of the structural parameters returned by these two fits. If these two fits returned discrepant values, both were inspected and a judgement was made on which model to use, on the basis of the residual images and the difference in total magnitude between the galaxy and the model. Only 5% of the bulge+disk  $B$  fits needed this further visual validation. This entire procedure is schematized in Figure 4.

It is important to notice that, while disk scalelength and bulge-to-total ratios are quite consistently returned by all four fits to the  $B$  images, bulge sizes and Sérsic indices show much larger variations from one fit to the other. This is illustrated in Figure 5, where we compare the different measurements obtained for the  $B$ -band in the four cases  $UF$ ,  $C1$ ,  $C2$ ,  $C3$ . The dispersion around the identity line in the four fits is  $\sim 0.4$  kpc and 9% for  $h$  and  $B/T$ , and the dispersion for the bulge half-

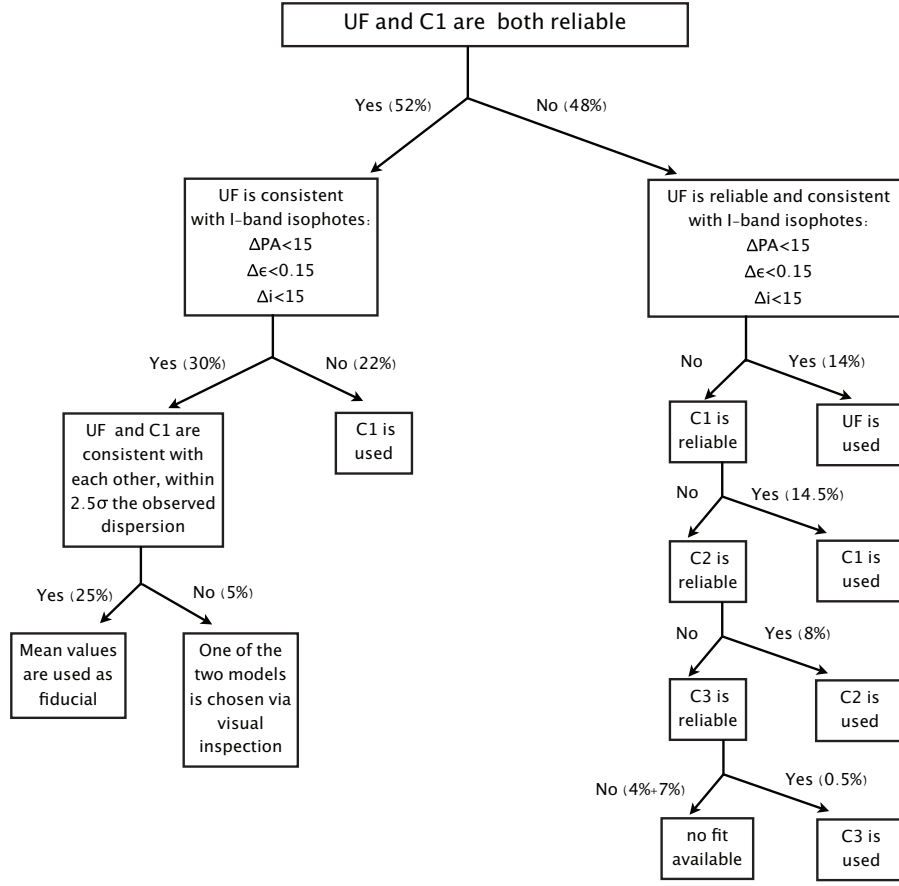


**Figure 4.** Flow chart describing our scheme for selecting the fiducial GIM2D bulge+disk  $B$ -band models.  $UF$ ,  $C1$ ,  $C2$  and  $C3$  are the four fits that we performed on the  $B$  images, respectively by keeping the  $B$  bulge and disk parameters completely unconstrained, fixing their position angles and ellipticities to those derived from the  $I$ -band fits, adding to the  $I$ -band-fixed parameters the bulge half-light radius and Sérsic index  $n$ , and finally, by tying to the  $I$ -band values also the  $B$  disk scalelengths. Number in parenthesis give the fraction of  $B$ -band bulge+disk decompositions which fall in each category; note that sub-branches sum up to the fractions listed on the previous level. The fractions refer to disk galaxies with a detected bulge component in the ZENS sample, i.e., to S0, bulge-dominated spirals and intermediate-type disks. The two numbers for the models with no bulge+disk decomposition in the  $B$ -band give the fraction of galaxies for which either an  $I$ -band fit is available, but no good  $B$ -band fit can be achieved (4%), or the fraction of galaxies for which neither an  $I$  nor a  $B$  bulge+disk decomposition can be achieved (7%).

light radii and Sérsic indices  $n$  is  $\sim 0.5$ - $0.7$  kpc and  $1.5$ - $1.7$ , respectively. Especially for the bulge  $n$  values, models with the isophote's position constrained and unconstrained can indeed provide very different results. Similar conclusions on the reliability of the bulge and disk parameters are drawn from tests on simulated galaxies which we discuss in Section 6.6.

Not surprisingly, the success rate for the bulge+disk decomposition is lower than the one for the single component. The single component fits return robust measurements for  $\sim 90\%$  of S0, bulge-dominated spirals and intermediate-type disk galaxies in the both the  $B$ - and  $I$ -bands (see Appendix A for a detailed summary for the individual morphological classes). Bulge+disk decompositions in both  $B$ - and  $I$ -bands are available for  $\sim 85\%$  of these galaxies.

For galaxies with a reliable decompositions in both bands, Figure 6 presents the parameters obtained in the two pass-bands. Partly by construction, the scatter around the identity line for the bulge-to-total ratio is less than  $0.1$  in the vast majority of the cases, as shown on the top left panel of the Figure. Given that our morphological classification is based on the  $I$ -band

bulge-to-total ratios, this means that our classification would not change substantially if we had used the  $B$ -band measurements instead. The disk sizes obtained in the two filters agree well with each other, although disks are more extended in the  $B$ -band than in the  $I$ -band, as also discussed above. As anticipated, the bulge radii and indices have instead a broader scatter. Note that, despite the scatter, in the vast majority of cases the Sérsic indices for the bulge are consistent with either a 'concentrated' or a 'diffuse' central bulge component in both filters; truly discrepant results are obtained in a small number of cases ( $\sim 7\%$ ).

#### 4.2.1. Comparison between galaxy half-light radii estimated from single Sérsic fits and from bulge+disk fits

As we will discuss extensively in Section 6.3 the calculation of a galaxy size radius is made difficult by a number of observational biases which can lead to substantial uncertainties. Here we additionally show how the estimation of the galaxy half light radius depends on the choice of the fit used to model the galaxy light, by comparing the global galaxies half-light radii derived from the single Sérsic fits with those obtained from the

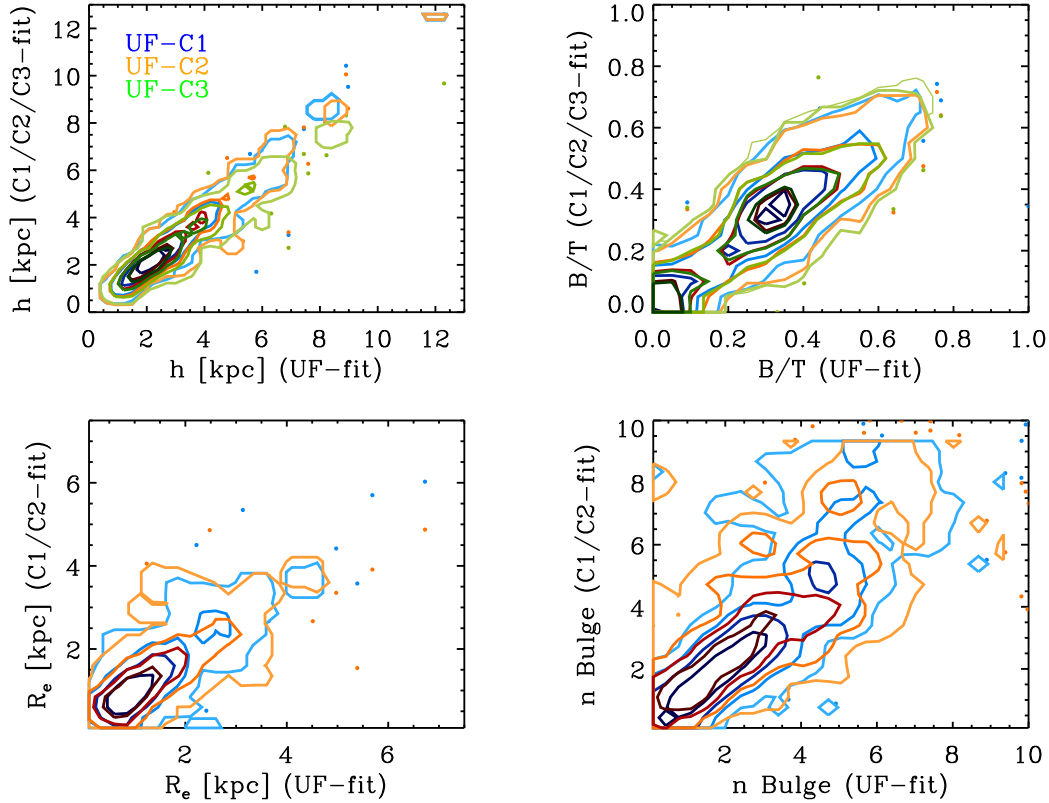


**Figure 5.** Comparison between the bulge and disk structural parameters obtained with GIM2D in the four different  $B$  fits described in section 4.2. These four  $B$  fits vary between being totally unconstrained ( $UF$ ), and fully tied too the  $I$ -band best fit parameters ( $C3$ ). From top to bottom and left to right we show the disk scale-length, bulge-to-total ratio, bulge effective radius and bulge Sérsic index. The contours identify isodensity regions containing 25%, 50%, 75% and 95% of the data. The points show the models which are not encompassed by the contours. The three different colors highlight the comparison between the unconstrained  $B$  fits ( $UF$ ) with the  $B$  models in which the position angles, ellipticity and inclination angle are tied to the  $I$ -band ( $C1$ , blue contours), with those in which also the bulge half-light radius and Sérsic index are kept fixed ( $C2$ , orange contours) and with the models which are fully tied to the  $I$ -band structural parameters ( $C3$ , green contours). The green curves are shown only for disk scalelengths and bulge-to-total ratios, as model  $C2$  and  $C3$  have the same bulge parameters.

bulge+disk decomposition. This is shown in Figure 7 for the  $I$ -band, but similar results are obtained in the  $B$ -band. It is clearly seen that for about 10% of the galaxies with formally ‘reliable’ bulge+disk decomposition and single component fits, half-light radii from the Sérsic models are larger by more than a factor 1.5 than the sizes inferred from the bulge+disk decompositions. As illustrated in the inset in Figure 7, the majority of the discrepant galaxies have steep light profiles with Sérsic index  $n > 2$ . We note that for all these galaxies both the single and double component fits were inspected to confirm their reliability; furthermore, the magnitude difference between the model galaxy and the real ZENS image within an aperture equal to 1.5 times the Petrosian radius is  $< 0.3$  mag for both the single and double component fits (see surface brightness profiles for the models and real galaxies and residual images in Figure A4).

For these galaxies we decided to keep both radii estimates but we provide an additional uncertainty on the size estimate with respect to the formal error, which is given by half the difference between the two radii estimates.

### 5. QUANTIFICATION OF GALAXY STRUCTURE. III. NON-PARAMETRIC ANALYSIS

To quantify the morphology of our sample of galaxies with non-parametric indicators we used the *Zurich Estimator of Structural Types Plus* (ZEST+), which upgrades the ZEST approach published in Scarlata et al. 2007.

ZEST+ is a C++-based code for the study of galaxy structure and it is designed for automated morphological classification of galaxies through either a principal component analysis or a support vector machines technique. The classification scheme uses both user supplied parameters and/or a set of non-parametric morphological coefficients computed by ZEST+ itself. For the ZENS galaxies we employed ZEST+ only to derive the structural coefficients, rather than using the morphological classification option, since, given the limited size of our sample and the availability of bulge-to-disk ratios, we chose to base our morphological classes mainly on the latter (see Section 7). ZEST+ has been thoroughly tested on large galaxy samples and, thanks to several improvements relative to the ZEST algorithm and implementation of Scarlata et al. 2007, shown to be even more robust – see for example Cameron et al. 2010 for a first application to the COSMOS (Scoville et al. 2007) field.

The output coefficients of ZEST+ that we used in

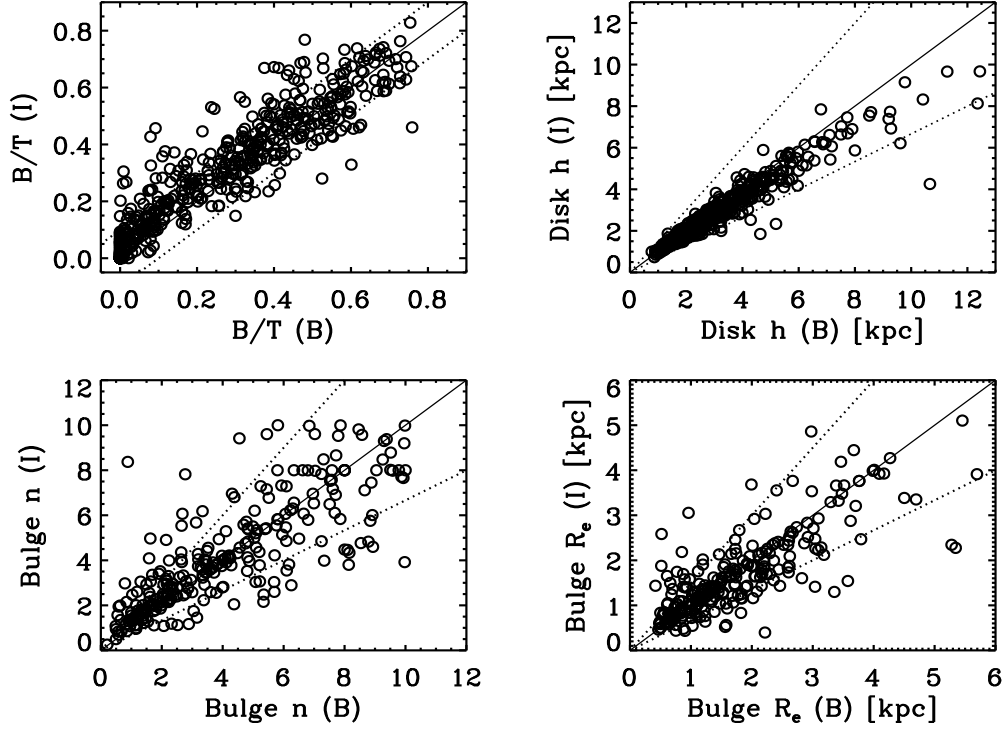


**Figure 6.** Comparison between the GIM2D double-component  $I$ -band fit parameters, and the corresponding parameters in the finally-adopted, fiducial  $B$ -band fits. Specifically, the upper panels show the comparison between the bulge-to-total ratios and disk scale lengths in the two filters. The lower panels show the comparison between the bulge half-light radii and bulge Sérsic indices. In the upper left panel, values are plotted only for galaxies which have detected bulge and disk component in both bands. In the other panels, galaxies are further constrained to have  $B/T > 0.1$  when considering bulge parameters. The dashed lines in the upper left panel indicate a positive and negative variation of 0.1 in the bulge-to-total ratio with respect to the identity line; in the other three panels, they indicate a relative change of a factor of 1.5.

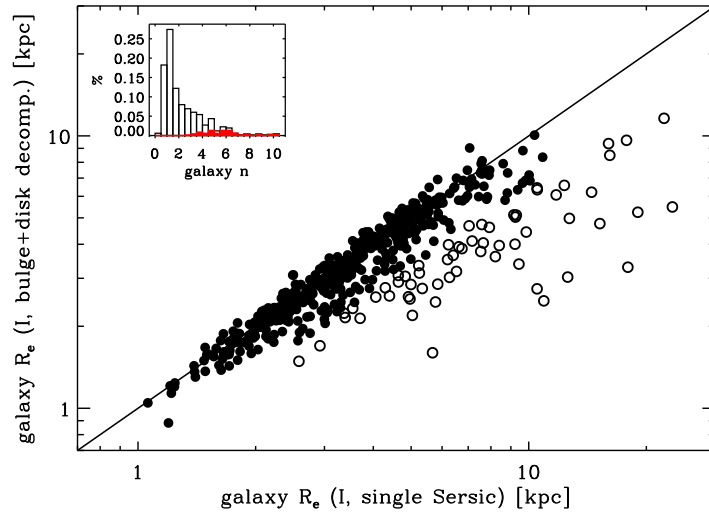


**Figure 7.** Comparison between  $I$ -band galaxy half-light radii obtained from single Sérsic fits and bulge+disk decompositions. The empty circles highlight those galaxies for which the two size estimates differ by more than a factor 1.5. The distribution of galaxy Sérsic indices for such discrepant cases are shown in red in the inset on the top left corner of the plot, in comparison with the indices for the rest of the sample, shown in black.



ZENS are galaxy concentration ( $C$ ), asymmetry ( $A$ ), Gini and  $M_{20}$  coefficients, and smoothness ( $S$ ). These morphological estimators are widely used in the literature to study galaxy structure and morphology (e.g. Conselice 2003, Lotz et al. 2004, Scarlata et al. 2007, Zamojski et al. 2007). For sake of brevity in the following we will refer to the  $C$ ,  $A$ , Gini,  $M_{20}$  and  $S$  set of measurements as to the “*CASGM*” parameters.

The concentration  $C = 5 \log(r_{80}/r_{20})$  was defined as the ratio of elliptical radii containing 80% and 20% of the total flux of the galaxy, which is provided as input by the user. For ZENS, the SExtractor Kron flux (FLUX\_AUTO) was employed.

The asymmetry index  $A$  gives information on the degree of rotational symmetry of the galaxy light. This is parametrized through the difference between the original galaxy image and a 180°-rotated version of it. To account for the effect of background noise, ZEST+ uses the procedure introduced by Zamojski et al. (2007), which involves the calculation of the asymmetry for both the original image  $A_0 = \frac{1}{2} \frac{\sum_{i,j} |I(i,j) - I_{180}(i,j)|}{\sum_{i,j} |I(i,j)|}$  and for a smoothed version of it,  $A_{0,S} = \frac{1}{2} \frac{\sum_{i,j} |I^S(i,j) - I_{180}^S(i,j)|}{\sum_{i,j} |I^S(i,j)|}$ , where  $I$  is the intensity of the image on the pixel  $(i, j)$  and  $I_{180}$  the intensity of the rotated image. The final asymmetry value is given by  $A = A_0 - \frac{A_0 - A_{0,S}}{1 - 1/\sqrt{5}}$ , where the last term corresponds to the background correction factor.

The Gini coefficient  $G$  introduced by Abraham et al. (2003) contains information on how uniformly the light is distributed within the galaxy: if the flux is equally distributed among all pixels, then  $G$  is equal to zero, whereas if all the light is concentrated in just one pixel, the coefficient  $G$  is equal to unity. We defined it as in Lotz et al. 2004:  $G = \frac{1}{\bar{I}n(n-1)} \sum_i^n (2i - n - 1) \bar{I}_i$ , where  $\bar{I}$  is the mean of the flux of the galaxy pixels, sorted in increasing order.

The parameter  $M_{20}$  is the normalized second-order moment of the brightest 20% of the galaxy pixels. It describes the spatial distribution of bright substructures within the galaxy, such as spiral arms, bars or bright nuclei. The computation of  $M_{20}$  involves the following steps: (i) galaxy pixels are ordered by flux, (ii) for the 20% brightest pixels, the sum of moments  $\Psi = \sum_i^{n_{20}} I_i [(x_i - x_c)^2 + (y_i - y_c)^2]$  with respect to the light-center in the Petrosian ellipse  $x_c$ ,  $y_c$  is computed, and (iii) the latter is normalized by the total sum of moments to give  $M_{20} = \log_{10} \left( \frac{\Psi}{M_{tot}} \right)$ , with  $M_{tot} = \sum_i^{n_{tot}} M_i$ .

Finally, the smoothness  $S$  is a measure of the degree of clumpiness of the galaxy light distribution, and is thus useful to trace patches in the light profile such as star-forming regions. To calculate  $S$ , a smoothed version of the original image, obtained by convolving it with a gaussian filter of FWHM equal to 0.25 times the petrosian radius  $R_p$ , was subtracted from the image itself. Clumpy regions were then identified from the residual image as those pixels for which the intensity  $I_{res}$  is  $k$  times higher than the background standard deviation in the residual image  $\sigma_{bkg}$ . We used a default threshold factor of  $k = 2.5$ . The pixels so identified were then used to calculate  $S = \left( \frac{\sum_{i,j} I_{res}(i,j)}{\sum_{i,j} |I(i,j)|} \right)_{I_{res}(i,j) > 2.5 \sigma_{bkg}}$ . A

region of radius  $0.25 * R_p$  from the center was masked out during the calculation to avoid including the highly concentrated centers of the galaxies which will boost the final value of the smoothness. The Gini,  $M_{20}$ ,  $A$  and  $S$  indices were all calculated within one petrosian ellipse.

Along with the structural indices, ZEST+ also gives an estimate for the “elliptical aperture” galaxy half-light radius, based on the user-provided total flux. When discussing ZEST+ based half-light radii for our ZENS galaxy sample, we will refer to these measurements.

## 6. CORRECTIONS FOR SYSTEMATIC BIASES IN THE STRUCTURAL PARAMETERS

The careful inspection and filtering of the measurements thus far presented, although necessary, does not provide a quantification of systematic or random errors in the derived structural parameters. In ZENS, and more generally in ground-based imaging galaxy survey (beyond our very nearest surroundings), the major contributors to such errors can be identified in the noise of the night sky and in a PSF width which is comparable to the typical size of the galaxies. Both analytical surface brightness fits and non parametric algorithms are affected by these observational limitation and none is completely free from pitfalls: the ZEST+ measurements are not PSF deconvolved and, to obtain a consistent measure of structure on the different ZENS fields, an homogenization to a common resolution of the *CASGM* parameters is necessary. In contrast, GIM2D uses the provided PSF to derive, in principle, seeing-corrected quantities, and indeed biases related to PSF-blurring are less severe in GIM2D-based measurements; however, a degree of uncertainty remains, which depends on the accuracy of the PSF modeling and the extend to which the galaxy is resolved. Furthermore, in low surface brightness regimes, both aperture photometry and two-dimensional fits are well known to underestimate galaxy sizes and fluxes (e.g. Bernstein et al. 2002a,b; Benítez et al. 2004; Häussler et al. 2007; Cameron & Driver 2007).

We asses here the impact of these effects specifically for our ZENS measurements through tests on artificial galaxy images. Our aim is to use the results of the tests to derive recipes to correct the observed galaxy structural parameters (e.g., sizes, concentrations, ellipticities, etc.) for the biases in the observations or, when this is not possible, to provide an estimate of the typical uncertainty affecting the data. We perform the analysis on the  $I$ -band, which we use as reference for the morphological classification, and which provides a view of the intrinsic galaxy structure less affected by dust or young stars. The corrections in the  $B$ -band are then derived from those obtained for the  $I$  measurements, suitably rescaled to the  $B$ -band luminosity and PSF.

### 6.1. Methodology

The derivation of the corrections is done by applying the entire process of object extraction, followed by parametric and non-parametric photometric/structural measurements with SExtractor/ZEST+ and GIM2D, in exactly the same way as on the real data, to a set of artificial galaxy images for which the intrinsic structural/photometric properties are known precisely by construction. The difference between the model input and



output parameters provides an estimate of the uncertainties in the measurements.

A self-consistent study of the errors in the quantification of the galaxy structural properties must be a function of five parameters: the galaxy luminosity (magnitude,  $mag$ ), the galaxy size (half-light radius  $R_e$ ), the inclination (ellipticity  $\epsilon$ ), the steepness of the light profile (Sérsic index  $n$  or concentration  $C$ ) and the PSF under which the galaxy was observed. The effects of each of such parameters on the quantification of structure, including galaxy sizes, are tightly interconnected and hence need to be considered simultaneously. It is immediately clear that, as an example, the impact of the PSF is stronger – with all other parameters fixed – for highly concentrated galaxies than for those with shallow light profiles, and for galaxies with sizes comparable to the seeing than for more extended ones.

We thus adopt a sampling approach in which we construct many thousand artificial galaxy models to fully explore the observed parameter space of galaxies in the ZENS data set, and such to have, for each combination of the five parameters  $mag - R_e - \epsilon - n(\text{or } C) - PSF$ , a sufficient number of models on which to test the measurements. This approach is also used in Carollo et al. 2012b (in prep.) on a higher redshift sample of galaxies extracted from the COSMOS survey.

Two cautionary remarks need to be made: first, our artificial galaxies are generated to populate *uniformly* a broad grid in the five-dimensional  $mag - R_e - \epsilon - n(\text{or } C) - PSF$  space. Real galaxies are not uniformly distributed in this parameter space, and this is not taken into account in our corrections. Second, we deliberately ignore dust or stellar population segregation effects, as our models are created smooth and neglect dust attenuation. In the following we will test the robustness of our corrections towards the specific design of the simulations.

### 6.2. Generation of the artificial galaxy images

To derive our correction function for the structural parameters of ZENS galaxies we created both Sérsic models and bulge+disk artificial galaxies on which we tested the corresponding GIM2D fits. In both cases, models were constructed on a grid of points in the ellipticity, magnitude, size and Sérsic index (or  $B/T$  ratio) parameter space. Specifically, in the single component case galaxies were simulated around the following regions:  $R_e = [0.4, 0.7, 0.9, 1.3, 1.5, 2, 3, 8, 20]$  kpc,  $I_{AB} = [13, 14, 15, 16, 17, 18, 19, 20]$ ,  $\epsilon = [0.1, 0.3, 0.6, 0.9]$  and  $n = [0.5, 1, 1.5, 2.5, 3.5, 4.5, 7.5]$ . For each grid node 30 models were generated randomly to have: radii and Sérsic indices within  $\pm 30\%$  of the nominal radius and index  $n$  at the grid point, magnitude within  $\pm 0.25$  magnitudes and a difference in ellipticity equal to  $\pm 0.05$ . This makes a total of  $\sim 60'000$  single-component model galaxies.

For the double component model galaxies, which span a wider range of combination of bulge and disk parameters and are also computationally more expensive, we used a coarser sampling of the parameter space, creating models in the following way: given a value of the magnitude for the *entire* galaxy randomly generated around the points  $I_{AB} = [13.7, 15.4, 16.8, 18.2, 19.6]$  and a disk scale length  $h$  similarly chosen within  $\pm 30\%$  from the positions  $[0.5, 1, 1.5, 3, 6, 15]$  kpc, artificial galaxies were

constructed in three bins of bulge-to-total ratios centered at values of  $B/T = 0.15, 0.4, 0.65$  and of width  $\Delta(B/T) = 0.15$ , hence allowing a maximum  $B/T = 0.8$ . The bulge half-light radius was selected on the same grid used for the disk scale length, but imposing that  $R_e < 1.678 \times h$ . The bulge Sérsic index was allowed to have values  $n = 0.5, 1, 2.5, 4, 8$  with a scatter of  $\pm 30\%$  and three bins of disk ellipticity (i.e galaxy inclination)  $\epsilon_{disk} = 0.1, 0.4, 0.7 \pm 0.1$  were employed. We furthermore assumed that bulges cannot be very elongated and hence explored only two values of the ellipticity for the bulge component, namely  $\epsilon = 0.1$  and  $\epsilon = 0.6$ .

All model galaxies described above were then convolved with three PSF sizes, for a total of  $180'000$  single component models and  $\sim 90'000$  double-component models. The three PSF sizes were taken to reproduce the best, medium and worst ZENS seeing in the  $I$ -band (respectively  $0.7''$ ,  $1''$ , and  $1.5''$ ). The PSF-convolved models were inserted with Poisson sampling into sky-subtracted empty regions extracted from the real ZENS fields. To mimic the effects of uncertainties in the reconstruction of the PSF in the real data, when performing the GIM2D fits on the simulated galaxies we provided as input to the code a *rotated* version of the PSF originally used to convolve the artificial image.

For brevity, we focus in the following on the results obtained for the simulations convolved with the median ZENS PSF, which are hence representative of the bulk of the ZENS observations. In Appendix B a full account of the results derived with the best and worst PSF can be found, which shows correction matrices that are consistent with those here presented. Note that the corrections to each ZENS galaxy were obtained through linear interpolation, at the PSF size value relevant for any given galaxy, of the correction matrices describing PSF sizes that bracketed the PSF in question.

### 6.3. Corrections of galaxy sizes and magnitudes

We start the description of the resulting correction functions by focusing on those parameters which our approach can self-consistently correct without recurring to additional information, namely galaxy sizes and magnitudes. We show in Section 6.4 how for other structural properties, such as the concentration coefficient, the recovery of the “true” values is instead less straightforward, and depends on the intrinsic distribution of parameters in the simulated sample (and requires therefore a different approach).

Our fiducial measurements of galaxy sizes in ZENS are those that we derive from the GIM2D analytic fits, which are less prone to systematic biases than those inferred with ZEST+, as we show below. It is nonetheless worthy to discuss here also the results for the ZEST+ measurements, not least because these measurements are used for the few ZENS galaxies for which no reliable GIM2D fit could be achieved.

After the extraction/fitting process on the artificial galaxies was completed, we produced “calibration maps” for sizes and magnitudes as shown in Figures 8 and 9. The arrows in the maps show, at any point of the *observed*  $R_e - mag - \epsilon - n(\text{or } C)$  plane, the direction and strength of the correction which is needed to recover the “intrinsic” galaxy size and magnitudes from the observed values; these correction arrows are obtained by

taking the median difference between the model nominal input parameters and the parameters measured with ZEST+/GIM2D of all artificial galaxies in the given point in the grid. The correction matrices are binned in three separate panels of concentration/Sérsic index and three separate panels of ellipticity. The colors of the arrows gives the amount of scatter shown by the individual models around the median correction: in green are grid points where all corrections are coherent in strength, in red are shown those which have a high scatter and hence our correction is representative on average but not for the single models. We use these maps to derive corrections for observed magnitude and sizes in the real ZENS galaxy sample. The choice of a discretized but dense grid allows us to pinpoint the correction/uncertainty maps at well localized positions on the considered planes. As indicated above, the corrections for any given real ZENS galaxy are obtained by interpolation at the position of the ZENS galaxy in the *observed*  $\epsilon - mag - R_e - n(C) - PSF$  space.

To discuss Figures 8 and 9 it is useful to identify three regions in the  $mag - R_e$  plane: (1) the region populated by models which are close to the surface brightness limit of the ZENS study (indicated with the dashed black lines in the plot), (2) the region of well-resolved, high-signal to noise ratio measurements, and (3) the region close or below the size of the PSF (highlighted with a gray horizontal line).

Above the detection and resolution limit, and at low ( $C < 2.5$ ,  $n < 1.5$ ) to intermediate ( $C \simeq 3$ ,  $n \simeq 2.5$ ) concentrations, both GIM2D and ZEST+ perform fairly well, and only small corrections are needed for both  $R_e$  and magnitude.

Not surprisingly, below the sky noise surface brightness, basically no galaxy can be recovered by both ZEST+ and GIM2D, as models are a priori not detected during the SExtractor source extraction (necessary to define the total galaxy flux and the initial guess for the size needed as input by ZEST+ and GIM2D). For galaxies with low concentration/Sérsic index, the detection rate falls rapidly to zero when the surface brightness limit is reached (no model with  $I_{AB} \sim 19$  and  $R_e \sim 10$  kpc is recovered); conversely, the centrally peaked light distribution in galaxies with higher concentration pushes the detection limit to slightly fainter surface brightnesses. Close to the surface brightness limit, magnitude and sizes are severely underestimated for both GIM2D and ZEST+ fits: sizes are typically smaller by more than a factor of two (three) and magnitudes are dimmer by half (one) magnitude for GIM2D (ZEST+) measurements.

At  $C > 3$ , the ZEST+ “aperture” measurements suffer from a strong underestimation of sizes and magnitudes at any signal-to-noise. This is a consequence of the well known tendency to miss a substantial fraction of the flux from the faint wings in steep light profiles when performing aperture photometry measurements. Integration to total light mitigates this effect in the GIM2D models, which nonetheless results in sizes which are about 30% smaller than the intrinsic ones for extended galaxies with steep light profiles ( $R_e \gtrsim 10$  kpc).

When moving close to the resolution limit of the survey, we notice further differences between the performance of ZEST+ and GIM2D. Thanks to the PSF deconvolution, the analytical fits are able to reliably recover the sizes also for models with sizes below the PSF FWHM.

Systematic effects become visible only at the worst observing condition (see Figure B2 in Appendix B). ZEST+ suffers from much stronger biases in this regime, causing an artificial increase of the size of models with  $R_e < PSF$  for any value of the seeing. We note however that our approach, being based on idealized, regular galaxy light distributions produced with GIM2D, may return in general an optimistically good performance of GIM2D than when recovering the parameters for real galaxies with irregular, clumpy light distributions. Our corrections are thus to be considered as the “minimal” correction functions that must be applied to the data to put the structural measurements on a comparable grid.

#### 6.4. The impact of the PSF on concentration and ellipticity measurements

Another clear effect observed for the ZEST+-based parameters is a lack of recovered parameters in the galaxy half-light radius  $R_e$  vs. magnitude plane at high concentrations and small radii (see right most panels of Figure 9); this becomes increasingly more severe at higher ellipticities and larger PSF FWHM (see also Figures B3-B4). A similar trend is observed for the GIM2D fits in the worst seeing conditions only at small radii (Figure B2). Note that, consistently, the distribution of the real ZENS galaxy measurements based on ZEST+ in Figure 9 presents the same bias.

The origin of such effect is investigated in Figure 10, which illustrates where the artificial galaxies, created in a given region of the parameter space, are placed in the *observed* space. In this map, the arrows indicate the direction in which models generated with a certain  $\epsilon$  and  $C$  are displaced relative to their intrinsic concentration and ellipticity: an upward-pointing arrow indicates that models are observed on average as less elongated, and a left-pointing arrow indicated that they are observed at lower concentrations. Intrinsic concentrations are calculated analytically from the original models Sérsic indices, and refer to the ratio of the radii containing 80% and 20% of the *Petrosian* flux (see e.g. Graham et al. 2005). In the same figure, red-to-yellow squares indicate points in the grid in which at least 50% (up to 100% for full red squares) of the artificial galaxies that are *observed* at that location originate from a different intrinsic concentration or ellipticity grid point. Green points in the figure indicate grid nodes which are not affected by either scattering of galaxies into the grid point from different intrinsic concentration/ellipticity panels, or by scattering of galaxies out of the grid point into a different panel of observed ellipticity and/or concentration.

It is clearly seen in Figure 10 that model galaxies which were originally generated at high concentrations and ellipticities have a high probability to be scattered into lower  $\epsilon$  and  $C$  bins by the aperture-based ZEST measurements; this bias is exacerbated at sizes  $\lesssim 2 - 3$  kpc. This is caused by the effect of the PSF convolution which artificially lowers a galaxy concentration and circularizes their axis ratio. Consequently, this ZEST+ region of the  $mag - R_e$  plane out to  $\sim 2$  PSF radii is highly degenerate, being populated by both galaxies which have intrinsic parameters in that location of parameter space, and by galaxies which are scattered into it from higher ellipticity and/or concentration regions. Given this degeneracy, it is important to verify to which extent the corrections

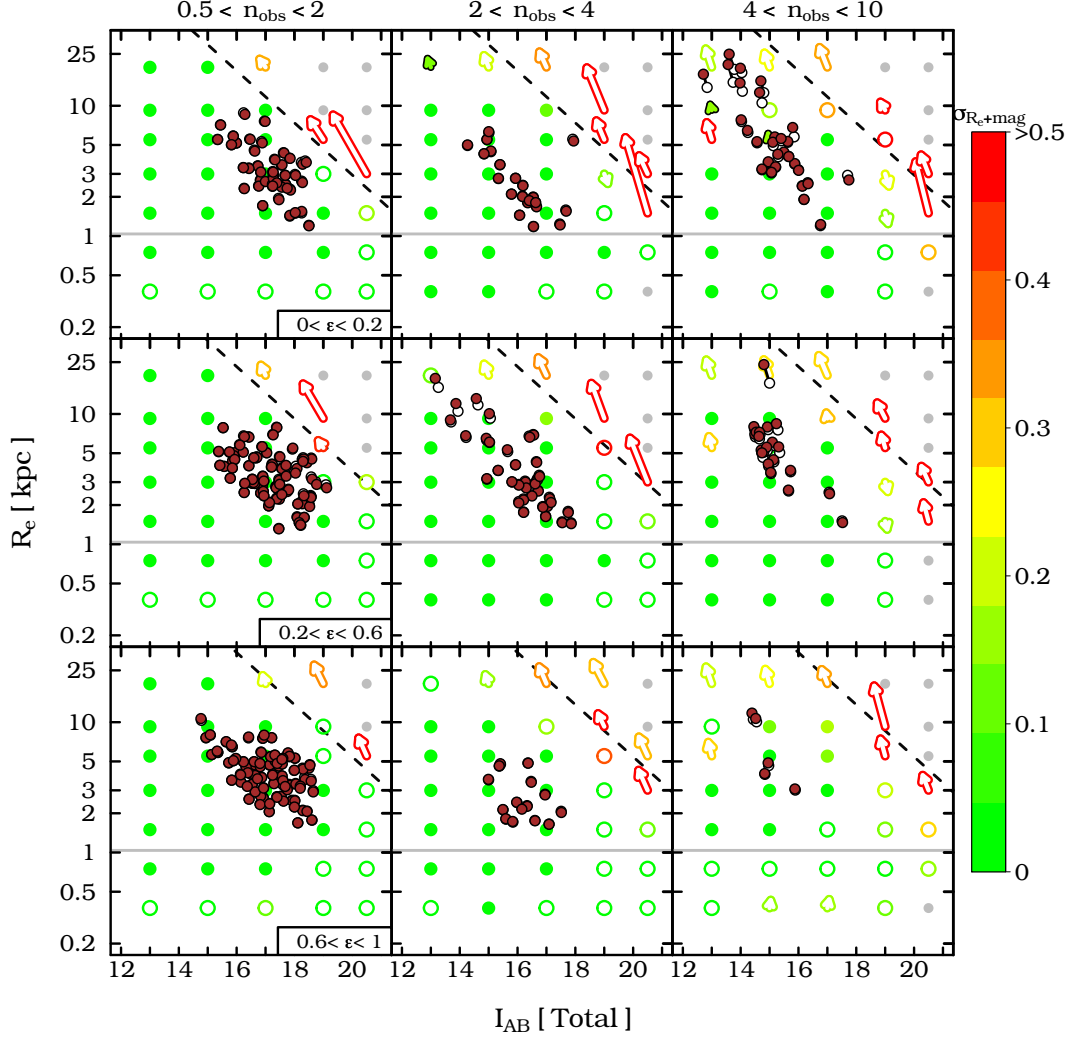


**Figure 8.** The size-magnitude plane with arrows illustrating the strength of the correction necessary, at each grid point, to recover intrinsic total magnitudes and sizes from the observed magnitude and sizes as measured by GIM2D in the ZENS *I*-band imaging. The corrections are based on single Sérsic fits to single Sérsic galaxy models; they are shown binned in three different panels of observed Sérsic index (from left to right) and three panels of observed galaxy ellipticity (from top to bottom). Arrows represent the direction and strength of the corrections at each grid point; they are obtained as the median difference in magnitude ( $\Delta m$ ) and radius ( $\Delta R_e$ ) between the input models and the measured parameters at the given grid point. Colored circles show positions in the plotted parameter space in which no corrections to magnitudes and sizes are required; these are defined as grid points in which 80% of the models have a correction in radius and magnitude which are, respectively,  $< 20\%$  and  $< 0.3$  mag. The colors of the arrows and circles indicate the amount of scatter in the individual contributing models relative to the shown median correction. The scatter increases from green to red and is defined as the quadratic sum of the median absolute deviations of  $\frac{\Delta R_i}{R_i}$  and  $\frac{\Delta F_i}{F_i}$ , with  $\Delta R_i$  and  $\Delta F_i$  the size and flux differences between each individual model at the corresponding median value. The precise values of the scatter around the medians at any color is given in the color chart on the right-hand side of the figure. Empty colored circles represent regions in the  $mag - R_e$  plane where the recovery of the models' ellipticity and Sérsic index is subject to large uncertainties; precisely, empty colored circles show those grid points in which at least 25% of the models have a difference between input and output  $\epsilon$  or  $n$  which is larger than 0.08 and 15%, respectively. The gray horizontal line marks the value of the typical PSF FWHM for the ZENS observations; the dashed black line highlights the surface brightness limit of our images. Gray dots highlight regions of incompleteness in the observed space, i.e., which are populated by less than 10 model galaxies. Corrected radii and magnitudes for the real ZENS galaxies that were observed with a seeing  $\sim 1''$  are plotted as small brown circles; for galaxies with magnitude-radii measurements falling on grid points with a correction arrow, we show as empty circles their pre-correction, raw measurements; corrections up to  $\sim 40\%$  had to be applied, in particular to galaxies with steep light profiles.

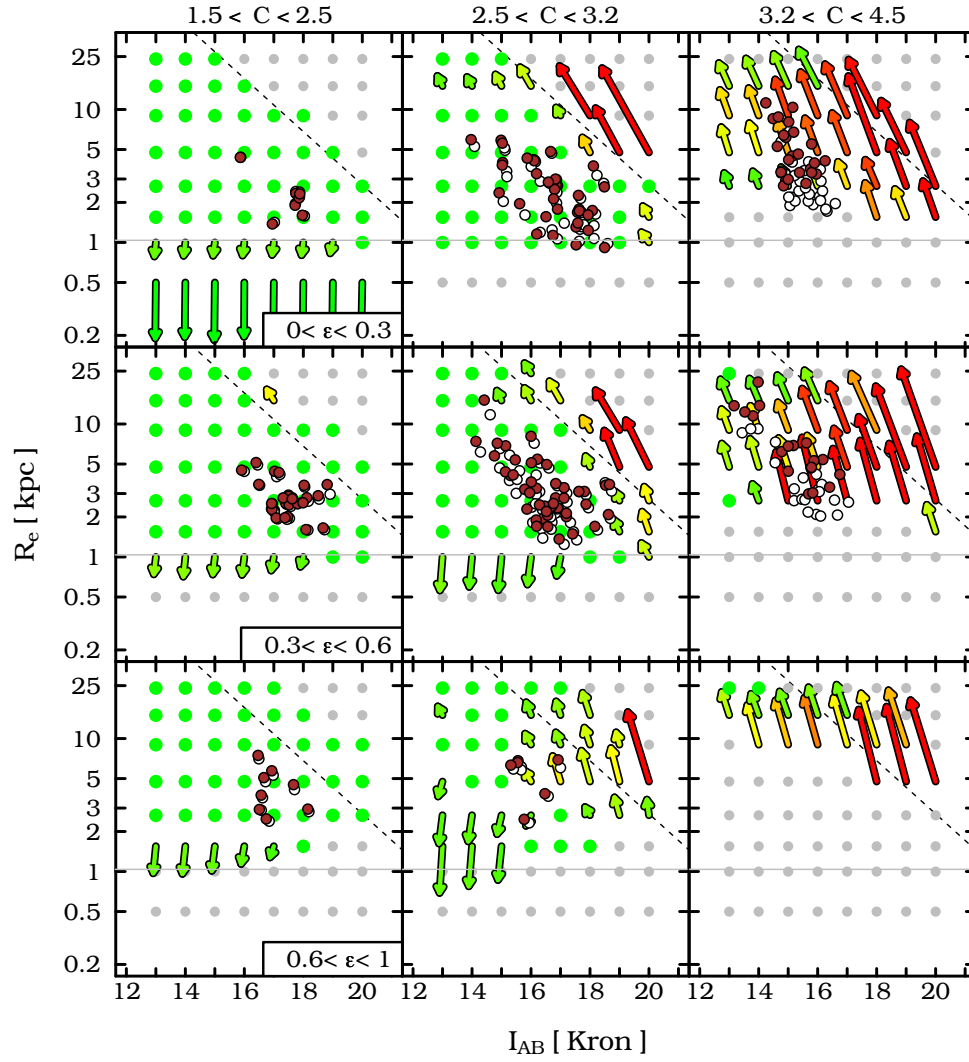


**Figure 9.** Same as Figure 8, but for measurements obtained with ZEST+. In this case, models and observed galaxies are binned in three panels according to the measured concentration index  $C$ . Colors and symbols are as in Figure 8. Note that the corrections are, as expected, more substantial than those shown in Figure 8 for the GIM2D-based measurements.

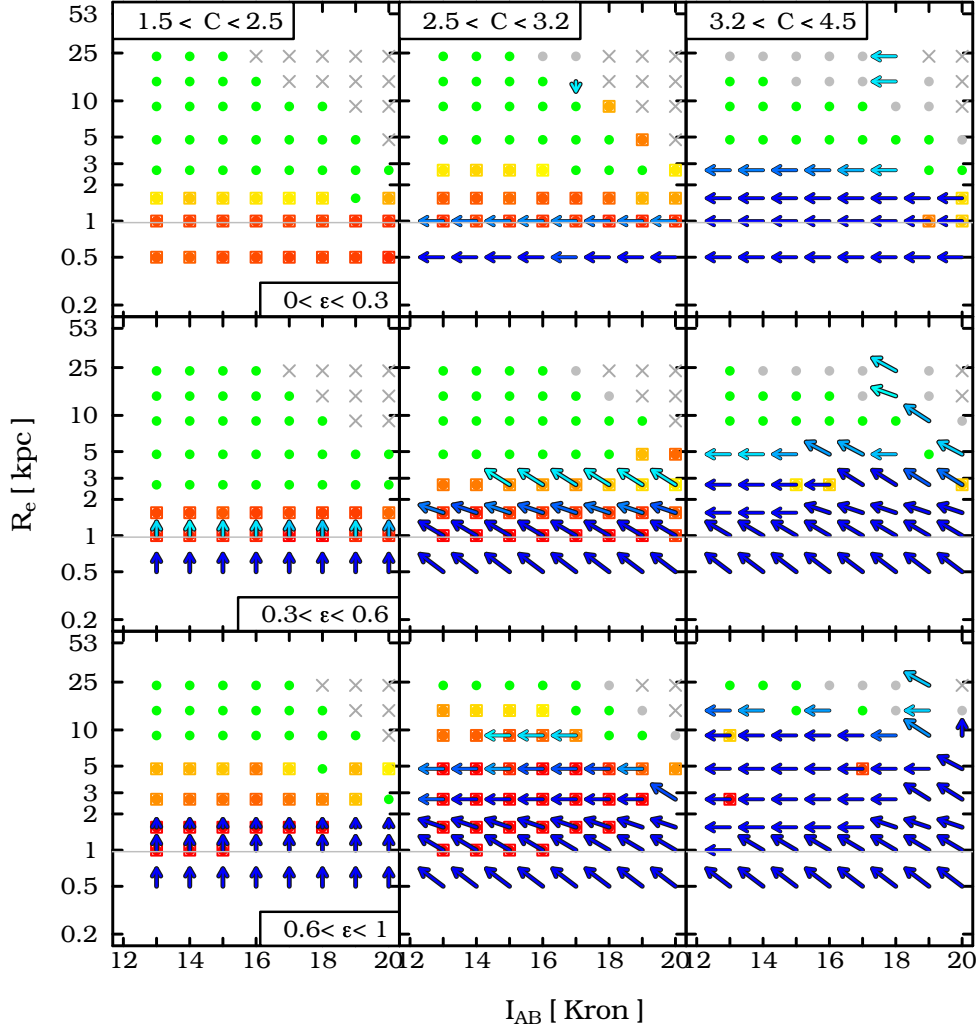


**Figure 10.** The size vs.  $I$ -band magnitude plane on which we show the effect of measurement biases on the recovery of galaxy concentration and ellipticity calculated with ZEST+. Colored arrows and squares indicate, respectively, the scattering of model galaxies out of their intrinsic  $C$  and  $\epsilon$  panels, and into a different panel of measured  $C$  and  $\epsilon$ : e.g., an upward-pointing arrow indicates that model galaxies with intrinsic parameters in that grid point are observed in a higher  $b/a$  ratio panel, while a left-pointing arrow indicates that the model galaxies are observed in a panel of lower concentration. An arrow is drawn on a grid point if at least 50% of the models that are generated at that given  $R_e - mag - \epsilon - C$  point are scattered out of it, into a different concentration or ellipticity panel; to draw the horizontal(vertical) component of the arrow, we further require that at least 25% of the scattered models change, when observed, panel of concentration(ellipticity). Blue shades become darker with increasingly larger fraction of objects which are scattered out of a given panel. The length of the arrows is arbitrary set for plotting purposes and has no specific meaning. With yellow square we show the points of the  $R_e - mag$  grid in which at least 50% of the *observed* model galaxies were generated in a different panel of intrinsic concentration or ellipticity (up to 100% in full red shade). Green points indicate grid nodes in the observed  $C$  or  $\epsilon$  parameter space which do not suffer from strong scattering of intrinsic model galaxies either into it or out of it. gray crosses and dots respectively highlight the grid points which are below the surface brightness limit of the ZENS study, and in which galaxy models with intrinsic  $C$  and  $\epsilon$  in those grid points are recovered by ZEST+ at a different radius and/or magnitude, but within the same concentration/ellipticity panel (i.e., at a different grid point within the same panel).

for radii and magnitude that we discussed above depends on the precise way in which the simulation grid is populated. If model galaxies which are “scattered in” and those which have intrinsic parameters in that location of parameter space required different corrections, then a precise modeling of the relative fractions of such galaxies in the given grid point would be needed. To test this, we created magnitude and sizes correction maps using either only artificial galaxies which were scattered into the given  $\epsilon - C$  bin, or only galaxies born in situ. We show the outcome of such an experiment for the median PSF in Figure B5 in Appendix B. Both realizations resulted in very similar corrections for size and magnitudes, indi-

cating that these are robust independent of the intrinsic concentration/ellipticity of the galaxies.

On the other hand, models which are scattered into lower  $C$  or  $\epsilon$  bins require by definition stronger corrections in  $\epsilon$  and  $C$  themselves than those which were generated within the bin. While for ellipticity it is reasonable to assume that also real (disk) galaxies would have a uniform distribution, and we hence can consider our corrections to be representative, the correction for concentration depends on the relative fraction of truly low concentration galaxies with respect to galaxies with a high intrinsic concentration. Given that we have a no priori knowledge of the true distribution of concentrations for

the real galaxies, and to avoid introducing biases associated to the choice of the simulation grid, we choose to follow a different method to correct the non-parametric structural estimators, which uses the available information on the Sérsic index. For data sets which do not have an as comprehensive set of measurements as ZENS, this approach could not be applied, and a statistical modeling of the underlying distribution of galaxies will be needed. These results should be taken as a cautionary note in using solely the concentration index as a morphological discriminant for galaxy types, especially if galaxies are close to the resolution limit of the given survey and if no correction to this parameter is attempted.

An equivalent map as in Figure 10, but for Sérsic indices and ellipticities measured by GIM2D (not shown) demonstrates only a marginal contamination/scattering of galaxy models across the broad ellipticity and  $n$  bins, thank to the PSF-deconvolution performed by the GIM2D fitting algorithm. Systematic effects are observed only for model galaxies convolved with the worst PSF of ZENS: in this case, models with high Sérsic indices and sizes smaller than  $\sim 1 - 1.5\times$  the PSF size are scattered to lower  $n$ . Interestingly, GIM2D tends to overestimate the ellipticity of such galaxies as opposed to what observed for the measurements performed with ZEST+. Given the little amount of contamination in these measurements, we apply to the ellipticities and Sérsic indices as measured by GIM2D the corrections obtained by interpolation between the relevant grid points of the previously discussed vector maps, which we regard as statistically representative of the average correction. Although under typical observing conditions the error on ellipticity and Sérsic index measured with GIM2D are small enough to keep model galaxies within the same bin in these parameters, moving closer to the resolution or detection limit of the ZENS WFI images increases the randomness in the measurements; inferred ellipticities and Sérsic indices have a typical scatter of  $\sim 0.1$  and  $20 - 30\%$ , respectively. We highlight these problematic regions with empty symbols in Figure 8.

#### 6.5. Corrections of non-parametric structural indices

To overcome the potential biases associated with calculating a correction for the *CASGM* parameters which is based on a distribution of structural properties for the input models which may not reflect the real one, we make use of the Sérsic indices of the galaxies from the GIM2D fits as priors to break the degeneracy. Sérsic indices are robustly determined in the vast majority of the models and are less prone to systematic biases, as discussed in the previous section.

The corrections for concentration, Gini and  $M_{20}$  indices are thus derived by splitting the artificial and real galaxies in similar bins of magnitude, radius, ellipticity and PSF as those employed for the size corrections (see Figure 9). In this case however we characterize the galaxy structure according to the observed Sérsic index rather than observed concentration, dividing the samples in three broad bins of  $0.2 < n_{obs} < 1.5$ ,  $1.5 < n_{obs} < 3.5$  and  $3.5 < n_{obs} < 10$ , respectively.

Following the same approach as for sizes and magnitudes, the corrections for non-parametric structural estimators are then defined as the median difference between the models' intrinsic indices and those calcu-

lated with ZEST+ at the given position in the observed  $mag - R_e - \epsilon - n - PSF$  parameter space. The intrinsic concentration is computed analytically from the input Sérsic index, as specified above, while for the Gini and  $M_{20}$  indices we use the measurements performed on “pure” models that are neither PSF-convolved nor degraded with the ZENS typical noise. Given that our analysis is based on intrinsically smooth and axisymmetric models, we do not attempt to correct the asymmetry and smoothness index. These quantities will nonetheless be affected (the smoothness possibly by the largest amount), and this caveat should hence be kept in mind. For the few ZENS galaxies for which no GIM2D fit is available, we applied an average correction obtained as the median of the correction for the ZENS galaxies having GIM2D fits and similar observed concentrations.

#### 6.6. Robustness of the bulge-to-disk decompositions

A similar approach as the one employed for the single Sérsic fits was used to test the reliability of the GIM2D bulge+disk (B+D) decompositions. All the B+D model galaxies were processed in exactly the same way as the real galaxies: i.e., after the decomposition, the output models were filtered to reject the unphysical fits and to identify acceptable B+D decompositions (see Appendix A.2). Consistently with the approach used for the real galaxies, only these were used for deriving the correction functions for the B+D parameters.

The correction maps for the B+D parameters are shown in Figure 11 and 12, for the three PSFs. For bulges, we present the results for all disk inclinations together, as no strong dependence on the model axis ratio was detected.

Both scale lengths and magnitudes of disks are very well recovered by the GIM2D code for most of the cases. Systematic deviations from the input parameters are observed only for very small disks (i.e.,  $h \sim 0.5\times PSF$ ), especially for the largest PSF size and in the low surface brightness limit, where disk scale-lengths are underestimated by a factor of about two, and the measured magnitudes are systematically fainter than the input ones, as already discussed above. Globally, in only  $\sim 10\%$  of the cases the normalized difference between input and output disk sizes is larger than  $\sim 50\%$ , and predominantly in the low surface brightness regime. Figure 11 shows that only very few ZENS disks fall in these problematic regions.

The bulge parameter are instead subject to much larger uncertainties, as illustrated in Figure 12. Although in many regions of the magnitude-size relation there are no systematic corrections, the scatter of measured bulge sizes around the input ones is generally large, typically  $\sim 30 - 40\%$  for the measured bulge half-light radii. The strongest differences between input and output model parameters are measured for bulges with high Sérsic indices ( $n \gtrsim 4$ ) in which case a substantial over-estimation of bulge effective radii is observed. Low Sérsic index bulges (leftmost panels in the Figure), on the other hand, suffer from smaller measurement errors. Below the resolution limit and for the worst PSF, sizes are over-estimated also for bulges with  $n < 4$  whereas the effect is less evident for the best or intermediate PSF.

These uncertainties in the bulges sizes reflects in (or are possibly generated by) a general difficulty in recov-

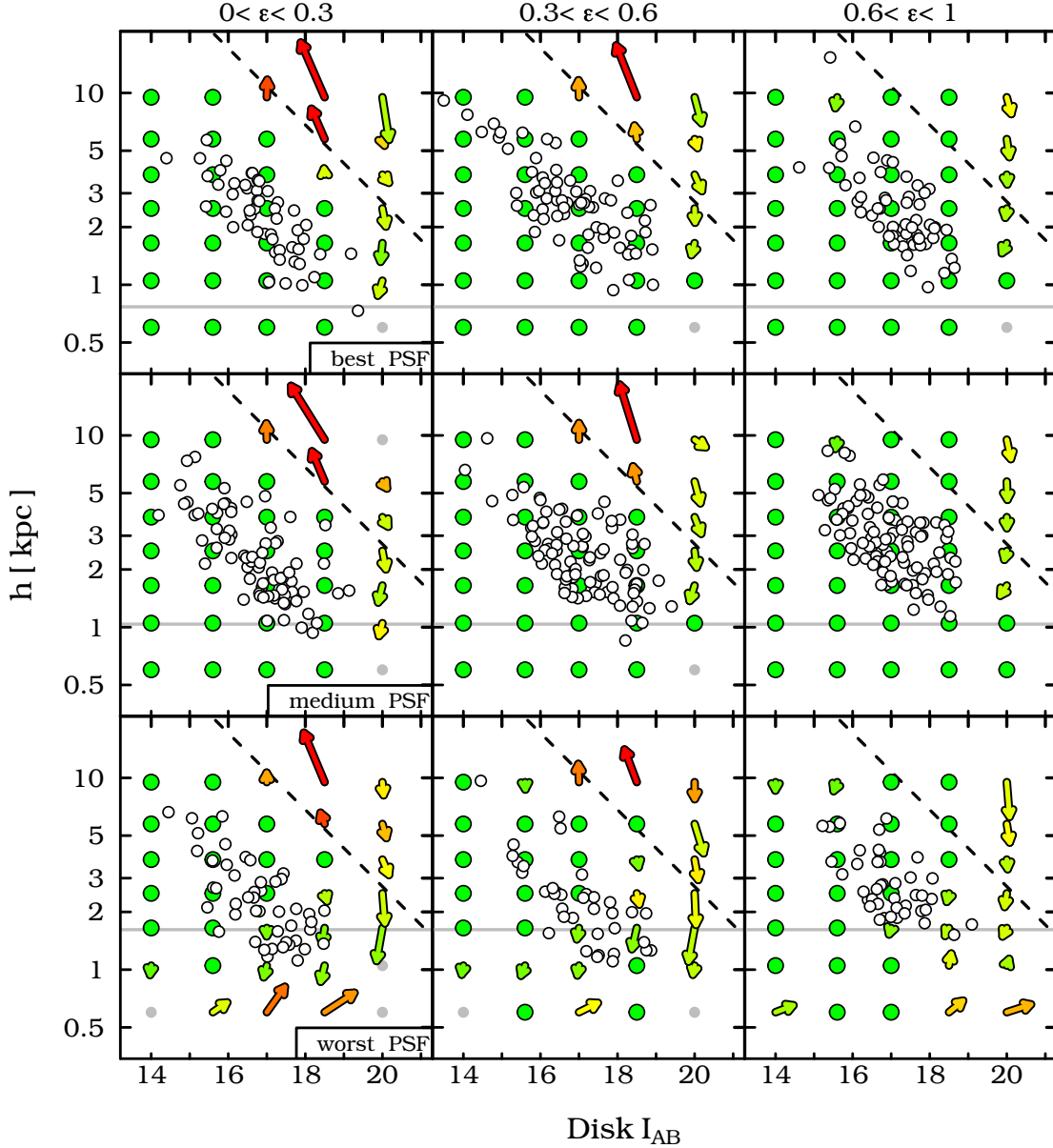


**Figure 11.** The disk scale length  $h$  vs. disk  $I$ -band magnitude plane, with highlighted the error vectors illustrating the systematic errors on the disk scalelength and  $I$  magnitude recovered by GIM2D relative to the intrinsic values. These vector maps are the results of our extensive simulations described in Section 6. Only models with measured bulge-to-disk ratio  $B/T < 0.80$  are considered in this figure. From top to bottom, the panels refer to the best, median and worst ZENS PSF. Results are presented, from left to right, in three bins of disk ellipticity. Colors and symbols are as in Figure 8. Small black empty circles indicate the real measurements for the disk components of ZENS galaxies.

ering the correct bulge Sérsic index. As an illustration of this fact, we plot on the top Panel of Figure 13 the comparison between input and measured bulge Sérsic indices for the median PSF. It can be noticed how the measured Sérsic index, especially below  $n \simeq 2$ , can deviate substantially from the model intrinsic values. This particularly severe for bulges with half-light radii which are close to the PSF size: small bulges with low index  $n$  can be misclassified as bulges with larger half-light radii and steeper light profiles.

Although the structural properties of the bulges are subject to relatively large uncertainties, the fractional contribution of the bulge to the total light is generally well measured by the GIM2D decompositions, as shown

on the middle panel of Figure 13. In the bottom panel we plot, for a given value of the observed bulge-to-total ratio, the fraction of input models which where originated with a  $B/T$  which differed less than 0.15 from the measured one, between 0.15 and 0.3 and more than 0.3 (black, gray and red lines respectively). In  $\sim 80$ -85% of the cases the bulge-to-total ratio is recovered within a scatter of 0.15 and really catastrophic failures ( $\Delta(B/T) > 0.3$ ) happen in  $\lesssim 10\%$  of the models. It is worth to notice that the fraction of galaxies for which the  $B/T$  is robustly recovered is largely independent of the value of  $B/T$  itself, and the typical scatter around the input bulge-to-total ratio is of order  $\sim 0.1$ . Problematic fits which results in large differences in  $B/T$  are again mostly associated with flat



( $n < 2$ ) and small ( $R_e < 1\text{ kpc} \simeq \text{PSF}$ ) bulges, for which is difficult to disentangle the disk component from the small, disk-like bulge.

In the light of these results we decided *not* to apply any corrections to the bulge and disks structural parameters: on one hand disk sizes are well recovered by the GIM2D fits, hence no substantial correction is needed, on the other the large scatter in the recovered bulge half-light radii and Sérsic indices make the derived corrections noisy and dependent on the specific sampling of parameter space with our simulations. For this reason, we prefer to use the direct output from GIM2D for the bulge half-light radii, but with associated a typical uncertainty of 30%, as estimated from our tests.

### 6.7. Testing the robustness of the applied corrections

We present a number of diagnostic tests that we performed to verify the reliability of the corrections for the structural parameters that are described in Section 6.3 and 6.5.

As a first sanity check we run our correction scheme, in exactly the same fashion as for the real galaxies, on the measured properties for the models themselves; the outcome of this exercise is illustrated in the upper panels of Figure 14 for sizes obtained with GIM2D and ZEST+, for models convolved with the median PSF. The intrinsic (input) and corrected radii for the model galaxies agree very well, and systematic biases that are present in the uncorrected sizes are largely cured by our correction scheme. Furthermore, the large discrepancies between the ZEST+ and GIM2D raw measurements disappear in the corrected data.

The bottom panels in Figure 14 show the comparisons of ZEST+ and GIM2D half-light radii, ellipticities and  $I$ -band magnitudes, before and after the application of our correction schemes for the real ZENS galaxies. The raw sizes derived by ZEST+ are systematically smaller than those obtained by the GIM2D fits, by up to a factor of  $\sim 2 - 3$  in the worst cases. Our correction scheme nicely brings the two estimate into a very good agreement. As a consequence of the PSF convolution, galaxies are also measured to be rounder in ZEST+ than in GIM2D, especially at low radii, a bias which is largely cured by the implementation of the correction scheme. The latter also mitigates the underestimation of the total fluxes in ZEST+.

We also note that (disk) galaxies with low concentrations and/or low values of  $n$  Sérsic index, which we have shown to require very modest or no corrections to their sizes, well match the Sloan measurements of sizes presented by Shen et al. (2003) (see Figure A2 in Appendix A, where we show the mass-size relation for the ZENS galaxies compared with Shen’s data, separately for early- and late-type galaxies; the masses for our galaxies are taken from Paper III). We also show in the same Appendix that early-type galaxies with steep light profiles, which do require a correction to their sizes, lie slightly above the median values for the early-types reported by Shen et al.

The comparison between uncorrected and corrected  $I$ -band  $C$ , Gini and  $M_{20}$  indices is shown in Figure 15. Specifically, to test whether our corrections deal properly with PSF-induced biases, we compare, for corrected and uncorrected measurements, the distributions

of these parameters for two bins of PSF size, i.e., PSF  $FWHM < 0.9''$  and  $> 1.1''$ , respectively. The uncorrected indices show different distributions for galaxies observed with small or large PSF’s FWHM. The effect is mostly evident for the concentration parameter, for which a two-sided Kolmogorov-Smirnov test rejects the possibility that the low and high FWHM samples are drawn from the same parent distribution at the 97% confidence level. A similar effect is also noticeable for the  $M_{20}$  index; the Gini coefficient is instead less sensitive to PSF blurring. All such biases disappear once our corrections are applied, as shown in the lower panels of the same figure. The inspection of the distributions of Figure 15 furthermore shows that the corrections produce a second peak of high  $C$  values for the early-type galaxies, which would otherwise be absent from the raw measurements; similarly, a corresponding peak at “more negative” values appears in the corrected  $M_{20}$  distributions.

This is also highlighted in Figure 16, where we show the comparison between corrected and uncorrected non-parametric structural estimators and the corrected Sérsic indices. The upper-left panel shows the comparison for the concentration index: the solid red line marks the expected values of the concentration inside the Petrosian radius for a perfect Sérsic profile of a given index  $n$ . It is clear that before correction, the measured concentration flattens rapidly at values  $\sim 3 - 3.5$  for  $n \geq 3$ , lying far away from the theoretical line. After applying our correction, the measured points well match this line. A similar adjustment is also observed for the  $M_{20}$  index, while, as already mentioned, the Gini coefficient requires vanishing corrections. The central and right upper panels show the dependence on ellipticity of uncorrected concentration and  $M_{20}$  parameters for galaxies classified as disks in Section 7; the artificial lack of high concentration galaxies at high elongation is largely removed by our correction scheme.

We finally note that all our corrections are clearly “statistical”. For example, individual models can retain an underestimation of the radius of up to a factor 30%, especially models close to the surface brightness limit of the ZENS observations. Nevertheless, in a statistical sense, our correction schemes return well-calibrated measurements that can be robustly compared with each other.

## 7. A QUANTITATIVE MORPHOLOGICAL CLASSIFICATION FOR THE ZENS GALAXIES

### 7.1. Classification Criteria

The availability of a large suite of structural diagnostics for the ZENS galaxies enables us to perform an accurate and quantitative morphological classification, eliminating biases and dilution of signal in studies of galaxy properties as a function of morphology.

We classified the ZENS galaxies into six morphological classes, primarily based on the prominence of the bulge component in the  $I$ -band. These classes are, respectively, ellipticals, bulge-dominated disks – further divided into S0 and bulge-dominated spirals – intermediate-type disks, late-type disks and irregular galaxies. The stamp images of the galaxies of different morphological types are shown in Figures C1-C8 in Appendix C. A flow-chart schematic description of the steps applied in our morphological classification scheme is shown in Figure 17, in which we also list the frac-



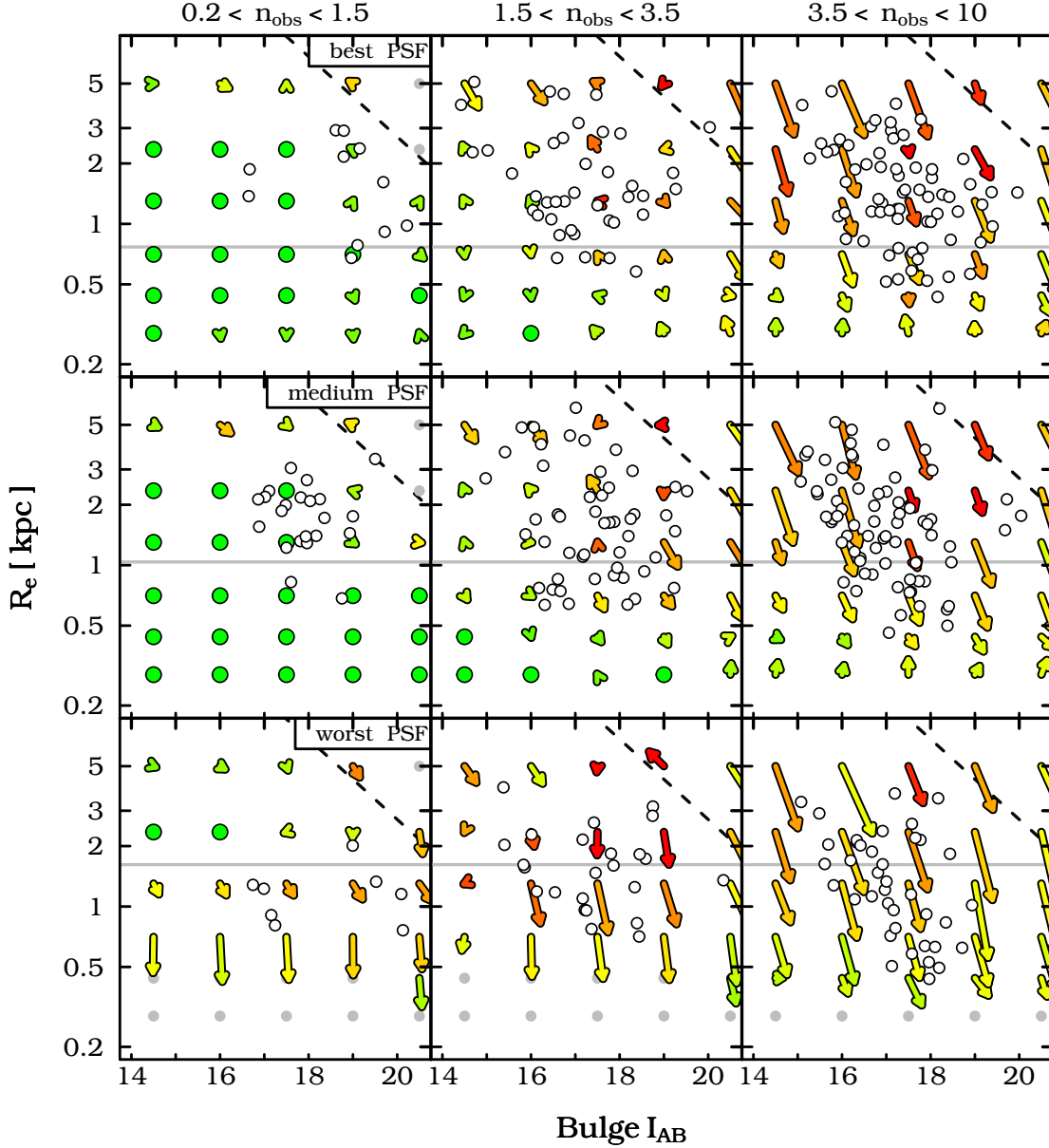


**Figure 12.** The bulge half-light radius  $R_e$  vs. bulge  $I$ -band magnitude plane, with highlighted the error vectors illustrating the systematic errors on the bulge radii and magnitudes recovered by GIM2D relative to the intrinsic values. Only models with measured bulge-to-disk ratio  $0.1 < B/T < 0.80$  are considered in this figure. From top to bottom, the panels refer to the best, median and worst ZENS PSF. Results are presented, from left to right, in three bins of Sérsic indices. Colors and symbols are as in Figure 8. Small black empty circles indicate the real measurements for the disk components of ZENS galaxies.

tion of each morphological type in the first-epoch ZENS database.

In detail, our classification criteria are as follows. Ellipticals are required to be well fitted by a single Sérsic profile with *corrected*  $n > 3$  and normalized residuals smaller than 10% out to the sky level of the image (see e.g. Kormendy et al. 2009). We present the  $I$ -band surface brightness profiles for all elliptical galaxies in Figure C2: the light distribution of such galaxies is perfectly represented by a single (corrected)  $n > 3$  Sérsic component.

The distinction among different disk types is based on the following criteria: galaxies with  $B/T(I) < 0.2$  are assigned to the late-type disk class, those with  $0.2 \leq B/T(I) < 0.5$  are classified as intermediate-type disks

and those with  $B/T(I) \geq 0.5$  as bulge-dominated galaxies. For many reasons, including a good degree of mixing of physical classes in the visual classification of the Third Reference Catalog (RC3, de Vaucouleurs 1963), we will refrain from using its popular nomenclature. We note however that, albeit with scatter, our bulge-to-total separation for disk galaxies roughly corresponds to a division in types S0, S0a/Sa, Sab/Sbc and Sc/Sm.

Both S0 and spiral galaxies with large bulges fall in the bulge-dominated galaxies category. The distinction among the two is based on the  $B$ -band smoothness parameter ( $S_{B\text{-band}}$ ), which is set to  $< 0.01$  for S0 and larger than this value for early-type spirals, except in those case where faint spiral arms – not prominent enough to cause a variation of the smoothness param-

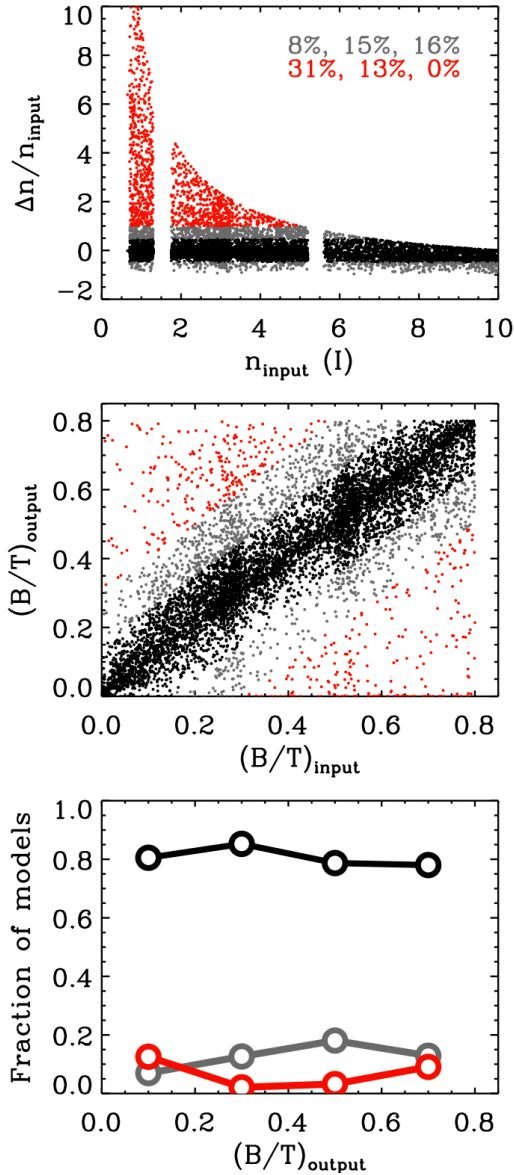


**Figure 13.** In the top panel we show the comparison between the intrinsic bulge Sérsic indices for the set of simulated galaxies used to test the reliability of GIM2D bulge+disk decompositions, and those recovered by GIM2D. The variation  $\Delta$  corresponds to the difference between the intrinsic and measured values. With black points we highlight models for which the structural parameters are well recovered, i.e., have relative error less than 50%. In gray are the points which have a fractional error between 50% and 100%, and in red are the extreme outliers with errors which are larger than 100%. The reported fractions are the fraction of discrepant models relative to the total in the three bins of Sérsic index  $n$  shown in the Figure. In the central panel we show the comparison of intrinsic and measured bulge-to-total ratios  $(B/T)$  for the model galaxies. Black shows models for which  $|\Delta(B/T)| < 0.15$ , gray those with  $0.15 < |\Delta(B/T)| < 0.3$  and red is for models for which the measured  $B/T$  deviates more than 0.3 from the intrinsic value. The fraction of models within each of the three types, as a function of the observed  $B/T$ , is shown in the bottom panel.

eter – are clearly seen in the visual inspection of the images. For nearly edge-on system it is obviously impossible to determine the presence or absence of spiral arms and the difference between S0 and bulge dominated spiral galaxies becomes less clear. Given that we have no means to securely distinguish these morphological types at these inclinations, we assigned to the bulge-dominated spiral class those galaxies which satisfy the  $B/T$  criterion above, and either present a dust lane in the disk plane or have a high  $B$ -band smoothness parameter ( $S_{B\text{-band}} > 0.01$ ). As seen in Figures C3 and C4, a large fraction of the highly-inclined galaxies are classified as bulge dominated spirals, and only those which clearly do not have a dusty disk are defined as S0. The contamination of S0 galaxies into the bulge-dominated spiral class is hence likely non-negligible at the highest inclinations.

The distinction between S0 and elliptical galaxies is also non trivial, this time especially in face-on systems. To attempt to distinguish between these two classes we inspected all the residuals of the single component fits and any sign of a faint disk component was used as a discriminant diagnostic. Finally the  $B$ -band smoothness  $S$  parameter was used to further validate the separation between the two types, by requiring that for S0  $S_{B\text{-band}} > 0.003$ , a condition which is however secondary to the fact of S0 not being perfectly fit by a single Sérsic model.

We note that for 18% of all ZENS galaxies that were not classified as ellipticals or irregulars, and that would therefore be assigned a “disk” classification, it was not possible to obtain a reliable  $I$ -band bulge+disk decomposition (see Appendix A). In these cases the classification is based on the corrected Sérsic indices from the single component fits, as shown in the right hand side of Figure 17. For the very few galaxies ( $\sim 1\%$ ) for which we could obtain no reliable bulge+disk decomposition or Sérsic index, we used the *corrected* ZEST+ parameters (specifically the concentration) to define their morphological class. Specifically, in such few cases, galaxies with  $C < 2.8$  were assigned to the late-type disk class, those with  $2.8 < C < 3.3$  to the intermediate-type disks and galaxies with  $C > 3.3$  to the bulge-dominated spiral class. The values of these cuts are determined through the relation between  $n$  and  $C$  in Figure 18.

Irregular (i.e., thus possibly disturbed by mergers/encounters) galaxies are identified in the ZENS sample by visual inspection; in this category we include those galaxies which have no clear disk/bulge component or have a highly disturbed morphology characterized by multiple clumps, as shown in Figure C8.

There are furthermore eight galaxy-pairs in the first-epoch ZENS sample which are also plausibly undergoing a merger, of which we present stamp images in Figure C8. These galaxy-pairs are identified as single objects in 2dFGRS, and appear as single members in the group catalog, i.e., they have only one redshift measurements in the 2dFGRS catalogue. For three of such couples, we confirmed with SDSS (York et al. 2000) spectral or photometric redshifts, or with spectroscopic data available in the NED database, that the two galaxies are at the same redshift, hence in the process of merging. For the remaining five galaxies, for which no such information is available, we note that two pairs show clear tidal features and disturbed morphologies, supporting the merger sce-

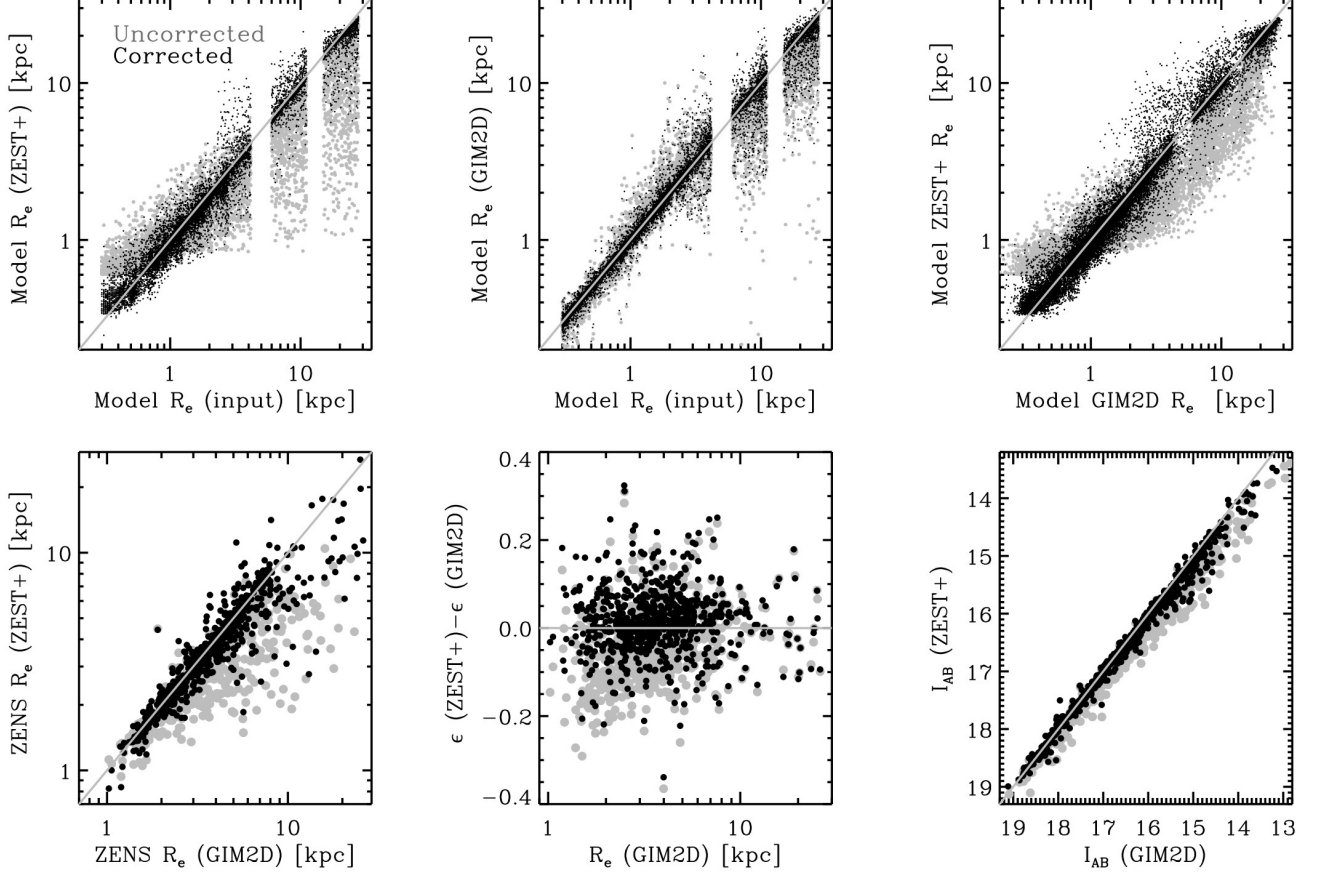


**Figure 14.** Tests of the correction scheme outlined in Section 6 both for the GIM2D and ZEST+ measurements on simulated (top panels) and real ZENS data (bottom panels). In all panels, black symbols are the corrected measurements and gray the raw, uncorrected measurements. The top panels specifically show the comparison between intrinsic (input) half-light radii of simulated galaxies versus half-light radii recovered with ZEST+ (left) and GIM2D (center), and the comparison between ZEST+ and GIM2D half-light radii (right). The identity lines (shown in gray) are well matched by the corrected sizes, with systematic shifts largely cured by our correction scheme. The bottom panels show the application of our corrections to the real ZENS data. Specifically, we show the comparison between ZEST+ and GIM2D half-light radii measurements, the ellipticity differences between ZEST+ and GIM2D as a function of (corrected) GIM2D half-light radius, and the comparison between  $I$ -band magnitudes recovered by ZEST+ and GIM2D. Also in these case, large discrepancies observed in the raw measurements vanish once we apply our correction scheme.

nario; the remaining three pairs display less clear signs of interactions, and hence for them a chance projection cannot a priori be excluded. We will include nonetheless the latter in the sample of merger galaxies and, when necessary, test our results with and without these systems.

For consistency with the original 2dFGRS and 2PIGG catalogs, we count the merging galaxies as a single galaxy pair system in the sample of 769 galaxies, but we compute and provide photometric/structural properties for the individual members, as well as those for the combined pairs when relevant. In the “normal” disk population, there are furthermore some galaxies which present clear tidal features and disk distortions; such galaxies are flagged as having plausibly undergone a recent galaxy-galaxy interaction or merger. The properties of merger galaxies in the ZENS sample and the connection with the local and large scale environment are investigated in Pipino et al. 2012 (in prep., Paper VI)

### 7.2. Structural properties of the different morphological classes

Our morphological classification scheme is primarily based on a bulge-to-total ratio separation. We inspect in Figure 18 the distributions of the *corrected*  $C$ ,  $n$ , Gini and  $M_{20}$  for the various morphological classes, and we summarize in Table 2 the median values of these corrected non-parametric diagnostics for each morphological class, separately in three bins of ellipticity (i.e., inclination for disk galaxies). Note that the six morphological classes largely segregate in specific region of the structural planes. Again we stress that this consistency between B/T and non-parametric diagnostics is reached only after correcting the latter as described in Section 6: the raw measurements before the implementation of the corrections would substantially mix different galaxy populations (e.g., through biased concentration and  $M_{20}$  estimates, see Figures 15 and 16) – a bias which we believe affects most other published analyses based on (uncorrected) non-parametric diagnostics.

There are of course some noticeable deviations which remain, even after correcting the non-parametric diagnostics. A small number of galaxies classified as intermediate- or late-type disks have low  $M_{20}$  indices for

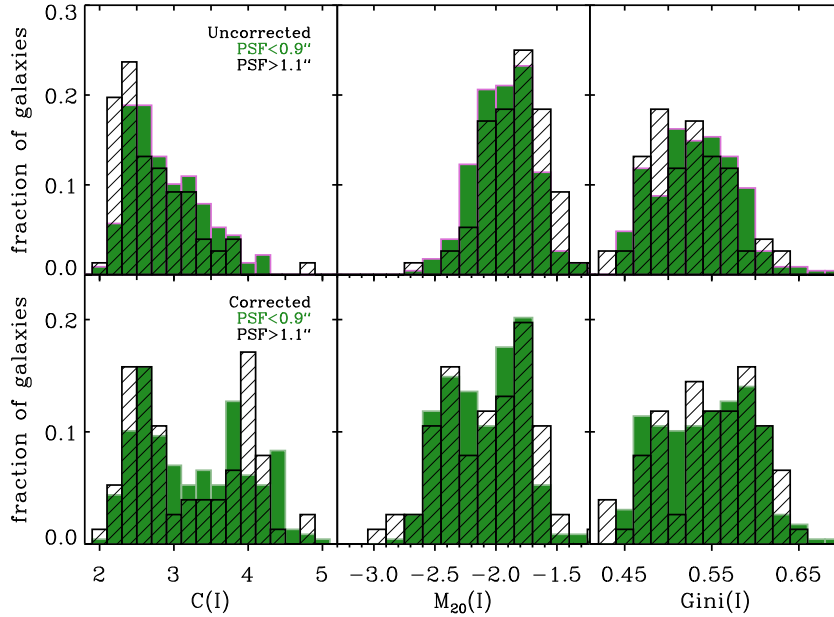


**Figure 15.** Comparisons of the distributions of ZEST+ concentration (left),  $M_{20}$  (center) and Gini (right)  $I$ -band parameters before (top row) and after (bottom row) the application of our correction scheme to eliminate PSF-induced biases. The distributions are shown for two separate bins of PSF FWHM, i.e., FWHM  $< 0.9''$  (green histograms) and FWHM  $> 1.1''$  (black histograms). Galaxies observed with smaller PSF appear more concentrated than those observed with a larger seeing, a consequence of the blurring of the structural features caused by the PSF. Also, the effect of PSF-blurring is to move high-concentration, highly-negative  $M_{20}$  galaxies to lower concentration, less negative  $M_{20}$  regions of parameter space. Both biases are eliminated by our correction scheme.

**Table 2**  
Median values of the corrected structural diagnostics for the different morphological classes in bins of ellipticity

Type	$\langle C \rangle$	$\langle \text{Gini} \rangle$	$\langle M_{20} \rangle$	$\langle S \rangle$	$\langle n \rangle$	$\langle B/T \rangle$
E	4.11/-/-	0.60/-/-	-2.44/-/-	0.004/-/-	5.06/-/-	-/-/-
S0	4.28/4.28/-	0.61/61/-	-2.50/-2.57/-	0.006/0.006/-	5.22/ 4.62	0.60/0.6/-
Bulge-dom. Spiral	3.91/3.87/4.07	0.60/0.60/0.62	-2.28/-2.36/ -2.51	0.060/0.042/0.12	3.83/3.89/3.80	0.59/0.56/0.60
Interm.-type Disk	3.56/3.40/3.18	0.56/0.55/0.56	-2.20/-2.11/-2.14	0.026/0.051/0.11	2.81/2.33/2.00	0.36/0.35/0.32
Late-type Disk	2.56/2.56/2.56	0.49/0.49/0.51	-1.79/-1.79/ -1.80	0.046/0.058/0.089	1.11/1.11/1.10	0.03/0.05/0.03

**Note.** — The median values of the corrected non-parametric diagnostics measured in the three ellipticity bins  $\epsilon < 0.33$ ,  $0.33 < \epsilon < 0.55$  and  $\epsilon > 0.55$ , from the lowest to the highest ellipticity. Note that Ellipticals and S0s have only one and two bins of ellipticity, respectively. Note also that the dependence on ellipticity of non-corrected  $C$  and  $M_{20}$  values for disk galaxies shown in Figure 16 is largely eliminated by our correction scheme.

their concentration or Gini values, overlapping with the region of the plane which is mostly occupied by irregular galaxies. We visually inspected all these galaxies and verified that the  $M_{20}$  deviations are mostly caused by the presence of bright clumps in the galaxies outskirts, but that a clear and ordered disk structure is present (we highlight these galaxies with a “\*” in Figures C5-C6).

Also, some intermediate-type disk galaxies have relatively high concentration values ( $C(I) > 4$ ). This demonstrate that concentration is *not* necessarily a proxy for the fractional contribution of the bulge component to the stellar light, as also pointed out by other authors (e.g. Scodreggio et al. 2002). There is, of course, a correlation between  $B/T$  and  $C$  characterized by a linear correlation coefficient of  $\mathcal{R} = 0.81$ . However, the scatter is large and a given concentration value can be associated with a broad range of  $B/T$  ratios, as illustrated in the top right

panel of Figure 19. We emphasize that the *uncorrected* values of concentration lead to a much larger scatter, which results in a weaker correlation between  $B/T$  and uncorrected  $C$  with  $\mathcal{R} = 0.61$ . We highlight with colors in Figure 19 two regions of parameter space which are worth noticing, i.e., that of galaxies with  $B/T < 0.35$  and  $C > 3.5$  (red points) and that of  $C < 3.5$  and  $B/T > 0.45$  (blue points). As illustrated in the bottom panels of the same figure, highly concentrated galaxies with low  $B/T$  ratios are found below the bulk of the population in the relation between the bulge half-light radius and the disk scale length; the Sérsic indices of their bulges are in most of the cases ( $\sim 70\%$ ) above 2.5. Such objects hence host dense but small bulges, which are causing an increase in the concentration value but do not give a major contribution to the total galaxy light. The blue points at low  $C$  and high  $B/T$ , in contrast, are galaxies with typically

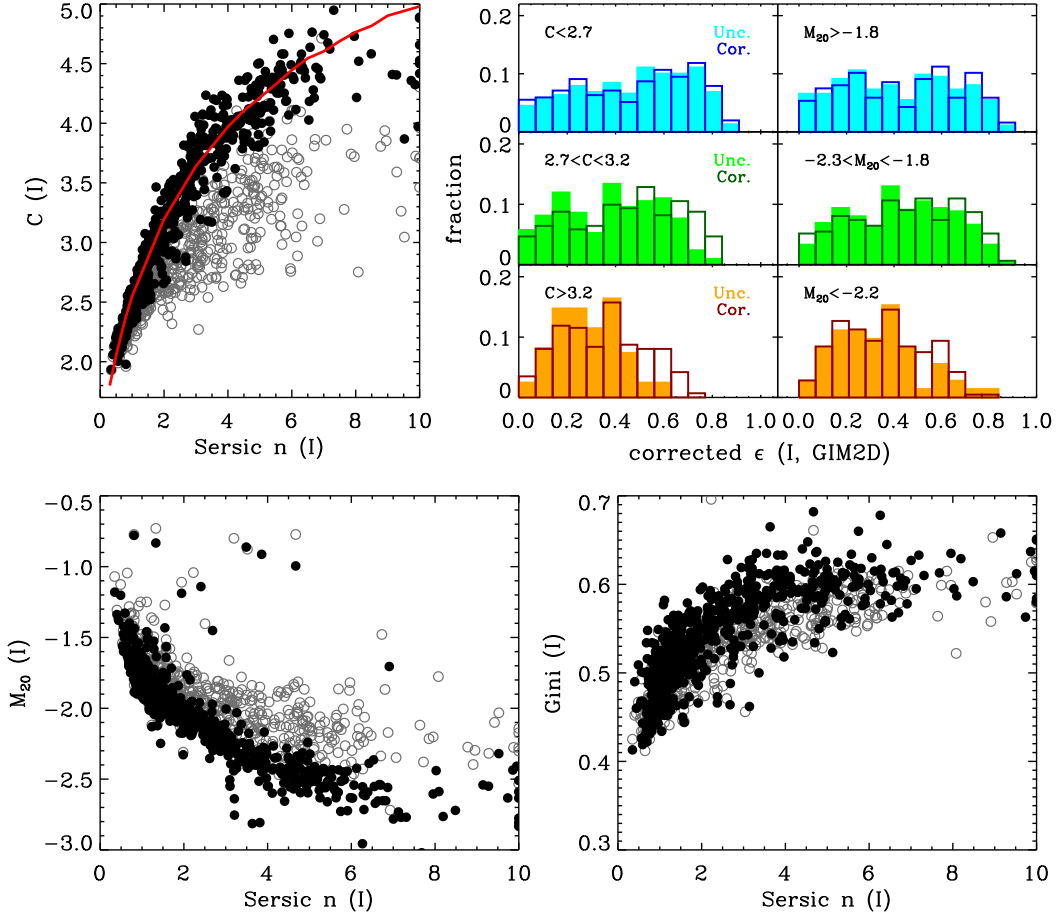


**Figure 16.** Relation between  $I$ -band Sérsic index  $n$  and non-parametric structural quantities, i.e.,  $C$ ,  $M_{20}$  and Gini coefficients before and after applying our correction scheme, described in Sections 6.5 and 6.3 (top left panel and bottom panels). gray points show the uncorrected measurements and black points the corrected measurements. In the upper left panel the solid red line marks the values of the concentration index which are theoretically expected for a pure Sérsic profile of a given  $n$ . Both  $C$  and  $M_{20}$  require substantial corrections, while the Gini coefficient is largely unaffected by observational biases. The upper central and right panels finally show, for galaxies classified as disks in Section 7 (S0 and later), the dependence of uncorrected and corrected concentration and  $M_{20}$  parameters on ellipticity. Specifically, we present the distribution of ellipticity for galaxies divided in three bins of concentration and  $M_{20}$ , as indicated by the Figure legend. The filled light histograms are for the uncorrected parameters, the dark empty ones for the corrected indices. The uncorrected  $C$  and  $M_{20}$  values show a bias with  $\epsilon$  which is removed by our correction procedure.

extended bulges with low Sérsic index (i.e., pseudo-bulge like structures, see e.g., Carollo 1999; Carollo et al. 1998, 2007 and Kormendy & Kennicutt 2004 for a review and further references).

In Figure 20 we furthermore show the different corrected structural indices for the morphological classes, as a function of the galaxy inclination. The distribution of corrected parameters for each individual class are fairly flat with ellipticity, as they should (in contrast with the non-corrected parameters, which we have shown to have a bias with ellipticity; see Section 6.7 and Figure 16). Note the galaxy smoothness maintains a substantial dependence on inclination by increasing towards higher inclinations; this parameter has not been corrected, since we used only smooth galaxy models to determine our correction matrices. Part of the dependence of  $S$  on ellipticity might thus be a residual observational bias; part might however be a consequence of the prominence of dust lanes in edge-on galaxies.

Dust absorption in the disk could also in principle arti-

ficially lower the derived bulge-to-total ratios for edge-on galaxies (see for example Driver et al. 2007), and hence introduce a bias in the B/T-based morphological classification. We expect this effect to be minimal in our analysis, since we use the relatively unaffected  $I$ -band to derive our fiducial  $B/T$  estimates, but it is nonetheless worthwhile to test whether there are indication of biases among the morphological classes. In the lower right panel of Figure 20 we plot the distributions of ellipticity for disk galaxies with bulge-to-total ratio  $< 0.2$  (blue histogram),  $0.2 < B/T < 0.5$  (green histogram), and  $0.5 < B/T < 0.8$  (red histogram).

For  $\epsilon \lesssim 0.6$  we find a reasonable constancy with ellipticity of the relative contribution of three disk types to the total disk population, indicating that there are no major biases in this regime. At higher axis ratios, there is a depletion of  $B/T > 0.2$  galaxies and an increase of the "bulgeless" disk galaxies, which we however interpret mostly as a consequence of a true change in the morphological mix and of uncertainties in the elliptic-

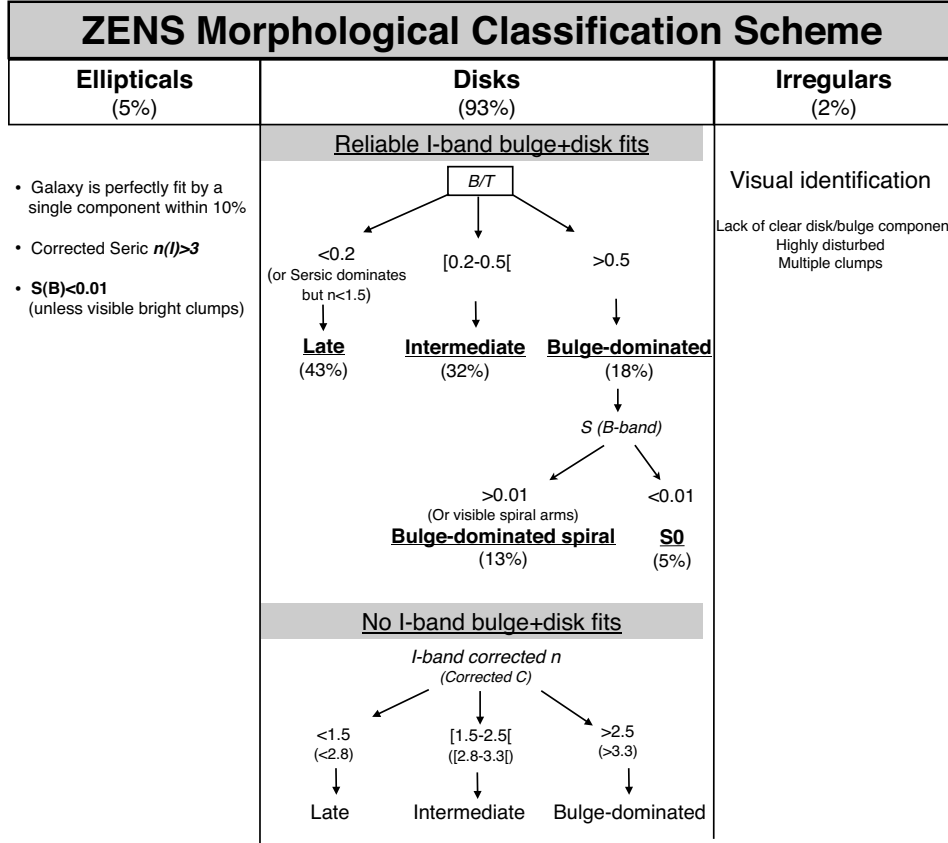


**Figure 17.** Schematic description of the steps adopted for the ZENS morphological classification. The numbers in parenthesis provide the fraction of galaxies assigned to the different morphological classes with respect to the total first epoch ZENS sample.

ity measurements rather than of strong dust absorption. The decrease in the number of bulge-dominated galaxies and intermediate-type disks at  $\epsilon \gtrsim 0.6$  reflects the fact that the ellipticity is a morphological indicator: by definition highly flattened galaxies do not host big bulges (see also the other panels in the Figure). Likewise, the peak of  $B/T < 0.2$  disk galaxies at  $\epsilon \simeq 0.7$  can be explained by the “rounding” of isophotes due to PSF effects in these galaxies and the intrinsic galaxy thickness. Indeed no galaxy is observed at  $\epsilon > 0.87$  and the fraction of  $B/T < 0.2$  disk galaxies at  $0.6 < \epsilon < 0.87$  relative to the total sample of disk galaxies is  $\sim 24\%$ , i.e., if they were (infinitely thin disks and) equally distributed up to  $\epsilon = 1$ , each of the four 0.1-wide bins between  $0.6 < \epsilon < 1$  would contain 6% of the sample, which is the average number observed at lower axis ratios. Together with the constancy of the median  $B/T$  ratio for the different morphological classes in three ellipticity bins show in Table 2, these considerations lead us to conclude that our  $B/T$  measurements are largely independent of axis ratio and that our morphological classification is unaffected by inclination effects. As a final remark, we note that the  $n$  Sérsic indices of intermediate-type disks also show a residual (but marginal) dependence on ellipticity: this is of course the morphological class for which the likely similar light contribution of bulge and disk components along the line-of-sight is the most difficult to disentangle. Nevertheless, the  $n$  values spanned by these morphological class at the different ellipticities are consistently in the “intermediate” range of  $n \sim 2 - 2.8$  (see table 2),

providing a consistent characterization of these systems across the whole ellipticity range.

#### 8. THE CONCENTRATION OF SATELLITE GALAXIES OF DIFFERENT HUBBLE TYPES IN DIFFERENT ENVIRONMENTS

As discussed in the introduction, the main goal of ZENS is to study galaxy properties, at fixed stellar mass and Hubble type, as a function of several environmental parameters derived self-consistently for the same galaxy sample, i.e., the host halo mass, the large scale density  $\log(1 + \delta_{LSS})$  and the projected group-centric distance. We furthermore split the ZENS galaxy sample in central galaxies in their host group halos, and satellite galaxies, which orbit the central galaxies within those halos (see Paper I for the precise definition of central and satellite galaxies, and for the environmental parameters). Several ZENS analyses are underway, which use the ZENS database, including the structural and morphological information derived in this paper, to investigate how galaxy structural and morphological properties vary across the different environmental regimes.

In this second paper in the ZENS series, as a first exploitation of the structural measurements presented above, we focus on how the concentration of *satellite galaxies* depends, at fixed stellar mass, on (i) *Hubble type*, and on (ii) *the other three environments*, in addition to the *satellite vs. central* ranking, that we explore in ZENS, i.e., *group mass*, *group-centric distance* and *large-scale structure density*.



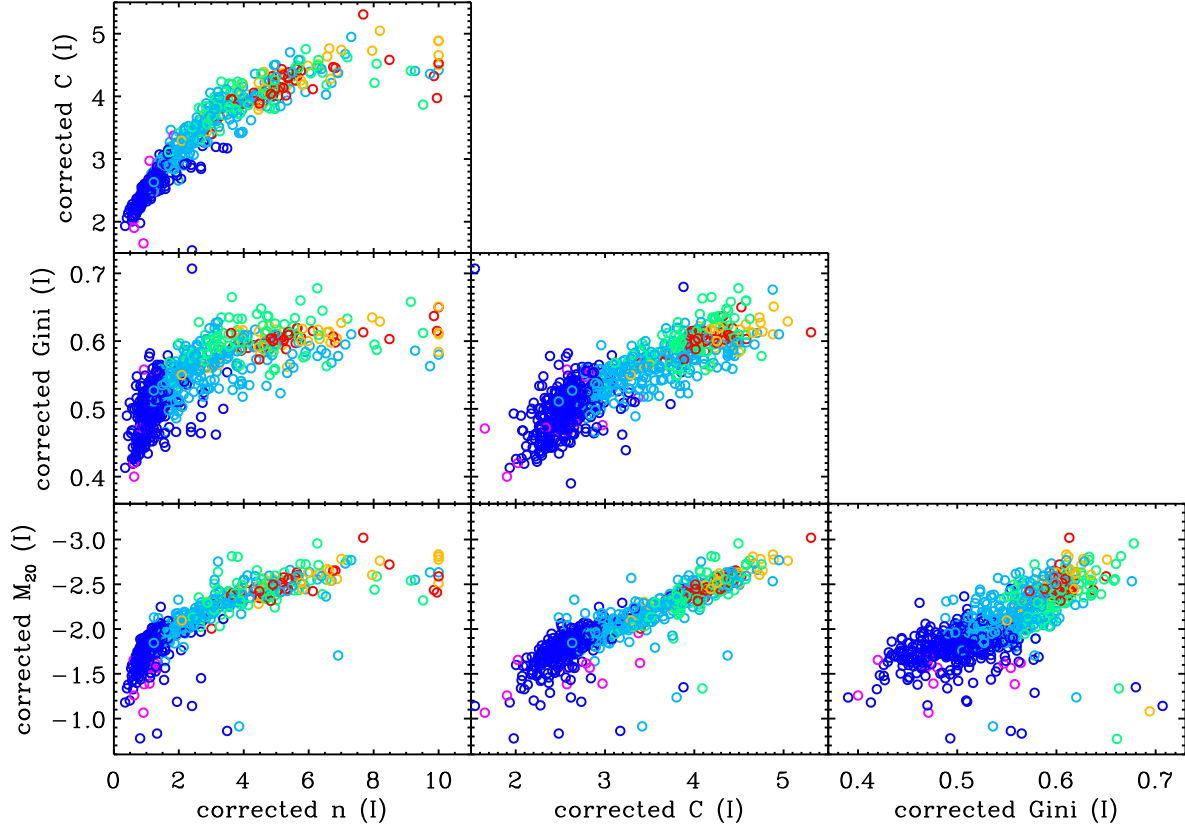


**Figure 18.** Location of the different morphological classes in the  $C - Gini - M_{20} - n$  planes. The colors highlight the five morphological classes: red=ellipticals, orange=S0, green=bulge-dominated spirals, cyan=intermediate-type disks, blue=late-type disks and magenta=irregulars.

### 8.1. The role of Hubble type at fixed stellar mass

It is known that galaxy structure, as described by the concentration parameter, is a strong function of galaxy mass (e.g. Kauffmann et al. 2003; van der Wel 2008). As we have discussed above, concentration is however a relatively poor indicator of galaxy morphology (when this is defined according to a more physical parameter such as the bulge-to-total ratio, as we do for the ZENS galaxies). Furthermore, morphology also is a function of stellar mass (see Paper III and also, e.g., Pannella et al. 2006; Bamford et al. 2009; Oesch et al. 2010; Bernardi et al. 2010; Vulcani et al. 2011). With available robust (corrected) concentration values, and a B/T-based morphological classification, we thus investigate how much of the concentration vs. galaxy stellar mass correlation is to be ascribed to a variation in the Hubble type of galaxies, and how much is actually driven by a real change in concentration within each individual morphological types. Stellar masses are taken from Paper III. The results of this analysis will also help us interpret the analysis of satellites’ concentration in the different environmental parameters, for which, in order to gain statistics, we will join together galaxies of different morphological classes.

Figure 21 shows the corrected concentration as a function of galaxy stellar mass. The points connected with lines are the median concentrations for satellite galaxies, divided according to the morphological types (note

that S0 and bulge-dominated spiral galaxies are joined together into a single broad morphological bin of “bulge-dominated” galaxies). The medians were calculated using a running box above the mass completeness of each morphological type (the results are noisier but consistent when using independent mass bins). The inspection of this figure shows an increase in concentration with increasing galaxy stellar mass at fixed morphological type for disk galaxies. Specifically, our elliptical satellites’ sample covers a small range of stellar mass ( $\sim 10^{10-10.5} M_{\odot}$ ), over which the concentration is observed to remain constant. For all types of disk galaxies, however, where the range of masses covered is larger, a trend of concentration with stellar mass is clearly observable, separately for each morphological disk type (the latter defined according to the galaxy bulge-to-total ratios as described in Section 7). We note that residual bulge-to-disk variations with stellar mass *within* each morphological disk class are possible, since our morphological classification was done independent of galaxy stellar mass, and each morphological bin covers a relatively broad range of bulge-to-total ratio. Quantitatively, however, the median bulge-to-total ratios vary, between the mass bin centered at  $10^{10} M_{\odot}$  and the mass bin centered at  $10^{10.7} M_{\odot}$ , only from 56% to 62%, 34% to 35%, and 6% to 17%, respectively for bulge-dominated, intermediate-type and late-type disk galaxies. Thus, we conclude that the known concentration-mass correlation is not solely driven by a correlation between morphological type and

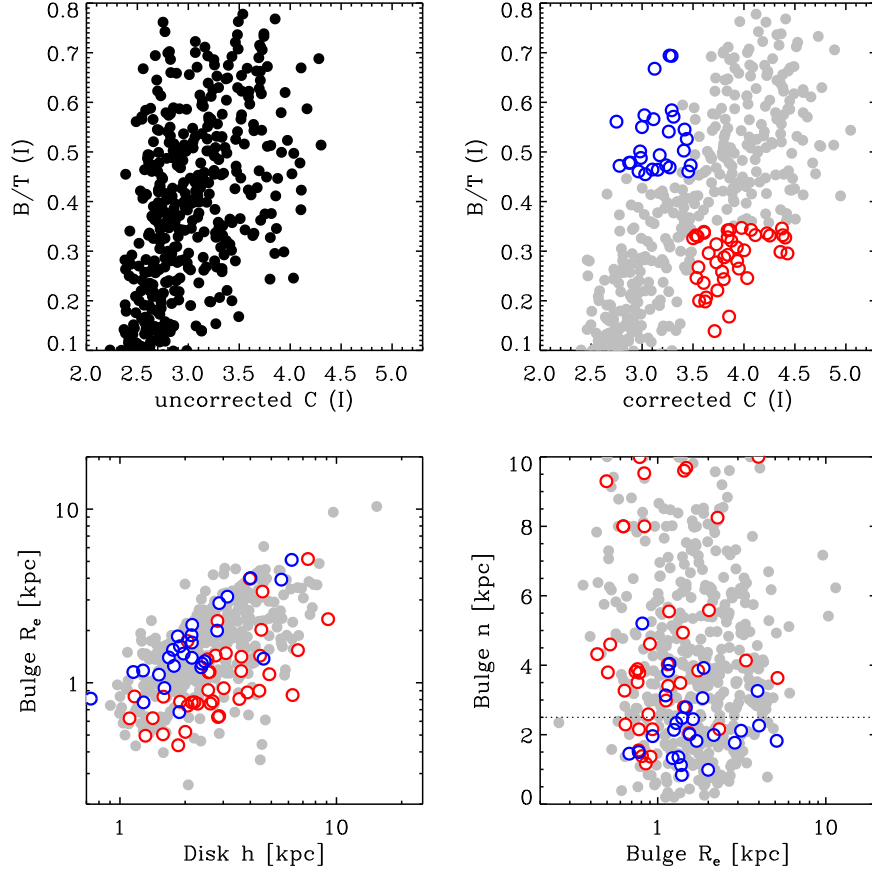


**Figure 19.** The  $I$ -band relation between bulge-to-total ratio and uncorrected (top left panel) and corrected (top right panel) concentration for the first-epoch ZENS disk galaxies with bulge-to-disks analytical fits. In the plot with corrected- $C$  values, in red are highlighted galaxies which are concentrated ( $C > 3.5$ ) but have a low bulge-to-total ratio ( $B/T < 0.35$ ). In blue are highlighted galaxies which have low concentration ( $C < 3.5$ ) and high  $B/T > 0.45$ . Note the large scatter in the corrected- $C$  vs.  $B/T$  relationship, which makes  $C$  a poor morphological indicator. Note also that uncorrected- $C$  values are, as expected, even worse representatives of the galaxy  $B/T$  (and thus physical morphology) properties. The two bottom panels show, from left to right, the  $I$ -band bulge half-light radius vs. disk scalelength plane, and the  $I$ -band bulge Sérsic index vs. bulge half-light radius plane. The colors in these plots represent the galaxy populations highlighted in the  $B/T$  vs. corrected- $C$  plane.

stellar mass, but is, at least partially, driven also by a genuine increase in concentration of galaxies of similar Hubble type, i.e., of similar bulge-to-total ratio.

We fit the observed trends of corrected concentration versus galaxy stellar mass with a linear relation,  $C = \alpha + \beta \log(M/M_\odot)$ , in the mass range which is probed by all morphological type, i.e., for those bins which are above  $10^{10} M_\odot$  for their full width. The global  $C - M$  relation for the late-type disks shows a break around  $\sim 10^{10} M_\odot$ , below which mass the relation flattens; a linear fit is however a good approximation at  $M > 10^{10} M_\odot$  where we can make a meaningful comparison with the other types. The slopes  $\beta$  for the four morphological classes above this threshold mass are, respectively,  $\beta_{bulge-dom} = 0.49 \pm 0.07$ ,  $\beta_{interm.-type} = 0.30 \pm 0.13$  and  $\beta_{late-type} = 0.63 \pm 0.09$ ; satellite elliptical galaxies are consistent with no dependence of concentration on the galaxy mass, i.e.  $\beta_{ellipticals} = 0$ . Although, as commented above, the lack of dependence of  $C$  on stellar mass for the ellipticals is established only across a relatively limited mass range, generally speaking this finding follows the global trend, established on the disk galaxies, of a flattening of the  $C$  vs. galaxy stellar mass relation from the later- to the

earlier morphological type.

## 8.2. The dependence of disk satellite concentration on LSS density, group-centric distance and group halo mass

The sample of elliptical satellites in our first-epoch ZENS sample is limited, and does not enable us to further investigate their dependence on any of the ZENS environmental parameters. We can however address the question of whether the concentration of early-/late-type disk satellite galaxies depends on environment – and precisely on which of the three environments studied in ZENS.

In Figure 22 we present the (corrected) concentration vs. galaxy stellar mass relation for satellite disk galaxies, split into two broad morphological bins of “bulge-dominated” galaxies and “disk-dominated” galaxies by adding together S0s and bulge-dominated spirals in one bin, and intermediate-type and late-type disks in the other bin. The relation is plotted separately as function of group mass  $M_{GROUP}$ , LSS (over)density  $\delta_{LSS}$ , and group-centric distance  $R_{R200}$  (from top to bottom). The broad bulge-dominated galaxies bin is split in four bins of galaxy stellar mass, i.e.,  $\log(M/M_\odot) \in [9.5, 9.78]$ ,



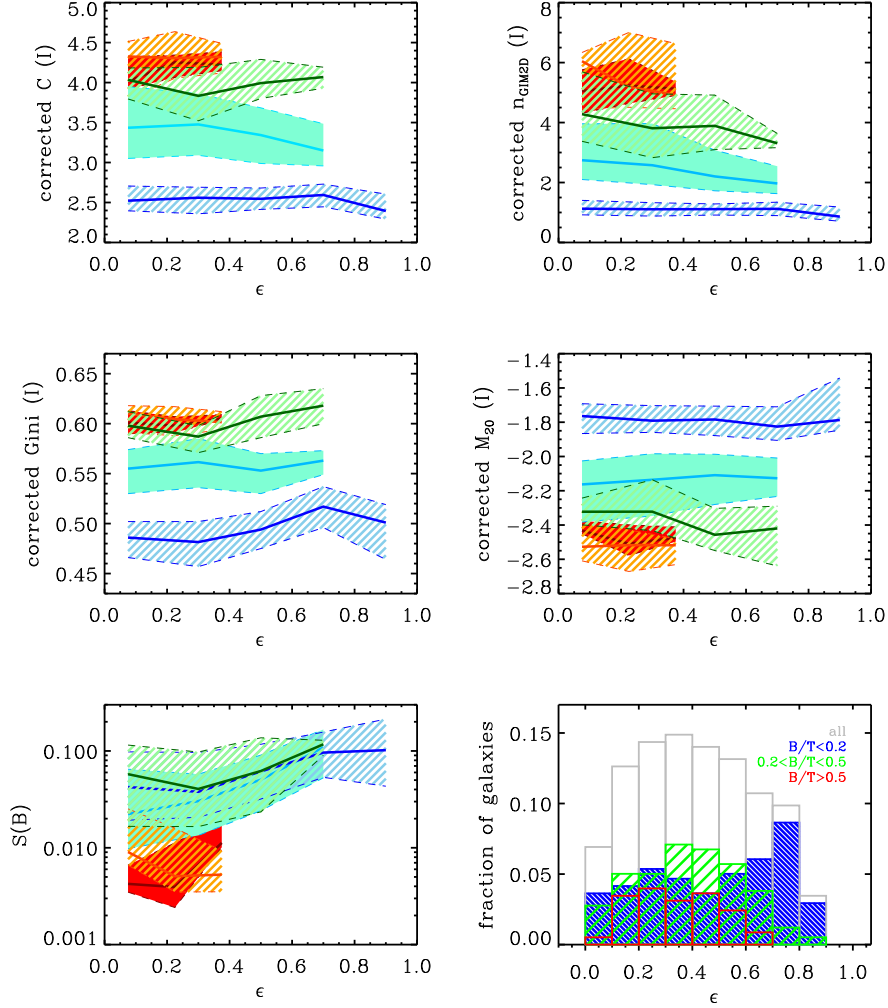


**Figure 20.** The shaded areas show the distribution of structural parameters (concentration, Sérsic index, Gini coefficient,  $M_{20}$  index and smoothness), as a function of measured ellipticity  $\epsilon$ , for galaxies of different morphological types. The color scheme reflects the morphological class: red=elliptical galaxies, orange=S0, green=bulge-dominated spirals, cyan=intermediate-type disks and blue=late-type disks. The distributions are calculated in bins of 0.15 in ellipticity for ellipticals and S0 – which span a smaller range of ellipticity – and in bins of 0.2 for all the other morphological types. The thick solid lines mark the median values and the shaded areas the 25th and 75th percentiles. Note the good segregation in parameter space achieved by different morphological classes based on a B/T criterion; this is the result of our correction scheme, which eliminates observational biases (especially PSF-induced biases) from the measurements of the non-parametric estimators of galaxy structure. The bottom right panel presents the distribution of ellipticities for galaxies with  $I$ -band  $B/T < 0.2$  (blue histogram),  $0.2 < B/T < 0.5$  (green histogram) and  $0.5 < B/T < 0.8$  (red histogram) normalized to the total number of galaxies with available  $I$ -band B+D decompositions, for which the global distribution is shown in gray. We argue in the text that our B/T measurements are unaffected by inclination effects.

[9.78,10.08[, [10.08,10.38[, [10.38,10.88]; we use two bins of galaxy stellar mass for the broad bulge-dominated galaxies bin, i.e.,  $\log(M/M_{\odot}) \in [10.,10.6[$ ,  $> 10.6$ .

Before discussing the results we present some considerations on the biases and uncertainties which may affect the analysis. First, we remind that trends with group mass that we measure are, intrinsically, possibly even stronger. As discussed in Paper I, the uncertainty on our group mass estimates tends to “wash out” trends with this environmental quantity; quantitatively, real trends with group mass have slopes  $\approx 1.3 - 1.4$  steeper on average than what we can measure in the ZENS sample.

In Paper I we furthermore discuss a classification of the ZENS groups into “relaxed” and “unrelaxed” groups, according to whether a self-consistent solution for a central

galaxy can be found (in relaxed groups) or not (in unrelaxed groups). The latter are expected to be combination of genuinely dynamically young, merging structures, contaminated by physically relaxed groups for which several observational biases prevent us to properly identify their central galaxy. In the spirit of checking that our results are not affected by the inclusion of the unrelaxed groups in our studies, in Figure 22 we show the results for all first-epoch ZENS groups (left panels) and for the subset of first-epoch relaxed groups only (right panels) when studying the dependence of the  $C$ -mass relation on either  $M_{GROUP}$  or  $R_{R200}$ .

In Paper I we also comment on the fact that, at group masses above  $\sim 10^{13.4} M_{\odot}$ , group mass  $M_{GROUP}$  and LSS (over)density  $\delta_{LSS}$  are correlated by nature,

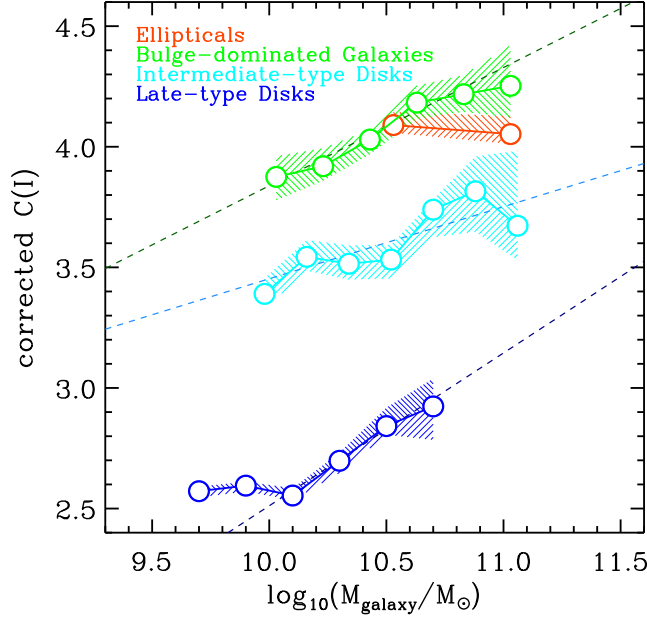


**Figure 21.** Corrected concentration  $C$  versus galaxy stellar mass (from Paper III), for the different Hubble types defined in Section 7 (S0 and bulge-dominated spirals are joined together in the broad bulge-dominated galaxies class). The points connected with lines show the median galaxy concentration, calculated over a running box of width 0.3 dex in mass for intermediate-type and late-type disks, and of width 0.4 dex for the earlier types. The dashed lines are the best linear fits to the observed relations over the mass range probed by all morphological types, i.e., for masses above  $10^{10} M_{\odot}$ . The shaded areas correspond to the  $1\sigma$  error bars on the median values.

since massive groups are found by definition only in dense regions of the LSS. In contrast, groups of masses  $< 10^{13.4} M_{\odot}$  are found at any value of  $\delta_{LSS}$ . It is thus possible to disentangle the effects of  $M_{GROUP}$  and  $\delta_{LSS}$  by limiting the studies as a function of  $\delta_{LSS}$  to group masses below this threshold. We adopt this strategy here as well, and, in order to search for a dependence of the  $C$ -mass relation for satellites on  $\delta_{LSS}$ , we test that the results obtained when including all first-epoch groups in the analysis with  $\delta_{LSS}$  (left central panel) hold also when restricting the group sample to groups with  $M_{GROUP} < 10^{13.4} M_{\odot}$  (right central panel).

Having established that the concentration parameter is a function of both galaxy stellar mass and morphological type (see Figure 21), keeping dependencies of both factors with the environment under control is necessary to proceed in this analysis. In Paper III we discuss the variation of the stellar mass of each broad morphological type with our environmental indicators and show that in our sample galaxy mass is largely independent of environment at fixed morphological type; we furthermore refer to Lu et al. (2012) (Paper IV) for a detailed study of the variation of the morphological mix with environment.

Here we note that, for the broad disk-dominated galaxies bin, biases in the median mass with any of the environments are not an issue, as for this class we can afford a fine galaxy mass bin splitting, and compare the  $C$ -mass relation for different environments within relatively small galaxy mass bins. For the broad bulge-dominated galaxies bin, however, given the fairly broad ranges covered by each of the two galaxy stellar mass bins, a difference in the median galaxy stellar mass (and, more generally, of the galaxy stellar mass distributions) between some of

the different environments could in principle be present. This could induce a spurious dependence on such environments of the  $C$  vs. stellar mass relations plotted in Figure 22. To keep this potential bias under control, we computed the median galaxy stellar masses within each environmental bin, and found that, for all three environments under study, the median stellar mass of galaxies in the broad bulge-dominated galaxies morphological bin changes by less than 0.03 dex between the environmental bins under comparison (i.e., low/high  $M_{GROUP}$ ,  $\delta_{LSS}$  and inner/outer group regions).

We also verified that the morphological mix does not change substantially with environment. The fractional contribution of intermediate-type disk galaxies to the total intermediate- plus late-type disk populations which compose the broad disk-dominated galaxies morphological bin defined above varies at most by 6% between the low/high  $M_{GROUP}$  samples. Precisely, in the four bins of galaxy stellar mass defined for the broad disk-dominated galaxies morphological bin this fractional contribution, i.e.,  $\frac{N_{interm.}}{N_{interm.} + N_{late-type}}$ , equals, respectively, 34%, 46%, 56%, 83% for  $M_{GROUP} < 10^{13.4} M_{\odot}$  and 36%, 41%, 62%, 85% for  $M_{GROUP} > 10^{13.4} M_{\odot}$ . Likewise, the fractional contribution of S0s to the broad bulge-dominated galaxies morphological bin is also almost identical between the samples of  $M_{GROUP} < 10^{13.4} M_{\odot}$  and  $M_{GROUP} > 10^{13.4} M_{\odot}$ , and equal to  $\sim 15\%$  at  $M_{galaxy} \sim 10^{10} M_{\odot}$  and  $\sim 40 - 45\%$  at  $M_{galaxy} > 10^{10.5} M_{\odot}$ . On the other hand, variations up to  $\sim 30 - 40\%$  are detected in the contributions of S0s and bulge-dominated spirals to the broad bulge-dominated morphological bin between samples at small/large group-centric distances and high/low LSS (over)densities; hence we use caution in interpreting,

for this broad morphological type, possible differences in the  $C$  vs. galaxy stellar mass relation in these environments.

Most environmental comparisons in Figure 22 show no clear trends with the different environments of the concentration vs. stellar mass relation for satellite galaxies, in either of the two broad morphological classes of early- and disk-dominated galaxies. Two potential environmental effects are however noticed, at a marginal statistical significance in our data, which are worth highlighting for further investigations on larger datasets:

(1.) At fixed galaxy stellar mass above  $10^{10.5} M_{\odot}$ , satellites with a bulge-dominated morphology are 5% more concentrated in the outskirts of galaxy groups ( $R/R_{200} > 0.6$ ) than similar satellites at smaller group-centric distances<sup>9</sup>. As discussed above, the interpretation of what gives origin to this effect is complicated by a different morphological mix, in these two environments, of S0 and bulge-dominated spirals within the broad bulge-dominated galaxies bin. Specifically, in our sample, and within the caveats of a relatively modest number of galaxies ( $\sim 30$ ), the S0 contribution to the broad bulge-dominated bin varies from  $\sim 25\%$  to  $\sim 60\%$  from the inner to the outer regions of the groups.

(2.) The disk-dominated population shows a systematic increase in median concentration, at fixed galaxy stellar mass above  $10^{10} M_{\odot}$ , with increasing group halo mass. In this case, the similar contributions of intermediate-type disks and late-type disks to the broad disk-dominated morphological bin ensure that this is a genuine environmental effect. The difference in concentration between low and high mass groups is  $\Delta C \simeq 0.3$  at  $\sim 10^{10.5} M_{\odot}$ , and increases to  $\sim 0.4$  in the highest mass bin. The effect is robust towards the inclusion/exclusion of the sample of unrelaxed groups.

## 9. SUMMARY AND CONCLUDING REMARKS

We have presented detailed structural analyses performed on the 769 galaxies in the 79 groups of the first-epoch ZENS data introduced in Paper I. The parametric and non-parametric structural measurements presented here, together with the detailed environmental parameters from Paper I and the photometric (including stellar masses) measurements presented in Paper III, set the basis for a number of forthcoming publications which use the first-epoch ZENS data to explore which environmental scales are relevant for the evolution of morphologically different galaxy populations at different mass scales (Carollo et al. 2012b; Cibinel et al. 2012b; Lu et al. 2012; Pipino et al. 2012; Rudick et al. 2012a,b). The measurements are included in the global ZENS catalog that we published in Paper I. In detail, the measurements that we have derived are:

- Strength of bars in disks, quantified through an isophotal analysis (Section 3);
- Single- and double-component (bulge+disk) Sérsic fits parameters both in the  $B$  and  $I$  bands, including model-based galaxy sizes (Sections 4.1 and 4.2);

- Non-parametric structural indices of concentration, asymmetry, smoothness of the light distribution, and Gini and  $M_{20}$  coefficients, and “aperture photometric” size estimates (Section 5);
- Morphological classes, based on a quantitative bulge+disk criterion, augmented (or supported) by quantitative criteria regarding the non-parametric diagnostics, *corrected* for observational biases (Sections 4.2 and 7).

Crucially, we do indeed derive correction matrices, which we apply to the relevant structural estimates, to minimize biases which, depending on PSF size as well as galaxy magnitude, size, shape of light profile and ellipticity, would otherwise prevent a reliable comparison of the structural properties of galaxies observed in different seeing conditions, and lying in different regions of this four-dimensional galaxy parameter space (see Section 6).

As expected, biases in the model-fit parameters are substantially reduced thanks to the treatment of the PSF-blurring effects in these algorithms; still, some are present even in the model-fit parameters, which may have an impact in some analyses if left uncorrected. Disk properties are well measured and require very modes or no further corrections; so are bulge-to-total ratios, which therefore offer an excellent parameter to base a quantitative morphological/structural classification. In contrast, bulge  $n$  Sérsic indices and half-light radii are degenerate in some circumstances. This implies that, on global galactic scales, concentration parameter or  $n$ -Sérsic index, alone, are not a good proxy for bulge-to-disk ratio and thus morphology: bulges can give large contributions to the total light budget and have large half-light radii, leading to low galaxy concentrations, or, vice-versa, bulges can be very compact and lead to high galaxy concentrations despite a modest contribution to the total light. Finally, we particularly warn against using uncorrected non-parametric estimators as galaxy classifiers since, understandably, they suffer from severe observational biases and introduce severe errors in the classifications (see Section 6).

As a first application of our corrected structural measurements, we study the variation of concentration in *satellite* galaxies of fixed stellar mass (from Paper III) with morphological type, and with the three environments detailed in Paper I, i.e., the mass of the host group halo, the projected group-centric distance, and the density of the large-scale structure cosmic web (Section 8).

We find that the known correlation of satellite concentration with galaxy stellar mass (e.g. Kauffmann et al. 2003) holds at a fixed morphological type. Specifically, there is a genuine increase in concentration with increasing stellar mass for disk satellite galaxies within each separate bin of bulge-dominated galaxies, intermediate-type and late-type disk morphologies. The slope of the concentration vs. galaxy stellar mass relationship flattens from the later to the earlier types (and becomes  $\sim 0$  for satellites with an elliptical morphology, which however cover a limited range in galaxy stellar mass in our sample). It is not trivial to disentangle, in a physically meaningful way, the contributions of an increasing bulge-to-total ratio with increasing mass, and an increasing bulge concentration at fixed bulge-to-total ratio with increas-

<sup>9</sup> A similar effect, seen at smaller masses in the total first-epoch ZENS sample (left), disappears when using only the relaxed groups; we thus do not discuss these lower masses further)

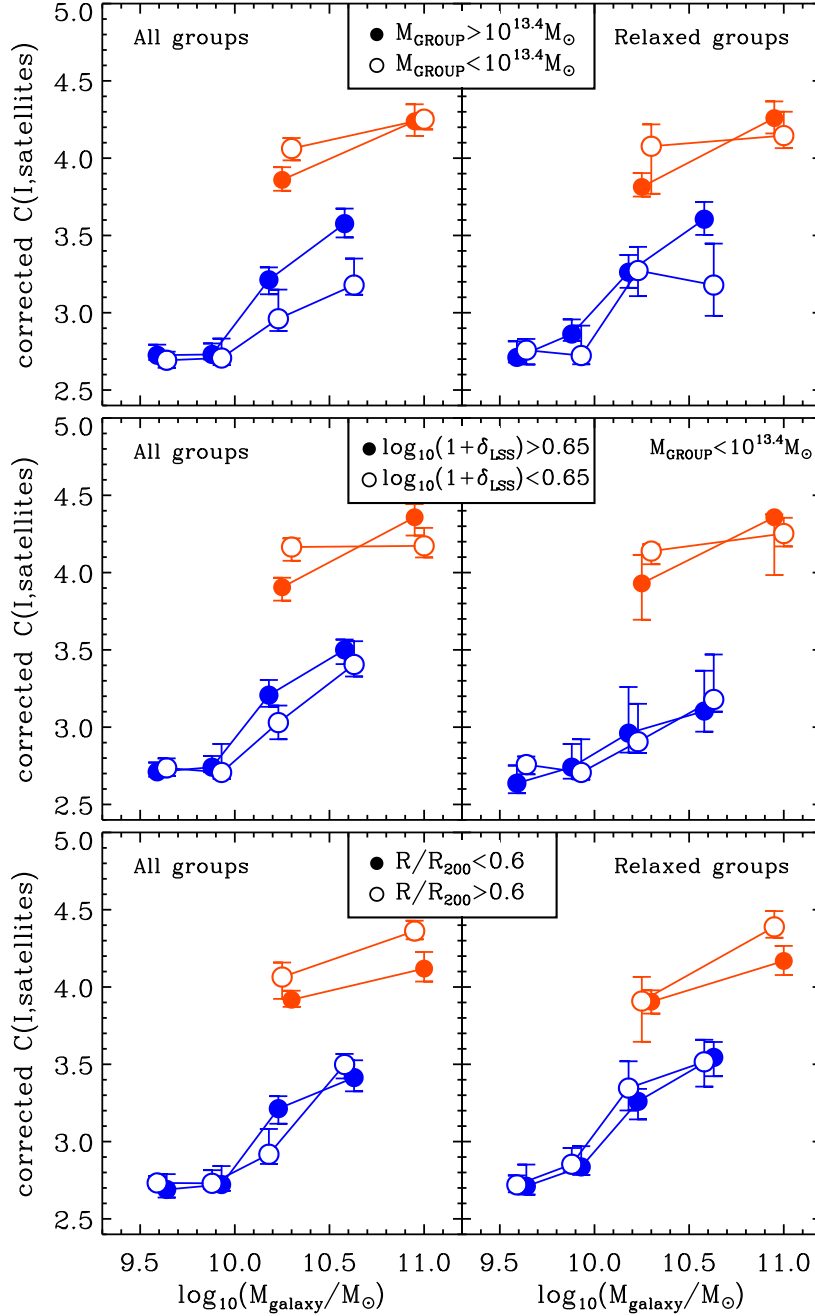


**Figure 22.** The panels show the corrected concentration parameter  $C$  as a function of galaxy stellar mass, split in bins of environments as follows: top panels show the dependence on group mass  $M_{\text{GROUP}}$ ; central panels on LSS (over)density  $\delta_{\text{LSS}}$ ; bottom panels on group-centric distance ( $R/R_{200}$ ). Only disk satellites are shown in this analysis. These are split in two broad bins of morphologies, specifically bulge-dominated galaxies (which include bulge-dominated spirals and S0 galaxies; red) and disk-dominated galaxies (which include intermediate-type and late-type disks; blue). For all three environmental indicators, filled symbols show results for the “denser” bin, and empty symbols for the “lighter” bin. In the top and bottom panels, left plots are for all first-epoch groups, and right plots for relaxed groups only (see text). In the central panels, the left plot shows again results for all first epoch groups, but this time the right plot shows results for groups with  $M < 10^{13.4} M_{\odot}$  only, to avoid spurious effects with group mass when studying the effects of the LSS density field. Symbols are positioned at the center of any given mass bins, with a small offset between denser/lighter environments applied for visual clarity.

ing mass, to the increase in concentration of satellite disk galaxies with increasing stellar mass. This is true even in our study, in which we did indeed base our morphological classification on the bulge-to-total ratio, and thus bulge-to-total variations within each Hubble type should be minimized. There are nevertheless some residual effects, as the median  $B/T$  is found to vary in our sample from  $\sim 5\%$  at  $10^{10} M_{\odot}$  to  $\sim 15\%$  at  $\sim 10^{10.5} M_{\odot}$  for late-type disks, and from  $55\%$  to  $70\%$  within the same galaxy stellar mass range for bulge-dominated disks. Still, for intermediate-type disk satellites, in which the bulge-to-total ratio is tightly constrained by firm lower and upper boundaries by definition, the increase in satellite density with stellar mass can be genuinely ascribed to a  $\sim 30\%$  decrease in the bulge-to-disk *size* ratio, i.e., to a genuine increase in the concentration of the bulge component at fixed bulge-to-total *light* ratio. We tentatively assume this as the explanation for the increase of disk satellite concentration with stellar mass at fixed Hubble type, an hypothesis which we will test with further analyses on our data and on simulated data.

We furthermore see no dependence of satellites' concentration on LSS density, consistently with previous works (e.g. van der Wel 2008). This remains true for either disk-dominated galaxies (a broad morphological bin including galaxies that our classification scheme identifies as intermediate-type and late-type disks) or bulge-dominated (an equivalently broad morphological bin which includes bulge-dominated disks and S0 galaxies).

We find however two effects respectively with group-centric distances for  $10^{10.5} M_{\odot}$  disk satellites with a prominent bulge component (our broad "bulge-dominated" morphological bin), and with group mass for  $10^{10} M_{\odot}$  disk satellites with small or no bulge component (our broad "disk-dominated" morphological bin). Albeit they both have a modest statistical significance in our first-epoch ZENS sample, we highlight them for further investigations on larger databases (with similar morphological/structural quality of our sample).

First, bulge-dominated satellites of stellar masses  $> 10^{10.5} M_{\odot}$  appear to be more concentrated at larger than at smaller group-centric distance. The interpretation of this result as a hint for an environmental effect is however hampered by the higher relative contribution to the bulge-dominated morphological bin of S0s relative to bulge-dominated spiral galaxies, in the outskirts relative to the cores of groups. This is interesting but counter to the intuitive idea that gas-rich bulge-dominated spirals may become S0 galaxies as they fall deeper into their group potential wells. This finding would favor however a picture where (i) the transformation of S0s occurs as soon as disk galaxies enter the group potential, and (ii) further stellar evolution within the groups replenished the dried-out disks of S0 galaxies of fresh gas, establishing/restoring in them a bulge-dominated morphology. We will endeavor to test this working hypothesis on a larger database (with the required structural and morphological quality as achieved for our ZENS sample).

Second, and this time an environmental effect which should suffer from no morphological complications,  $M > 10^{10} M_{\odot}$  disk-dominated galaxies appear to have a higher concentration in high-mass  $M > 10^{13.4} M_{\odot}$  groups than

in lower-mass groups. We discuss this result further in a forthcoming ZENS analysis, where we present the galaxy radius and surface mass density versus galaxy stellar mass relations for ZENS satellites of different morphologies (Carollo et al. 2012b).

Finally, in this paper, which has focused on the first-epoch ZENS data, the number of central galaxies is too small to discuss possible differences in concentration between centrals versus satellites (with Hubble type and the various environments). Weinmann et al. (2009); Guo et al. (2009) found evidence in SDSS that, among galaxies with  $C < 3$ , satellites are more concentrated than centrals with identical stellar mass. These authors interpret the variation in concentration within the framework of gradual stripping and subsequent quenching of satellite galaxies during infall into the group potential. This is also believed to cause a reddening of the satellite galaxies and a shrinking of their typical sizes. Here we wish to note that the SDSS studies divide the early- and late-type morphological classes on the basis of a non-corrected concentration criterion ( $C < 3$  for late-type and  $C > 3$  for early-type galaxies). Comparing their Figure 1 with our Figure 19, we see that  $C < 3$  in the SDSS system roughly corresponds to a value of  $C = 3.5 - 4$  in ZENS, as our concentrations show a small offset due to the corrections we applied. As illustrated in Figure 21, a cut at constant concentration sub-divides the ZENS galaxy sample into two broad bins in which, however, individual Hubble types are mixed together below the chosen  $C$  threshold. It thus remains an open question whether the difference in concentration between centrals and satellites reported by those authors is the result of a variation in the morphological mix of the central vs. satellite populations, or rather a change in the structure of central and satellite galaxies at a fixed morphological type. We postpone this analysis to a forthcoming paper, which will benefit from the increased statistics gained by using the entire ZENS sample.

#### ACKNOWLEDGEMENTS

A.C., E.C., T.L. and C.R. acknowledge support from the Swiss National Science Foundation. This publication makes use of data from ESO Large Program 177.A-0680, and data products from the Two Micron All Sky Survey, which is a joint project of the University of Massachusetts and the Infrared Processing and Analysis Center/California Institute of Technology, funded by the National Aeronautics and Space Administration and the National Science Foundation. GALEX (*Galaxy Evolution Explorer*) is a NASA Small Explorer, launched in April 2003. We gratefully acknowledge NASA's support for construction, operation, and science analysis for the GALEX mission.

#### REFERENCES

- Abraham, R. G., Tanvir, N. R., Santiago, B. X., et al. 1996, MNRAS, 279, L47
- Abraham, R. G., Merrifield, M. R., Ellis, R. S., Tanvir, N. R., & Brinchmann, J. 1999, MNRAS, 308, 569
- Abraham, R. G., & Merrifield, M. R. 2000, AJ, 120, 2835
- Abraham, R. G., van den Bergh, S., & Nair, P. 2003, ApJ, 588, 218
- Aguerri, J. A. L., Méndez-Abreu, J., & Corsini, E. M. 2009, A&A, 495, 491

- Allen, P. D., Driver, S. P., Graham, A. W., et al. 2006, MNRAS, 371, 2
- Bailin, J., & Harris, W. E. 2008, ApJ, 681, 225
- Baldry, I. K., Balogh, M. L., Bower, R. G., et al. 2006, MNRAS, 373, 469
- Balogh, M. L., Morris, S. L., Yee, H. K. C., Carlberg, R. G., & Ellingson, E. 1997, ApJ, 488, L75
- Bamford, S. P., Nichol, R. C., Baldry, I. K., et al. 2009, MNRAS, 393, 1324
- Barazza, F. D., Jogee, S., & Marinova, I. 2008, ApJ, 675, 1194
- Barden, M., et al. 2005, ApJ, 635, 959
- Barnes, J. E. 1988, ApJ, 331, 699
- Beckman, J. E., Peletier, R. F., Knapen, J. H., Corradi, R. L. M., & Gentet, L. J. 1996, ApJ, 467, 175
- Bender, R., Doebereiner, S., & Moellenhoff, C. 1988, A&AS, 74, 385
- Benítez, N., Ford, H., Bouwens, R., et al. 2004, ApJS, 150, 1
- Bernardi, M., Shankar, F., Hyde, J. B., et al. 2010, MNRAS, 404, 2087
- Bernstein, R. A., Freedman, W. L., & Madore, B. F. 2002a, ApJ, 571, 56
- Bernstein, R. A., Freedman, W. L., & Madore, B. F. 2002b, ApJ, 571, 107
- Bertin, E., & Arnouts, S. 1996, A&AS, 117, 393
- Blanton, M. R., et al. 2005, AJ, 129, 2562
- Blanton, M. R., Hogg, D. W., Bahcall, N. A., et al. 2003, ApJ, 594, 186
- Blanton, M. R., & Berlind, A. A. 2007, ApJ, 664, 791
- Buta, R., Vasylyev, S., Salo, H., & Laurikainen, E. 2005, AJ, 130, 506
- Byun, Y. I., Freeman, K. C., & Kylafis, N. D. 1994, ApJ, 432, 114
- Cameron, E., & Driver, S. P. 2007, MNRAS, 377, 523
- Cameron, E., & Driver, S. P. 2009, A&A, 493, 489
- Cameron, E., Carollo, C. M., Oesch, P., et al. 2010, MNRAS, 409, 346
- Carollo, C. M., Franx, M., Illingworth, G. D., & Forbes, D. A. 1997a, ApJ, 481, 710
- Carollo, C. M., Danziger, I. J., Rich, R. M., & Chen, X. 1997b, ApJ, 491, 545
- Carollo, C. M., Stiavelli, M., de Zeeuw, P. T., & Mack, J. 1997c, AJ, 114, 2366
- Carollo, C. M., Stiavelli, M., & Mack, J. 1998, AJ, 116, 68
- Carollo, C. M. 1999, ApJ, 523, 566
- Carollo, C. M., Stiavelli, M., de Zeeuw, P. T., Seigar, M., & Dejonghe, H. 2001, ApJ, 546, 216
- Carollo, C. M., Scarlata, C., Stiavelli, M., Wyse, R. F. G., & Mayer, L. 2007, ApJ, 658, 960
- Carollo, C. M., Cibinel, A., Lilly, S. J., et al. 2012 (Paper I), ApJ, submitted
- Carollo, C. M. et al. 2012b, in prep. (Paper IX)
- Cibinel, A., Carollo, C. M., Lilly, S. J., et al. 2012a (Paper III), ApJ, submitted
- Cibinel, A., Carollo, C. M. et al. 2012b, in prep. (Paper VIII)
- Colless, M., Dalton, G., Maddox, S., et al. 2001, MNRAS, 328, 1039
- Colless, M., Peterson, B. A., Jackson, C., et al. 2003, arXiv:astro-ph/0306581
- Combes, F., Debbasch, F., Friedli, D., & Pfenniger, D. 1990, A&A, 233, 82
- Conselice, C. J. 2003, ApJS, 147, 1
- Cooper, M. C., Newman, J. A., Madgwick, D. S., Gerke, B. F., Yan, R., & Davis, M. 2005, ApJ, 634, 833
- Côté, P., Ferrarese, L., Jordán, A., et al. 2007, ApJ, 671, 1456
- Courteau, S., de Jong, R. S., & Broeils, A. H. 1996, ApJ, 457, L73
- Cunow, B. 2001, MNRAS, 323, 130
- Debatista, V. P., Carollo, C. M., Mayer, L., & Moore, B. 2004, ApJ, 604, L93
- Debatista, V. P., Mayer, L., Carollo, C. M., et al. 2006, ApJ, 645, 209
- Dekel, A., Birnboim, Y., Engel, G., et al. 2009a, Nature, 457, 451
- Dekel, A., Sari, R., & Ceverino, D. 2009b, ApJ, 703, 785
- de Jong, R. S. 1996, A&AS, 118, 557
- de Propris, R., et al. 2003, MNRAS, 342, 725
- de Souza, R. E., Gadotti, D. A., & dos Anjos, S. 2004, ApJS, 153, 411
- de Vaucouleurs, G. 1963, ApJS, 8, 31
- Disney, M. J. 1976, Nature, 263, 573
- Dressler, A. 1980, ApJ, 236, 351
- Driver, S. P., Popescu, C. C., Tuffs, R. J., Liske, J., Graham, A. W., Allen, P. D., & de Propris, R. 2007, MNRAS, 379, 1022
- Eke, V. R., Baugh, C. M., Cole, S., et al. 2004a, MNRAS, 348, 866
- Eke, V. R., Frenk, C. S., Baugh, C. M., et al. 2004b, MNRAS, 355, 769
- Einasto, M., et al. 2007, A&A, 464, 815
- Erwin, P. 2005, MNRAS, 364, 283
- Fall, S. M., & Efstathiou, G. 1980, MNRAS, 193, 189
- Feldmann, R., Mayer, L., & Carollo, C. M. 2008, ApJ, 684, 1062
- Ferrarese, L., van den Bosch, F. C., Ford, H. C., Jaffe, W., & O'Connell, R. W. 1994, AJ, 108, 1598
- Fisher, D. B., & Drory, N. 2008, AJ, 136, 773
- Forbes, D. A., & Thomson, R. C. 1992, MNRAS, 254, 723
- Franx, M., Illingworth, G., & Heckman, T. 1989, AJ, 98, 538
- Gadotti, D. A. 2008, MNRAS, 384, 420
- Graham, A. W. 2001, AJ, 121, 820
- Graham, A. W., Driver, S. P., Petrosian, V., Conselice, C. J., Bershadsky, M. A., Crawford, S. M., & Goto, T. 2005, AJ, 130, 1535
- Graham, A. W., & Worley, C. C. 2008, MNRAS, 388, 1708
- Guo, Y., et al. 2009, MNRAS, 398, 1129
- Hansen, S. M., Sheldon, E. S., Wechsler, R. H., & Koester, B. P. 2009, ApJ, 699, 1333
- Häussler, B., et al. 2007, ApJS, 172, 615
- Hogg, D. W., et al. 2003, ApJ, 585, L5
- Hopkins, P. F., Cox, T. J., Dutta, S. N., et al. 2009, ApJS, 181, 135
- Immeli, A., Samland, M., Gerhard, O., & Westera, P. 2004, A&A, 413, 547
- Impey, C., & Bothun, G. 1997, ARA&A, 35, 267
- Janowiecki, S., Mihos, J. C., Harding, P., et al. 2010, ApJ, 715, 972
- Jedrzejewski, R. I. 1987, MNRAS, 226, 747
- Kauffmann, G., Heckman, T. M., White, S. D. M., et al. 2003, MNRAS, 341, 54
- Kawata, D., Mulchaey, J. S., Gibson, B. K., & Sánchez-Blázquez, P. 2006, ApJ, 648, 969
- Kimm, T., et al. 2009, MNRAS, 394, 1131
- Knapen, J. H., Shlosman, I., & Peletier, R. F. 2000, ApJ, 529, 93
- Kormendy, J. 1979, ApJ, 227, 714
- Kormendy, J., & Kennicutt, R. C., Jr. 2004, ARA&A, 42, 603
- Kormendy, J., Fisher, D. B., Cornell, M. E., & Bender, R. 2009, ApJS, 182, 216
- Kron, R. G. 1980, ApJS, 43, 305
- Lauer, T. R., Ajhar, E. A., Byun, Y.-I., et al. 1995, AJ, 110, 2622
- Laurikainen, E., Salo, H., & Buta, R. 2005, MNRAS, 362, 1319
- Laurikainen, E., Salo, H., Buta, R., & Knapen, J. H. 2007, MNRAS, 381, 401
- Lewis, I., et al. 2002, MNRAS, 334, 673
- Lintott, C. J., Schawinski, K., Slosar, A., et al. 2008, MNRAS, 389, 1179
- Lotz, J. M., Primack, J., & Madau, P. 2004, AJ, 128, 163
- Lu, T., et al. 2012, in prep. (Paper IV)
- Malin, D. F., & Carter, D. 1980, Nature, 285, 643
- Malin, D. F., & Carter, D. 1983, ApJ, 274, 534
- Maller, A. H., Berlind, A. A., Blanton, M. R., & Hogg, D. W. 2009, ApJ, 691, 394
- Marleau, F. R., & Simard, L. 1998, ApJ, 507, 585
- Menéndez-Delmestre, K., Sheth, K., Schinnerer, E., Jarrett, T. H., & Scoville, N. Z. 2007, ApJ, 657, 790
- Mihos, J. C., & Hernquist, L. 1994, ApJ, 437, L47
- Mihos, J. C., & Hernquist, L. 1996, ApJ, 464, 641
- Möllenhoff, C., Popescu, C. C., & Tuffs, R. J. 2006, A&A, 456, 941
- Muldrew, S. I., Croton, D. J., Skibba, R. A., et al. 2012, MNRAS, 419, 2670
- Naab, T., Burkert, A., & Hernquist, L. 1999, ApJ, 523, L133
- Naab, T., & Burkert, A. 2003, ApJ, 597, 893
- Nair, P. B., & Abraham, R. G. 2010, ApJS, 186, 427
- Nair, P. B., & Abraham, R. G. 2010, ApJ, 714, L260
- Norman, C. A., Sellwood, J. A., & Hasan, H. 1996, ApJ, 462, 114
- Oesch, P. A., Carollo, C. M., Feldmann, R., et al. 2010, ApJ, 714, L47
- Pannella, M., Hopp, U., Saglia, R. P., et al. 2006, ApJ, 639, L1
- Pipino, A. et al. 2012, ApJ, in prep. (Paper VI)

- Peng, C. Y., Ho, L. C., Impey, C. D., & Rix, H.-W. 2002, *AJ*, 124, 266
- Peng, Y.-j., et al. 2010, *ApJ*, 721, 193
- Peng, Y., Lilly, S. J., Renzini, A., & Carollo, M. 2012, arXiv:1106.2546
- Porter, S. C., Raychaudhury, S., Pimbblet, K. A., & Drinkwater, M. J. 2008, *MNRAS*, 388, 1152
- Refregier, A. 2003, *MNRAS*, 338, 35
- Rix, H.-W., Barden, M., Beckwith, S. V. W., et al. 2004, *ApJS*, 152, 163
- Rudick, C. S. et al. 2012a, in prep. (Paper V)
- Rudick, C. S. et al. 2012b, in prep. (Paper VII)
- Saglia, R. P., Bertschinger, E., Baggle, G., Burstein, D., Colless, M., Davies, R. L., McMahan, R. K., Jr., & Wegner, G. 1993, *MNRAS*, 264, 961
- Scarlata, C., Carollo, C. M., Lilly, S., et al. 2007, *ApJS*, 172, 406
- Schlegel, D. J., Finkbeiner, D. P., & Davis, M. 1998, *ApJ*, 500, 525
- Schweizer, F. 1979, *ApJ*, 233, 23
- Schweizer, F., Seitzer, P., Faber, S. M., Burstein, D., Dalle Ore, C. M., & Gonzalez, J. J. 1990, *ApJ*, 364, L33
- Scodeggio, M., Gavazzi, G., Franzetti, P., Boselli, A., Zibetti, S., & Pierini, D. 2002, *A&A*, 384, 812
- Scoville, N., Aussel, H., Brusa, M., et al. 2007, *ApJS*, 172, 1
- Sersic, J. L. 1968, Cordoba, Argentina: Observatorio Astronomico, 1968,
- Shao, Z., Xiao, Q., Shen, S., Mo, H. J., Xia, X., & Deng, Z. 2007, *ApJ*, 659, 1159
- Sheth, K., Elmegreen, D. M., Elmegreen, B. G., et al. 2008, *ApJ*, 675, 1141
- Shen, S., Mo, H. J., White, S. D. M., et al. 2003, *MNRAS*, 343, 978
- Simard, L., Willmer, C. N. A., Vogt, N. P., et al. 2002, *ApJS*, 142, 1
- Tal, T., van Dokkum, P. G., Nelán, J., & Bezanson, R. 2009, *AJ*, 138, 1417
- Toomre, A. 1977, *Evolution of Galaxies and Stellar Populations*, 401
- Trujillo, I., Aguerri, J. A. L., Cepa, J., & Gutiérrez, C. M. 2001, *MNRAS*, 328, 977
- Tuffs, R. J., Popescu, C. C., Völk, H. J., Kylafrs, N. D., & Dopita, M. A. 2004, *A&A*, 419, 821
- van den Bosch, F. C., Aquino, D., Yang, X., Mo, H. J., Pasquali, A., McIntosh, D. H., Weinmann, S. M., & Kang, X. 2008, *MNRAS*, 387, 79
- van der Wel, A. 2008, *ApJ*, 675, L13
- van Dokkum, P. G. 2005, *AJ*, 130, 2647
- Vulcani, B., Poggianti, B. M., Aragón-Salamanca, A., et al. 2011, *MNRAS*, 412, 246
- Weinmann, S. M., van den Bosch, F. C., Yang, X., & Mo, H. J. 2006, *MNRAS*, 366, 2
- Weinmann, S. M., Kauffmann, G., van den Bosch, F. C., Pasquali, A., McIntosh, D. H., Mo, H., Yang, X., & Guo, Y. 2009, *MNRAS*, 394, 1213
- Weinzirl, T., Jogee, S., Khochfar, S., Burkert, A., & Kormendy, J. 2009, *ApJ*, 696, 411
- Whitmore, B. C., & Gilmore, D. M. 1991, *ApJ*, 367, 64
- White, S. D. M., & Rees, M. J. 1978, *MNRAS*, 183, 341
- Wilman, D. J., Zibetti, S., & Budavári, T. 2010, *MNRAS*, 406, 1701
- Woo, J., Dekel, A., Faber, S. M., et al. 2012, arXiv:1203.1625
- Wyse, R. F. G., Gilmore, G., & Franx, M. 1997, *ARA&A*, 35, 637
- York, D. G., Adelman, J., Anderson, J. E., Jr., et al. 2000, *AJ*, 120, 1579
- Zamojski, M. A., Schiminovich, D., Rich, R. M., et al. 2007, *ApJS*, 172, 468

## APPENDIX

## A. QUALITY-CONTROL CHECKS FOR THE GIM2D MODEL FITS

## A.1. Comparison with previous works

For a number of galaxies in our sample, the SDSS New York University Value-Added Galaxy Catalog (NYU-VAGC) value added catalogue (Blanton et al. 2005) provides half-light radii and indices  $n$  from single-component Sérsic fits to the azimuthally averaged surface brightness profiles. We thus compare in Figure A1 our own best fit parameters for the single component fits, *prior to the application of our corrections* described in Section 6.3, with these previously published data. To match the VAGC definition, *circularized* radii are employed (although our own fiducial estimates, used in the analyses, are based on elliptical radii). The agreement between the two measurement sets is quite good.

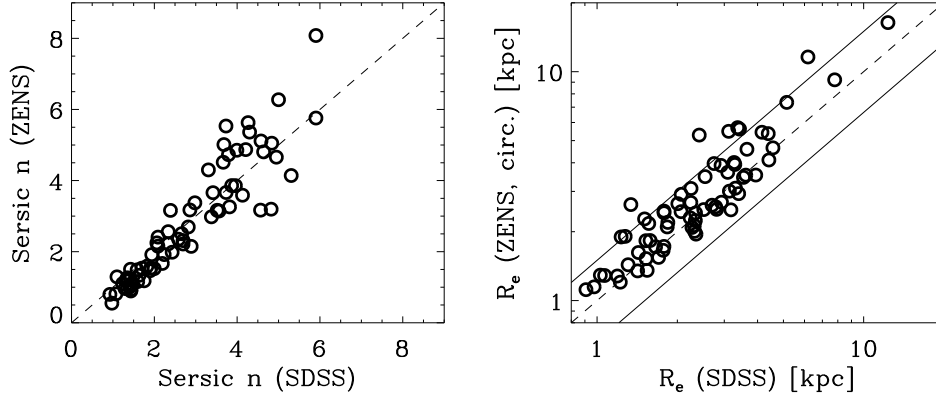


**Figure A1.** Comparison of Sérsic indices (left) and half-light radii (right) between our single-component  $I$ -band Sérsic fits and corresponding  $i$ -band single-component Sérsic parameters from the SDSS NYU-VAGC. To match these previous measurements, which use circular aperture, we plot here post-processing circularized (i.e.,  $\sqrt{ab}$ ) half-light radii also for ZENS. The dashed line in the right plot is the identity relation; the solid lines indicate a variation of a factor of 1.5.

We also show in Figure A2 a comparison between the mass-size relation obtained for the ZENS galaxies, both before and after applying the corrections outlined in Section 6.3, and the relation derived by Shen et al. 2003 in SDSS. Again circularized apertures are used in this comparison, to match the Shen et al. definition. Not surprisingly, given the global robustness of the structural parameters of disks, and more generally low Sérsic index galaxies, that we demonstrate in Section 6, the Shen et al. (2003) size-mass relation for the late-type galaxies is in excellent agreement with our relation. The Shen’s sizes for the early-types are however slightly smaller than our size estimates, a difference which is exacerbated by our corrections, which were not attempted in the SDSS analyses. For the uncorrected sizes, the difference is  $\sim 13\%$  at high masses  $\sim 10^{11} M_\odot$  and above, and increases towards lower galaxy masses, up to  $17\%$  at  $\sim 10^{10} M_\odot$ . The median size of the Shen et al early-type galaxy at this mass scale is 5.3 kpc, and our corresponding ZENS estimate is 6.2 kpc and 6.7 kpc before and after the corrections; comparatively, we expect this difference to have a limited impact on results. We further note that the Shen’s sizes are from the Sérsic fits of Blanton et al. (2003), and are thus similar to the sizes of the VAGC catalogue, which we have shown to agree well with our measurements on a one-to-one galaxy comparison. We thus attribute the small difference in size for low-mass early-type galaxies between our analysis and Shen’s to some combination of mainly three factors (in addition to the extra difference introduced by our correction scheme): (i) a difference between estimates based on elliptical apertures in ZENS and circular apertures in SDSS (which we have partly taken care of in a “post-processing” mode, by circularizing our measurements for the comparison; residual differences may however remain, and be possibly more relevant at relatively smaller sizes for relatively high Sérsic indices); (ii) a different morphological mix in between us and Shen et al. who use a split in Sérsic index to define their morphological classes; and (iii) a difference in the stellar mass calibration, possibly preferentially for “red” and/or systems with a comparable contribution from old and young stellar populations (as the galaxies in the relevant regime of stellar mass and Sérsic index may have). We discuss in some detail the comparison between our galaxy stellar masses and available SDSS estimates in Paper III.

## A.2. Validation of the GIM2D bulge+disk models

Caution should be exercised in using blindly the GIM2D double component results, as a number of factors can produce profiles which do not correspond to a meaningful bulge+disk decomposition (see also Allen et al. 2006 for an extensive discussion on this subject). For this reason, all residuals images, models and profiles obtained from GIM2D were visually inspected to look for possible failure of the fitting algorithm and to identify physically-reasonable double-component



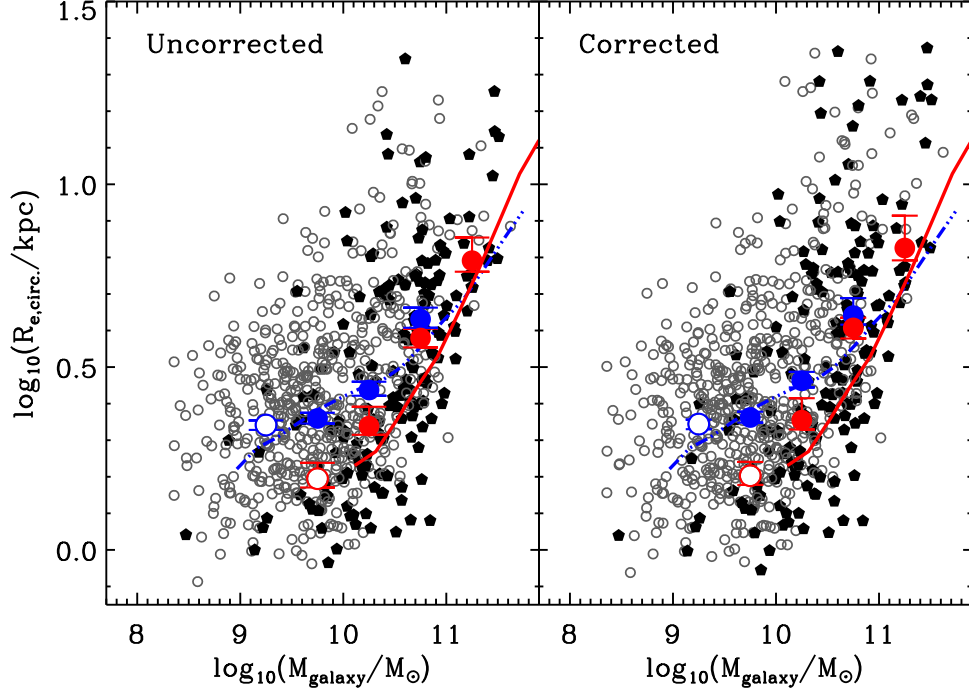


**Figure A2.** Comparison of the mass-size relation between our ZENS sample and the early- (red solid line) and late-type (dashed-dotted blue line) samples of Shen et al. 2003. The Shen’s red and blue lines connect median values of sizes in the corresponding stellar mass bins (adapted from their Figure 11). The left panel shows results before applying to our data the corrections described in Section 6.3; corrected sizes are shown in the right panel. Empty gray circles are ZENS galaxies classified as intermediate- and late-type type disks; filled black pentagons are ZENS ellipticals, S0s and bulge-dominated spirals. The median values for these two broad ZENS morphological samples are shown with large red symbols (E, S0 and bulge-dominated spirals grouped together) and large blue symbols (intermediate-type and late-type disks group together). White symbols with blue/red contours indicate ZENS data in mass bins below the ZENS mass completeness for the relevant morphological types. Post-processing circularized ZENS radii are again used for consistency with the SDSS sample.

models. As in Allen et al. (2006), we analyze the radial surface brightness profiles of bulges and disks to identify problematic models which would not be recognized as unphysical by simply looking at the fit  $\chi^2$  or at residual images. To this purpose we analyzed the surface-brightness profiles of the bulge and disk along both the semi-major and semi-minor axis; given that the two components can be twisted by several degrees, this allow us to make a consistent comparison.

For all galaxies for which we attempted a (Sérsic-profile bulge plus exponential-profile disk) decomposition, i.e., all galaxies which are not classified as ellipticals or irregulars, we classify the double-component model fits into the following categories:

1. bona-fide bulge+disk decompositions. These models have to satisfy the following criteria: the bulge dominates the light in the inner regions, and the disk component dominates at large radii; furthermore, the bulge half-light radius has to be smaller than the disk half-light radius. In the *B*- and *I*-bands, precisely 64% and 63% of the galaxies in our sample fall into this class.

In  $\sim 13\%$  of galaxies in this category, the above fits result however in rather elongated bulges ( $0.6 < \epsilon < 0.7$ ). A closer inspection showed that a good fraction of these models are associated to galaxies classified as barred disks. In a few other cases, a resolved bar is not observed and hence these central structures may either be unresolved bars or truly flattened bulges (although we ourselves wonder whether such distinction is meaningful, not only from a descriptive but also from a physical perspective). It has been argued that neglecting the bar component when modeling the light profile can affect the best fit parameters and cause an over-estimation of the bulge-to-total ratio of a factor of two to four, and an artificial increase of bulge effective radii (Laurikainen et al. 2005, Gadotti 2008, Weinzirl et al. 2009; although again, we do not necessarily agree on the philosophy behind such analyses). In any case, to highlight possible degeneracies between bulge and bar components, when appropriate we will discuss our results with and without these galaxies.

2. Another 21% and 11% *B* and *I* models are classified as “pure” (bulge-less) disks ( $B/T = 0$ ).
3. For the remaining  $\sim 20\%$  of disk galaxies, the bulge+disk decompositions failed to match either of the above categories. We separate a few cases within this class. In about 10% of such galaxies, the bulge component always dominates the surface brightness profile. These models are not necessarily unphysical decompositions: some

**Table A1**  
 Fraction of reliable single Sérsic fits and bulge+disk decompositions for  
 galaxies of different morphological types

Type	Reliable Single Sérsic Fits	Reliable Bulge+Disk Fits
<i>B</i> -Band	Total (94%)	Total (86%)
Elliptical	100%	-
S0	95%	86%
Bulge-dom. Spiral	96%	79%
Intermediate Spiral	89%	92%
Late Spiral	97%	83% <sup>a</sup>
<i>I</i> -Band	Total (95%)	Total (82%)
Elliptical	100%	-
S0	95%	84%
Bulge-dom. Spiral	96%	82%
Intermediate Spiral	90%	91%
Late Spiral	97%	75% <sup>a</sup>

**Note.** — The fraction of reliable single-Sérsic and bulge+disk decompositions (the latter obtained either with GIM2D or with GALFIT) for each morphological type, separately for the *B*- and *I*-bands. Elliptical are by definition galaxies very well fit by a single-Sersic component only, whose  $n$  index is  $> 3$ .

<sup>a</sup> In the fraction of failed bulge+disk decompositions we include those galaxies in which the formal Sérsic-bulge profiles dominates at all radii with an  $n < 1.5$ . These failed disk+bulge decompositions identify however good disk-dominated cases; these are 9% and 15% of the late-type disks in the *B*- and *I*-band, respectively.

galaxies which fall in this category have a Sérsic indices  $n < 1.5$  and are simply disk-dominated galaxies. GIM2D hence correctly recovers the information that the structure is dominated by the disk component. Nonetheless the  $B/T$  ratio are not considered as valid.

We consider instead as truly unphysical those fits which result in a disk half-light radius that is larger than the bulge’s half-light radius, and/or in which the disk and bulge profiles are “inverted”, i.e., the disk dominates in the inner regions and the bulge dominates in the outer regions. Also unphysical were judged those fits in which the bulge and disk surface brightness radial profiles cross twice (again, see also Allen et al. 2006).

We re-fitted all these problematic cases with the software GALFIT (Peng et al. 2002), which allows for more stringent constraints on the input parameters; we furthermore fitted the galaxies profiles within 1.5 Petrosian radii. We were able to recover 45% of the previously-classified as unphysical fits. For a total of 14% (*B*-band) and 18% (*I*-band) of first-epoch ZENS disk galaxies, however, also GALFIT did not converge to a physical bulge+disk decomposition. The fraction of successful bulge+disk decompositions for each morphological class are summarized in Table 3. The largest formal failure rate is observed for the late-type disks, as in this case many fits results in a dominating Sérsic-bulge profile with  $n < 1.5$ , as mentioned before. These are meaningful fits, but not meaningful bulge+disk decompositions; these systems are considered to be single-component, disk-dominated galaxies. Excluding these late-type disks, galaxies which do not have bulge+disk decompositions in either one or both filters sum up to  $\sim 15\%$  of the S0- to intermediate-type disk sample.

### A.3. Galaxies with discrepant single Sérsic and bulge+disk half-light radii

We show in Figures A3 and A4 the surface brightness profiles and residual images for those galaxies which have *I*-band half-light radii provided by the single Sérsic fits that are substantially larger the half-light radii inferred, in the same passband, from their bulge+disk decompositions (by more than a factor 1.5; see Section 4.2.1).

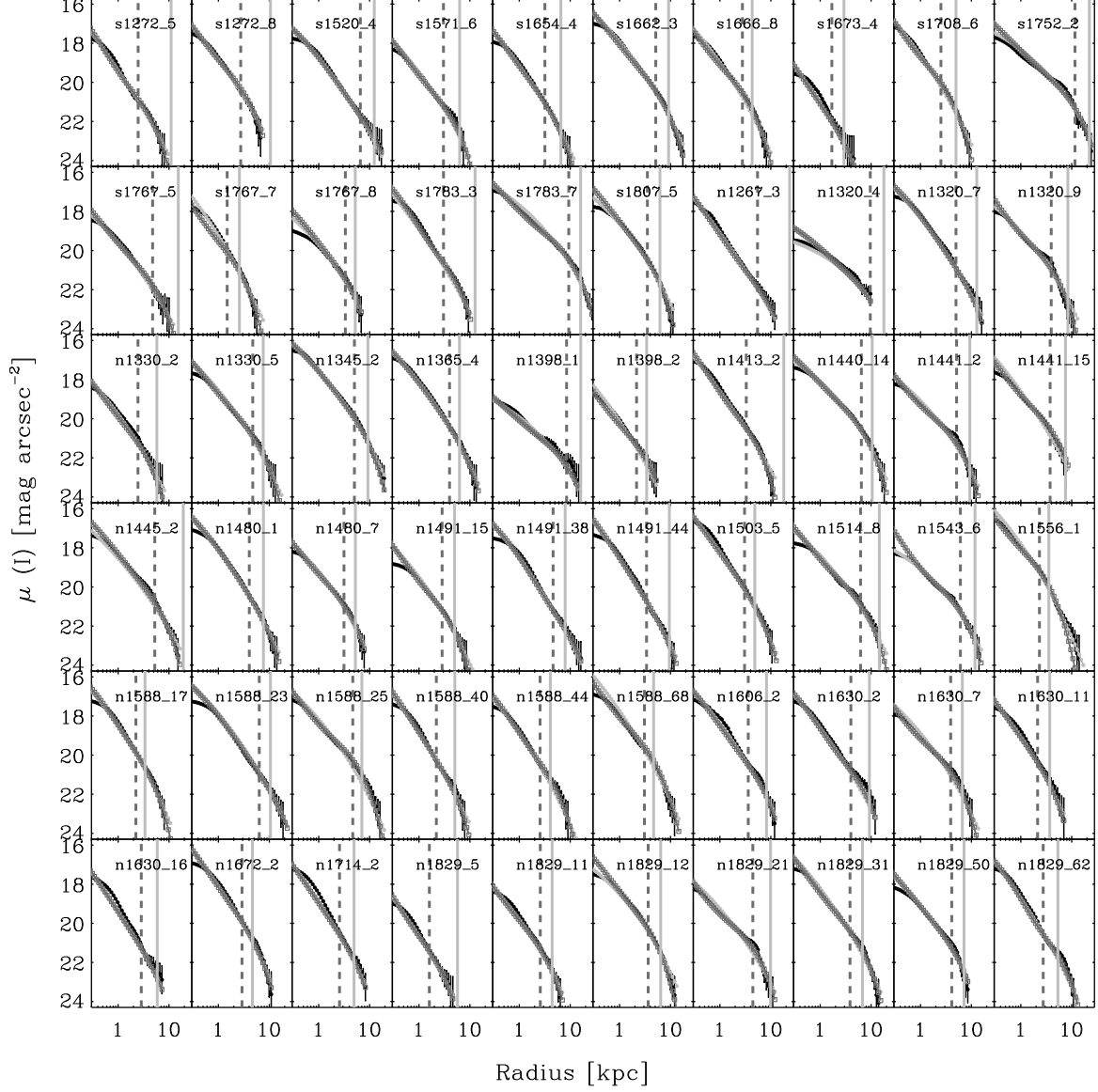


**Figure A3.** Surface brightness profiles for galaxies plotted with empty points in Figure 7, i.e., those galaxies which have more than a factor 1.5 difference in the half-light radii inferred from their single Sérsic fits and from their bulge+disk decompositions. The observed surface brightness profiles obtained from the IRAF `ELLIPSE` routine are shown with black point with errorbars. The light and dark gray points are the analytical profiles from the single and double component fits. The vertical dashed and solid lines mark the half-light radii from the bulge+disk decompositions and single Sérsic fits, respectively. We do not have any formal reason to exclude either fits, according to our quantitative quality-control criteria; we therefore leave these galaxies (and measurements) in our sample, but flag these galaxies so as to monitor their impact on our analyses.



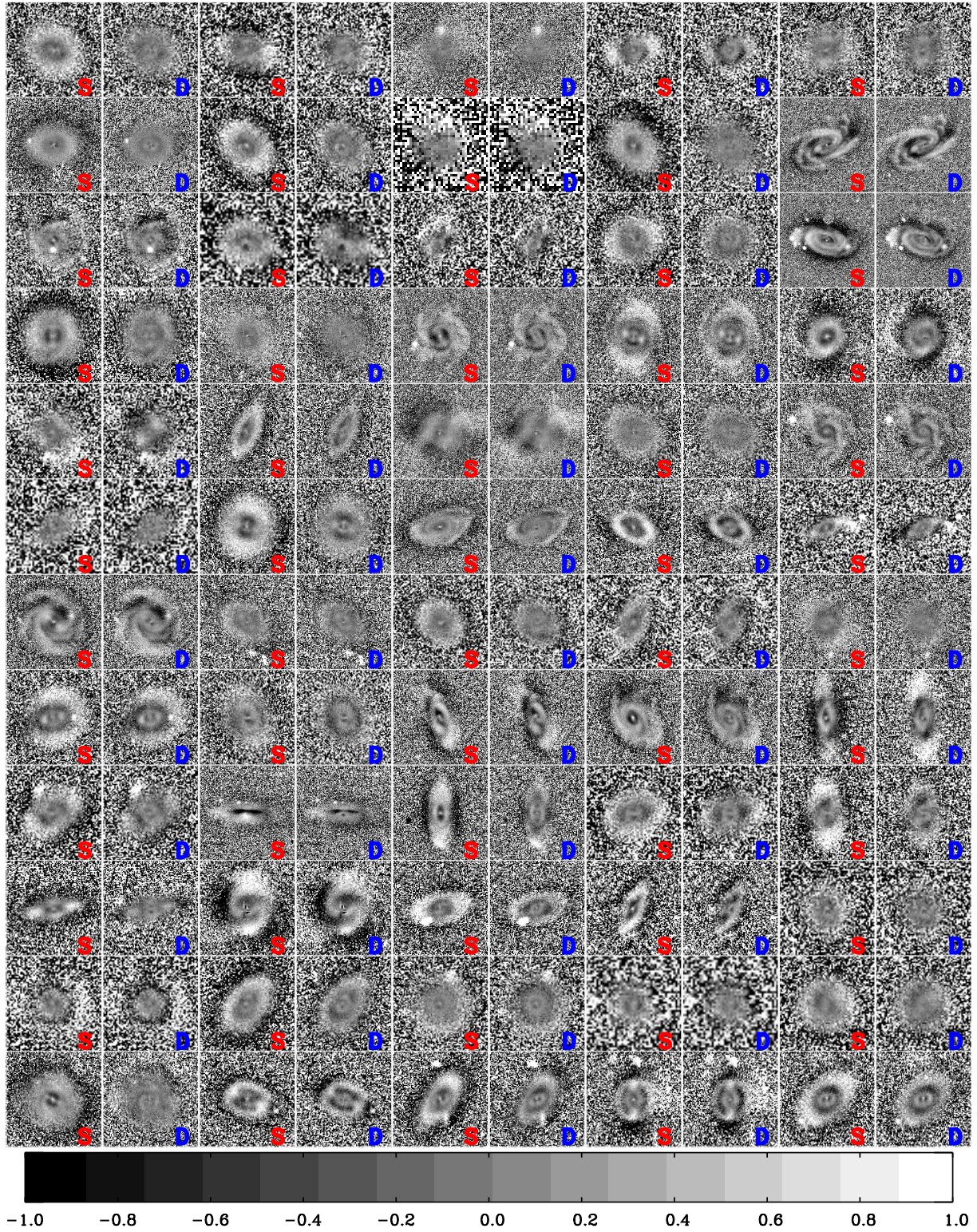


**Figure A4.** For each galaxy in Figure A3 we show the normalized residual images (i.e.,  $(I_{real} - I_{model})/I_{real}$ ) from the single- and double-component fits (marked with 'S' and 'D', respectively). The fractional residual level is indicated by the gray scale at the bottom of the plot. The residuals of the single- and double-component fits are qualitatively very similar, and quantitatively not so different to enable the formal exclusion of either fits.



#### A.4. Properties of galaxies with no reliable GIM2D fits

As discussed in Section 4, reliable Sérsic fits and bulge+disk decompositions are not available for some galaxies in our sample (see also Appendix A.2). We inspected whether the galaxies that remained without either or both analytical fits were somehow a biased component of our ZENS sample. Figure A5 shows the distributions of galaxy masses and  $I$ -band half-light radii for such galaxies with no GIM2D models. Galaxies without any (single- and double-component) size measurements, we use the ZEST+ radii, *corrected* as described in Section 6.3. To establish the presence/absence of possible biases, for comparison we also show the global distributions of masses and sizes of galaxies with reliable analytical fits. A summary of the fraction of failed models for each morphological type is given in Table 3.

Galaxies with no single Sérsic fits tend to populate the high mass/radius tail of the distributions and their incidence is highest for intermediate-type disks. For these galaxies we will use in our ZENS analyses the corrected ZEST+ sizes, which, on the remaining galaxies, we have shown to be in excellent agreement with the (corrected) sizes derived from the analytical fits; only 5% of galaxies are in this category. We hence reckon that the impact on the final results will be in any case negligible. Although the overall success of the bulge+disk decompositions is lower than the success rate of the single-component fits (see Table 3), galaxies with no bulge and disk parameters are more uniformly distributed in mass and size relative to the global ZENS population. It is thus reasonable to assume that the exclusion of these galaxies from analysis based on bulge/disk parameters will lower the statistical significance of the results, but should not introduce strong biases.

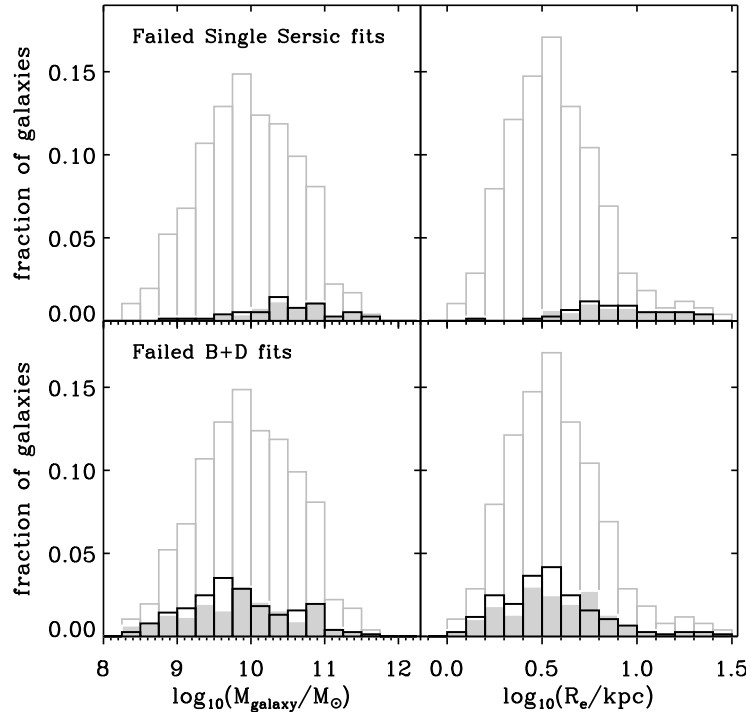


**Figure A5.** Distribution of galaxy masses and  $I$ -band corrected sizes (see Section 6) for the total sample of galaxies (empty, light gray histograms) and for galaxies with no reliable GIM2D Sérsic fit (top) or bulge+disk decompositions (bottom). The black histogram is for galaxies with no fit in the  $I$ -band and the filled dark-gray histogram for failed fits in the  $B$ -band. All histograms are normalized to the total number of galaxies in our sample. For galaxies which do not have half-light radii derived from the single Sérsic fits we use in this figure the corrected ZEST+ radii.

## B. CORRECTION MAPS FOR SIZES AND MAGNITUDES: VARIATIONS WITH PSF SIZE AND ROBUSTNESS TOWARDS CONTAMINANTS

### B.1. Correction maps obtained for the best and worst PSF

Correction maps for sizes and magnitudes, similar to those shown in the main text in Section 6 for the median PSF-FWHM of the ZENS WFI  $I$  images, are shown here for the two “bracketing” – i.e., the best and the worst – PSF FWHM values our dataset. A comparison of the corresponding correction maps derived for the three different PSF sizes clearly shows the major impact of PSF-blurring in the (uncorrected) structural measurements. The implementation of our correction maps rends all measurements comparable onto a consistently calibrated grid.

### B.2. The effect of contaminants on the derivation of the corrections

As commented in Section 6 for the ZEST+ measurements, there are regions of the observed  $C$ - $\epsilon$ - $mag$ - $R_e$  hyper-plane which are highly degenerate: they can be populated by models with intrinsic parameters which originate in that same region of parameter space, as well as by models with very different “intrinsic” ellipticity or concentration, which are scattered into that given bin by observational errors. It is thus important to verify that the size and magnitude corrections that we infer in these regions of parameter space are not strongly dependent on the precise way in which we populate the input grid of simulated models. If this were the case and without an a priori knowledge of the relative fraction of the two populations in the real Universe, the derivation of the corrections in the parameters space would be affected by biases introduced by the precise choice of the simulation grid. To assess whether our correction suffer from this problem, we calculated the corrections in these “troublesome” grid points by using only those models with original, intrinsic  $\epsilon - C$  values in that same bin, and, for comparison, using only models which were originated in a different  $\epsilon - C$  bin and were scattered into that bin by measurement errors. In many cases we found that both model samples gave consistent results for the corrections to the magnitude and sizes, which we could then use for our real galaxies. This is illustrated in Figure B5 for the lowest ellipticity bin, which is also the one with the highest contamination, and for models convolved with the typical  $I$ -band PSF. The corrections derived with the two sub-samples are reassuringly very similar over a wide are of size-magnitude space (and thus very similar to the global corrections presented in Figure 9). We therefore argue that our implementation of the correction scheme of Section 6.3 is free from biases introduced by the choice of the simulation grid.

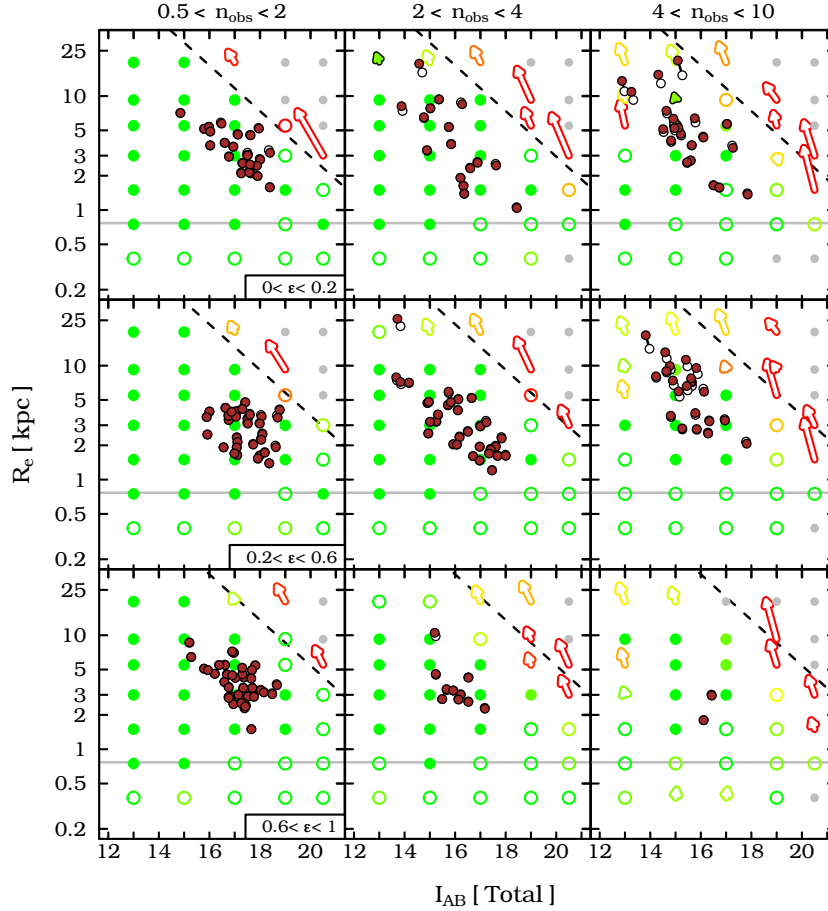


**Figure B1.** As in Figure 8 but for galaxy models convolved with the best PSF ( $0.7''$ ) measured in the  $I$ -band WFI ZENS images

### C. ZENS GALAXIES SPLIT IN THEIR MORPHOLOGICAL CLASSES

Finally we show the postage-stamp images of the ZENS galaxies, split according to their morphological type. The relevant structural parameters characterizing each type are indicated on top of each stamp image. The  $n > 3$  single-component profiles that *define* our elliptical galaxy sample are also shown.

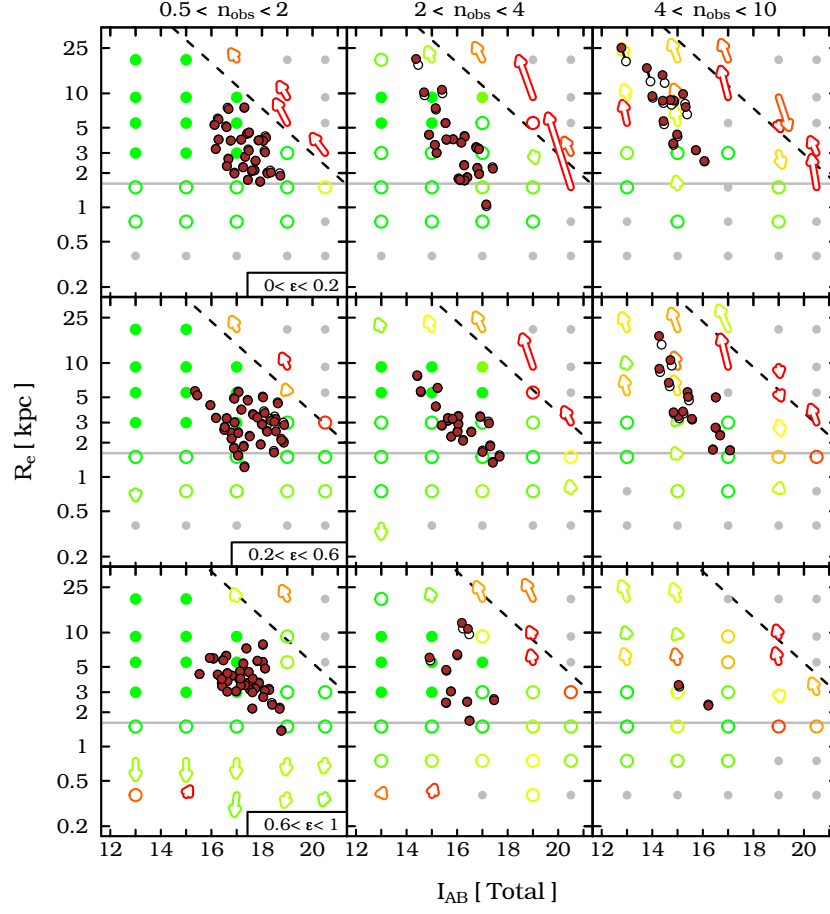


**Figure B2.** As in Figure 8 but for galaxy models convolved with the worst PSF ( $1.5''$ ) measured in the  $I$ -band WFI ZENS images

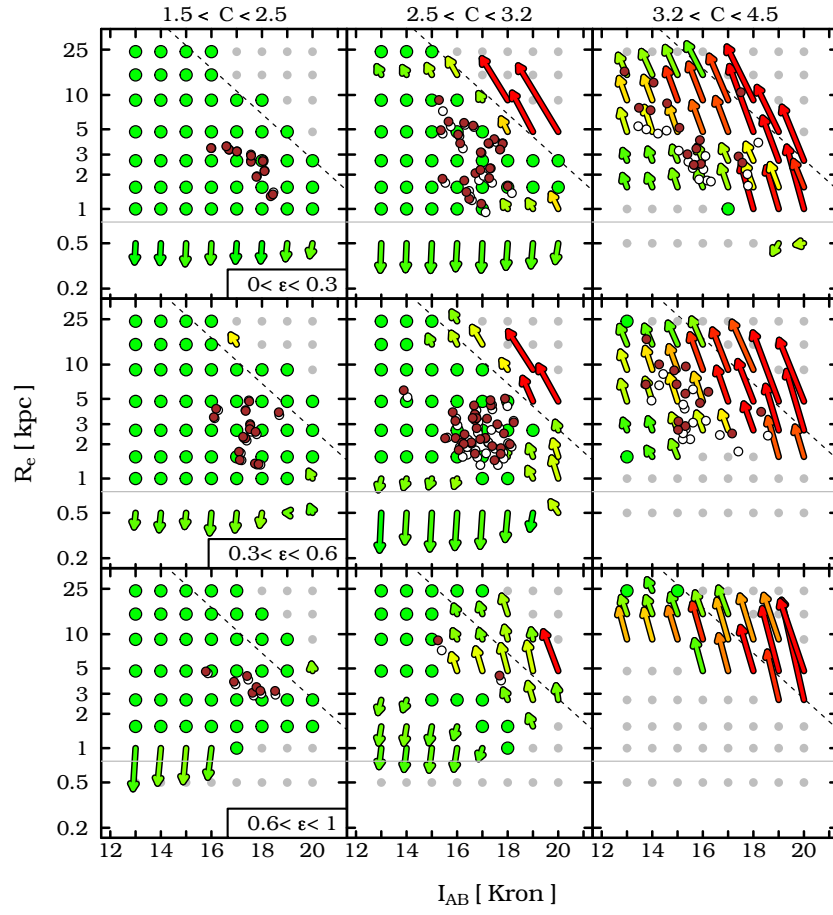


**Figure B3.** As in Figure 9 but for galaxy models convolved with the best PSF ( $0.7''$ ) measured in the  $I$ -band WFI ZENS images



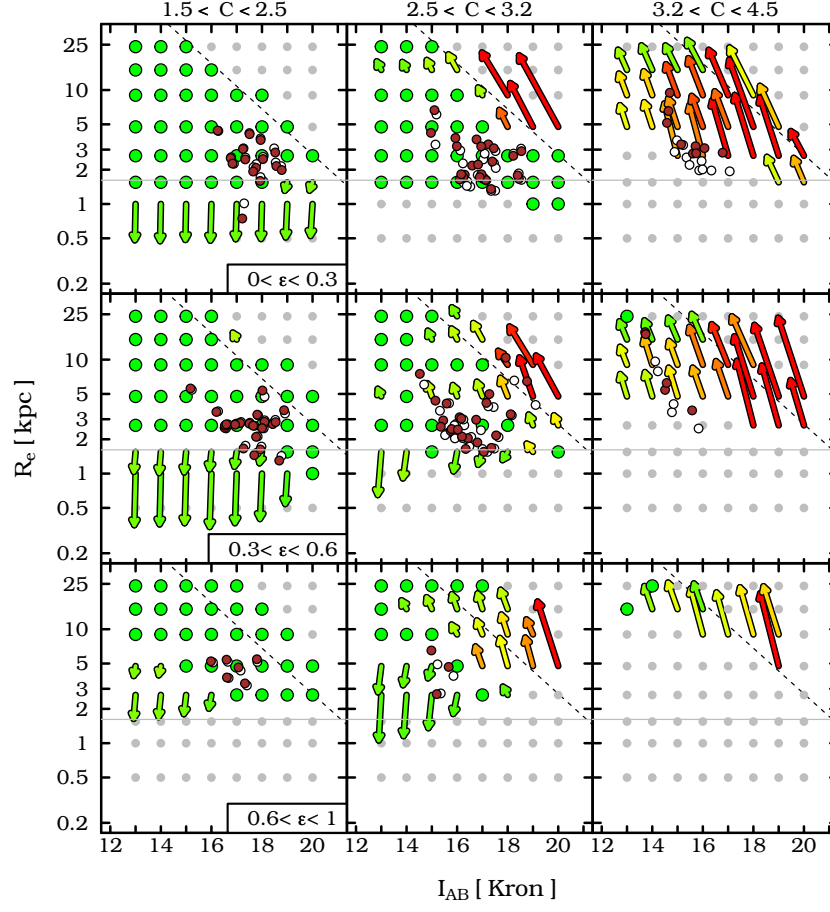


**Figure B4.** As in Figure 9 but for galaxy models convolved with the worst PSF ( $1.5''$ ) measured in the  $I$ -band WFI ZENS images

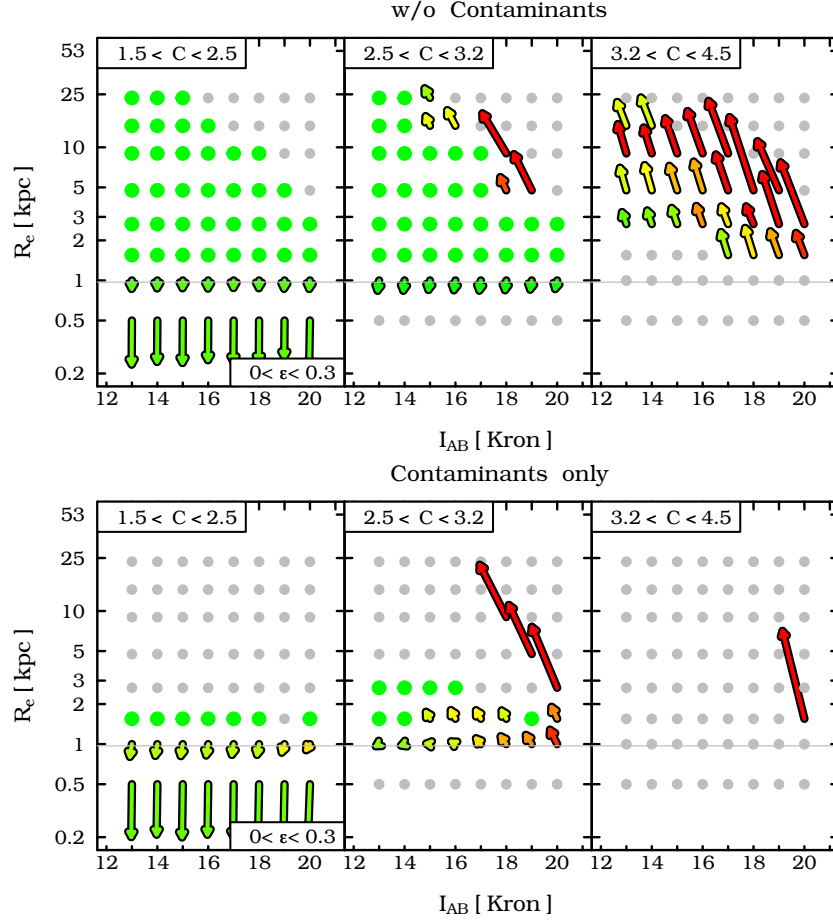


**Figure B5.** Comparison between the size-magnitude correction grid obtained from galaxies whose intrinsic parameters lie within the same  $\epsilon$ - $C$  bin (upper panels, “without contaminants”), and from galaxies with  $\epsilon$  and/or  $C$  values outside of the measured bin, which are scattered into the latter by measurements errors (lower panels; “contaminants only”). The comparison is shown for the lowest ellipticity bin, which suffers from the highest contamination of scattered galaxies into low concentration bins, and for the median PSF FWHM in the WFI ZENS data; similar results hold for all PSF sizes. Corrections for sizes and magnitudes obtained from “indigenous” and “scattered” models are well in agreement with each other, indicating that our correction maps do not depend significantly on the precise way we populate our simulation grid.

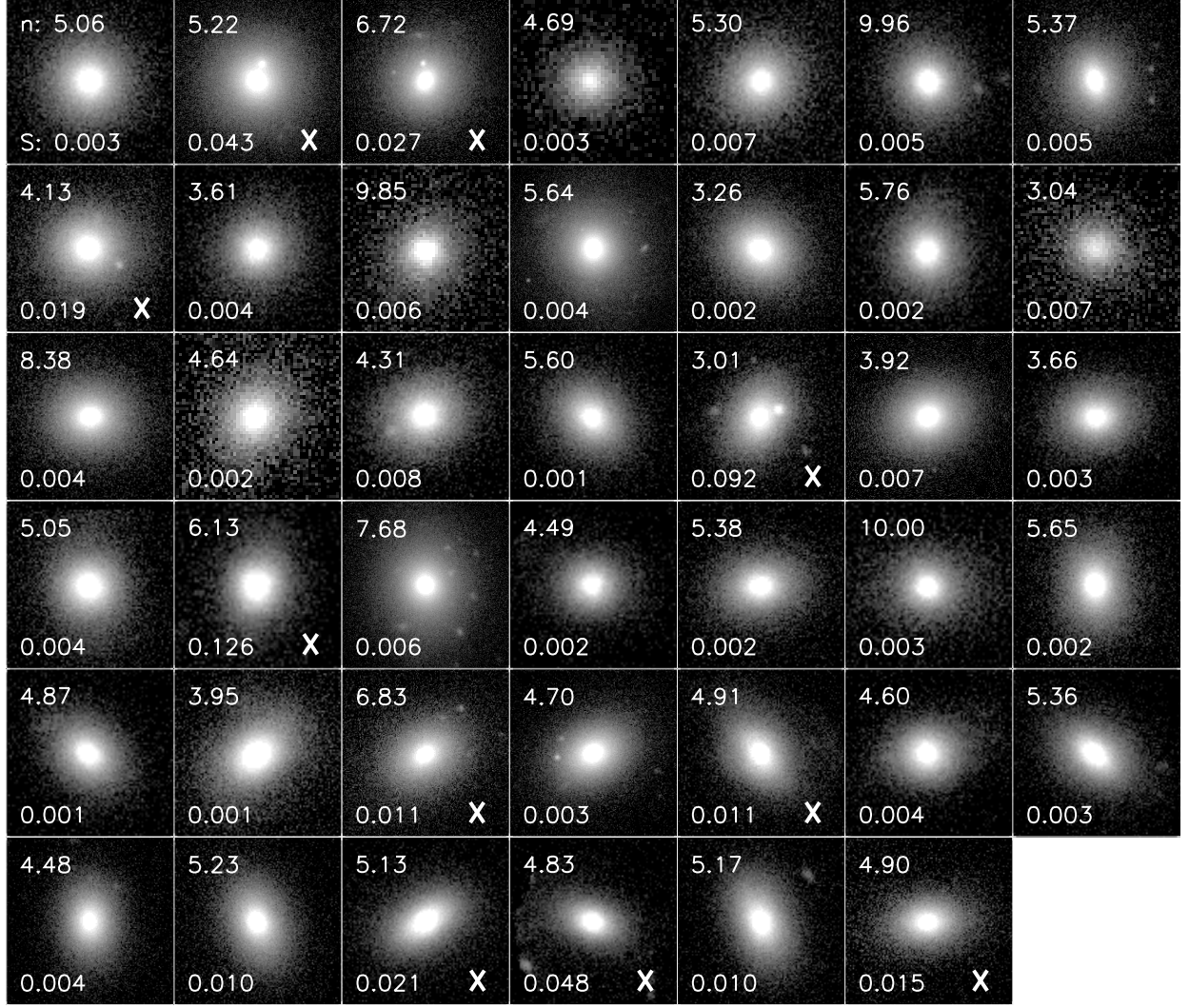


**Figure C1.** *I*-band stamp images, cleaned from neighboring objects, of ZENS galaxies classified as ellipticals. Galaxies are ordered from top-left to bottom-right in order of increasing ellipticity. The criteria defining galaxies falling into the elliptical class are given in Figure 17. Specifically, elliptical galaxies have corrected Sérsic indices  $n > 3$  and *B*-band smoothness  $S_{B-band} < 0.01$ . Furthermore their surface brightness must be perfectly fit by a single-component Sérsic profile, as shown in Figure C2. The value of the corrected Sérsic index  $n$  (top left) and *B*-band smoothness (bottom left) is indicated in each stamp. There are some exceptions, in which we maintain an elliptical classification despite the galaxy fails the  $S_{B-band}$  criterion. These galaxies are marked with a white cross on the image; in a large fraction of them, the increased smoothness is associated with a bright star cluster or small galaxy clearly visible in the stamps. For the other such galaxies, our visual inspection did not detect any clear substructure which would suggest a different classification. The surface brightness profiles obtained from the GIM2D fits of all the elliptical galaxies are shown in Figure C2, and show that these systems are genuine single-Sérsic galaxies. This condition, together with the absence of a faint disk in the residual images, was given priority in the classification relative to the smoothness criterion.

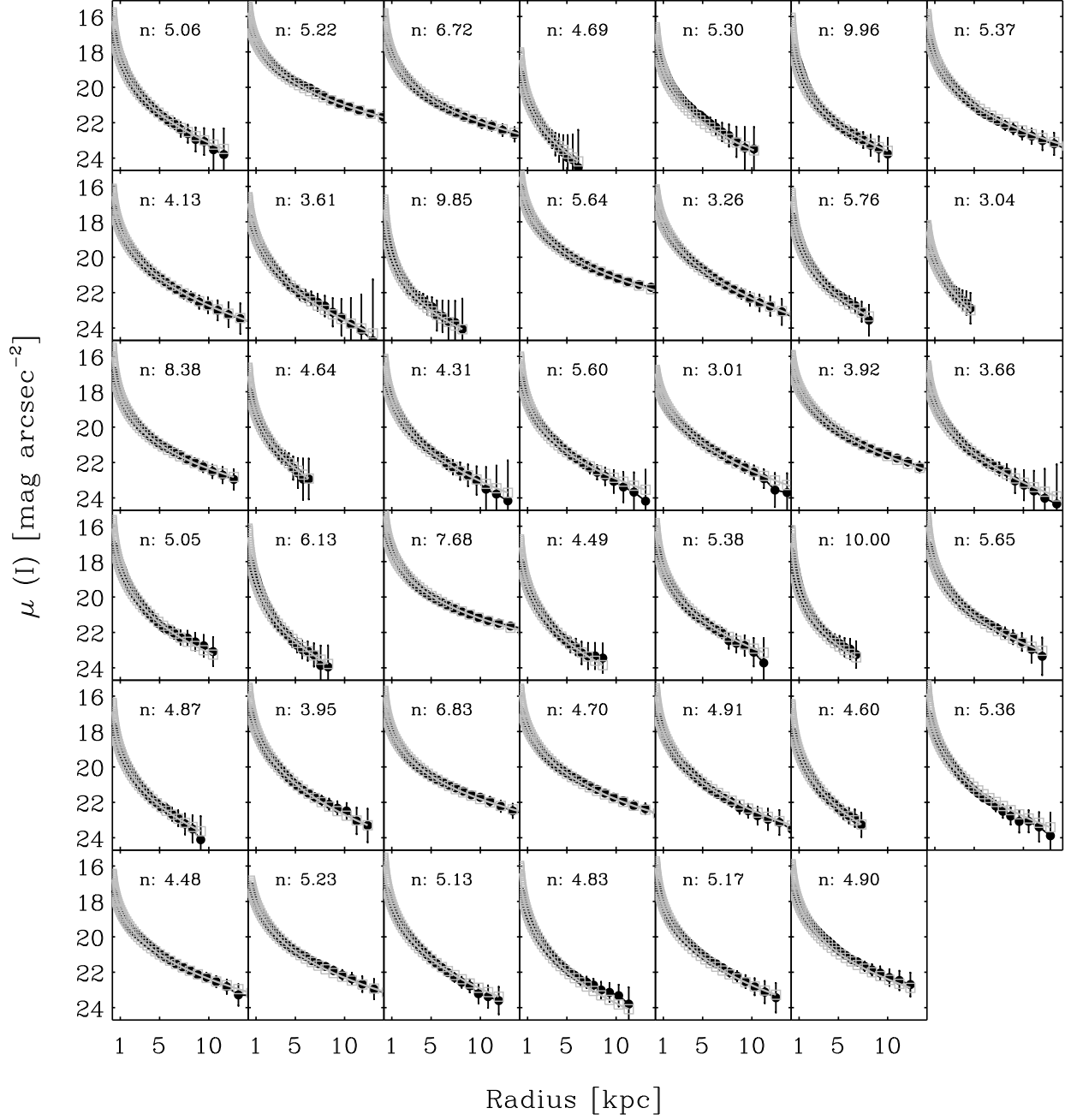


**Figure C2.** *I*-band surface brightness profiles and best fit single-Sérsic profiles for galaxies classified as ellipticals. The filled black points with error-bars are the surface brightness profiles from the **ELLIPSE** isophote fits, the gray empty squares show the single-Sérsic GIM2D models. Galaxies classified as ellipticals are required to be well fitted by a single component from the inner galaxy regions out to the outermost measured points. Each panel shows the value of the Sérsic index of the single-component fits.

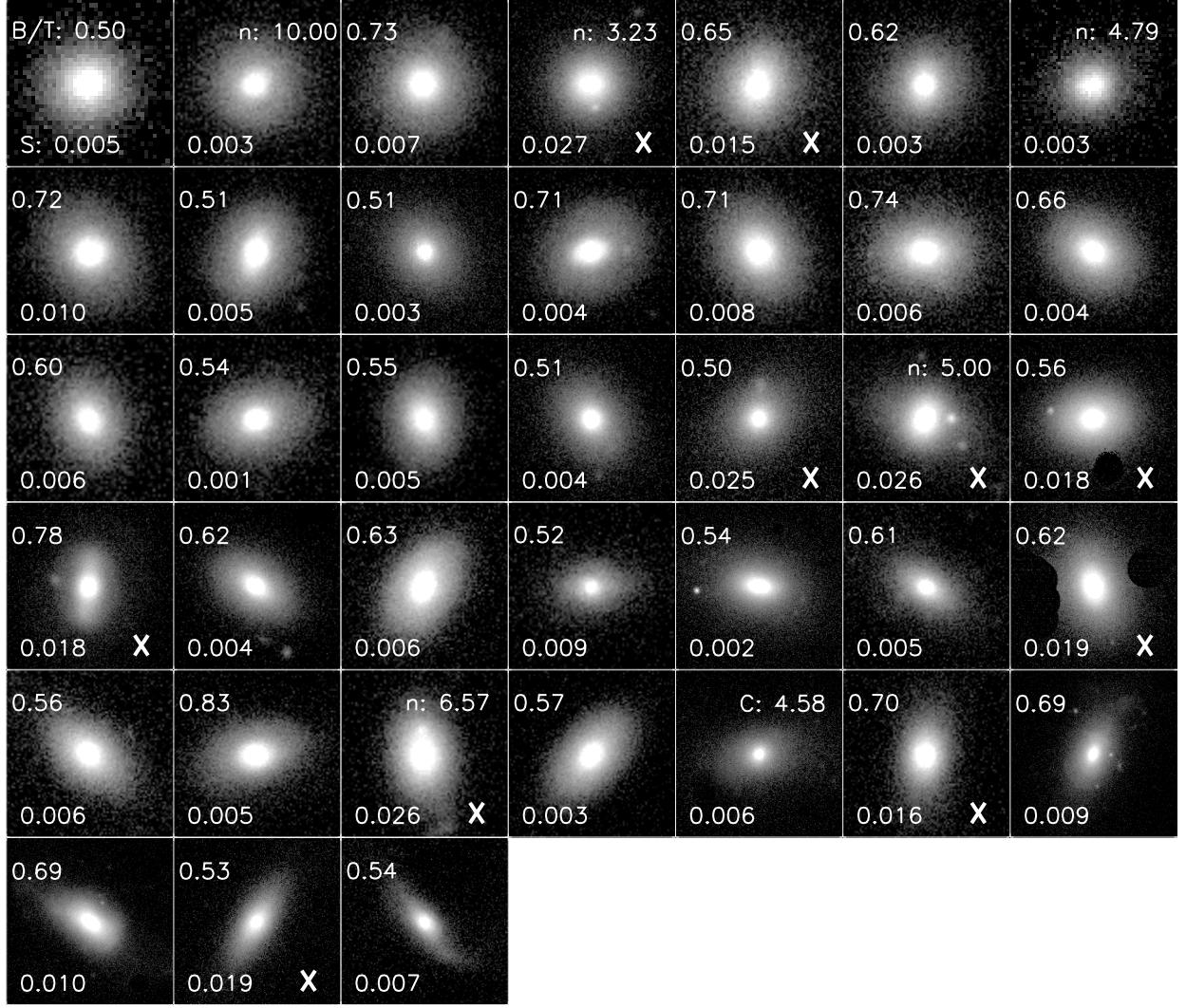


**Figure C3.** *I*-band postage-stamp images, cleaned from bright neighboring objects, of ZENS galaxies classified as S0s. These galaxies are defined to have *I*-band  $B/T > 0.5$  (or either *I*-band  $n > 2.5$  or  $C > 3.3$ , when no  $B/T$  decomposition is available) and *B*-band smoothness index  $S_{B-band} < 0.01$  (unless faint spiral arms are visible, in which case the galaxies are classified as a bulge-dominated spiral, or, in contrast, the smoothness is evidently boosted by e.g., bright star-clusters or small companion galaxies etc., in which case the galaxies are kept in the S0 class). The values of  $B/T$  (top left) and smoothness (bottom left) are indicated in the stamps. For those S0 galaxies with no reliable bulge+disk decomposition we report the value of the corrected Sérsic index or corrected concentration (if also no single-component index  $n$  is available; top right). Also in this class there are a few exceptions, which are highlighted with white cross, i.e., galaxies with  $S(B) > 0.01$ , as for the ellipticals, in seven out of ten of which a bright star-cluster/companion is again the reason for the increase in  $S_{B-band}$ ; in one other case, the boosted value of  $B$  smoothness is associated with residuals due to the gaps in the WFI detectors. Two remaining galaxies are moderately inclined systems but do not show any visible dust lane; for this reason they are included in the S0 sample.

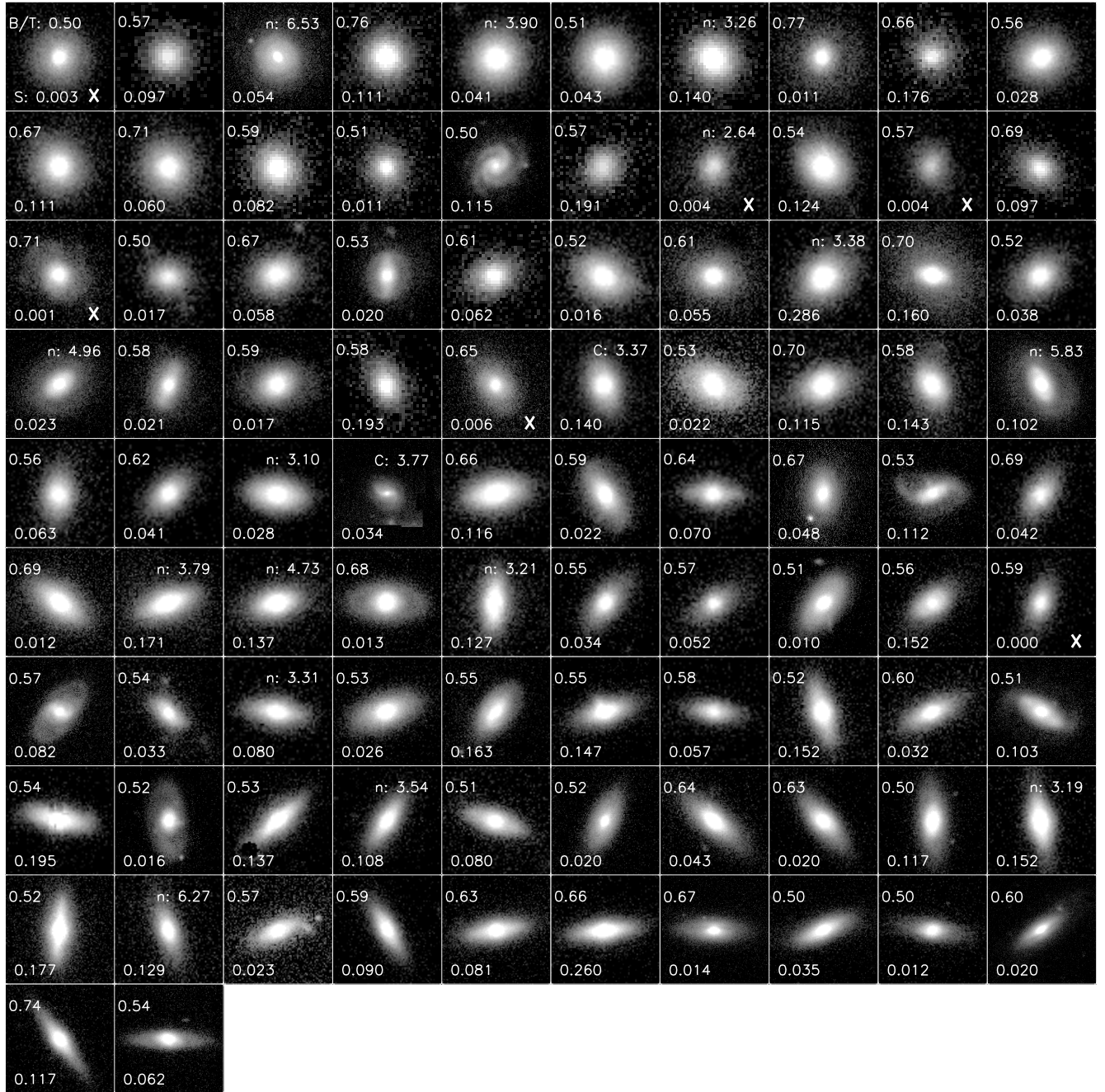


**Figure C4.** *I*-band postage-stamp images, cleaned from bright neighboring objects, of ZENS galaxies classified as bulge-dominated spiral galaxies. These galaxies have *I*-band  $B/T > 0.5$  (or *I*-band  $n > 2.5$ , when no  $B/T$  decompositions are available, or  $C > 3.3$  if also the latter is missing) and either *B*-band smoothness parameter  $S_{B-band} > 0.01$  or visible spiral arms. Numbers on the stamp are as in Figure C3. The crosses highlight those galaxies which have  $S_{B-band} < 0.01$  but visual inspection reveals faint spiral arms.



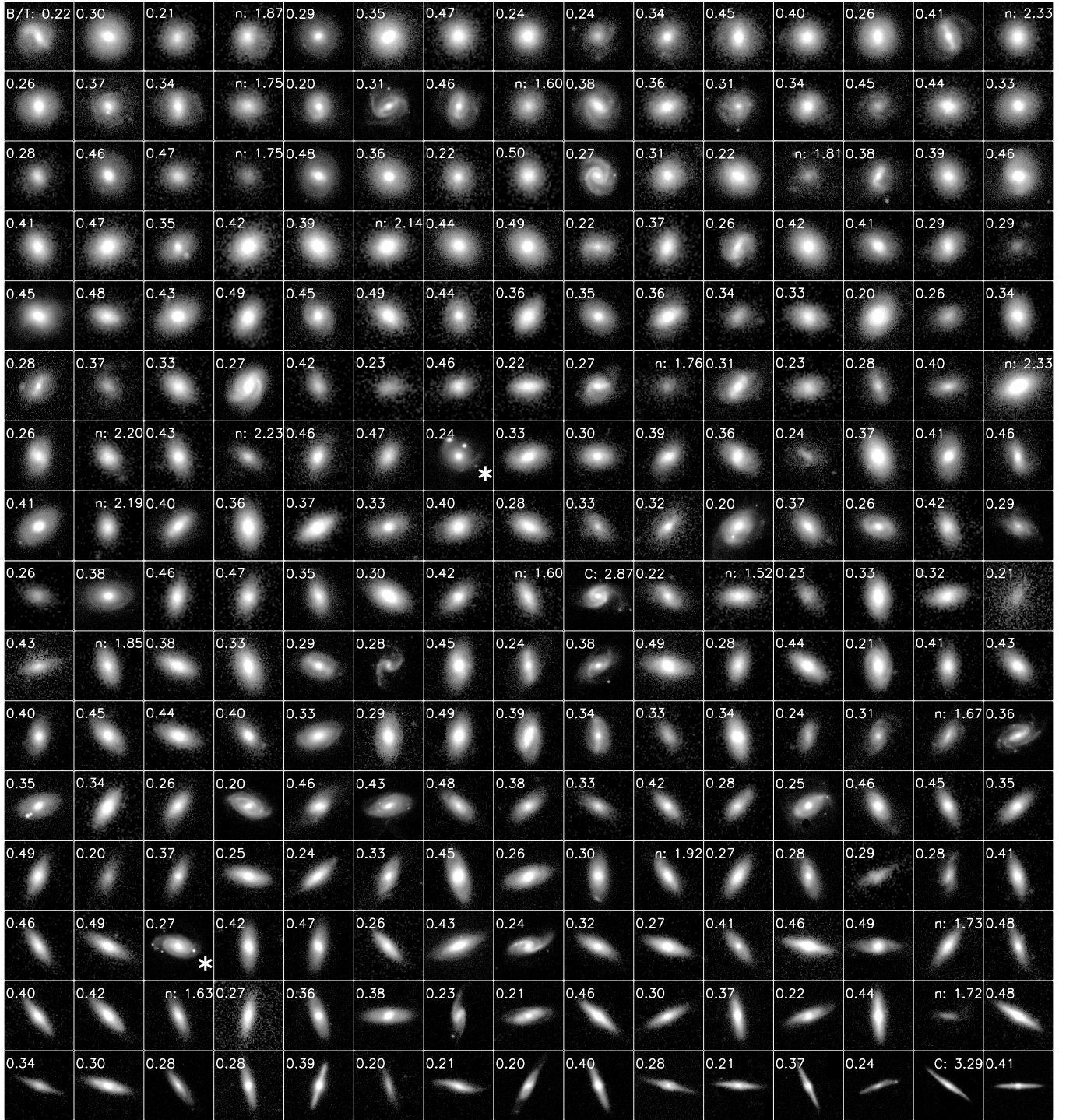


**Figure C5.**  $I$ -band postage-stamp images, cleaned from bright neighboring objects, of ZENS galaxies classified as intermediate-type disks. To fall into this class galaxies must have  $I$ -band  $0.2 < B/T < 0.5$  or, alternatively,  $1.5 < n < 2.5$ , when no valid bulge+disk decomposition is available (or  $2.8 < C < 3.3$  if also the Sérsic index is missing). Numbers on the images are the  $B/T$  ratios of each galaxy or the Sérsic index (or concentration parameter) when no  $B/T$  (and also no  $n$ ) is available. Stamp images marked with an asterisk are for those galaxies which have low  $M_{20}$  indices, and thus lie outside the global relations in the bottom panels of Figure 18.

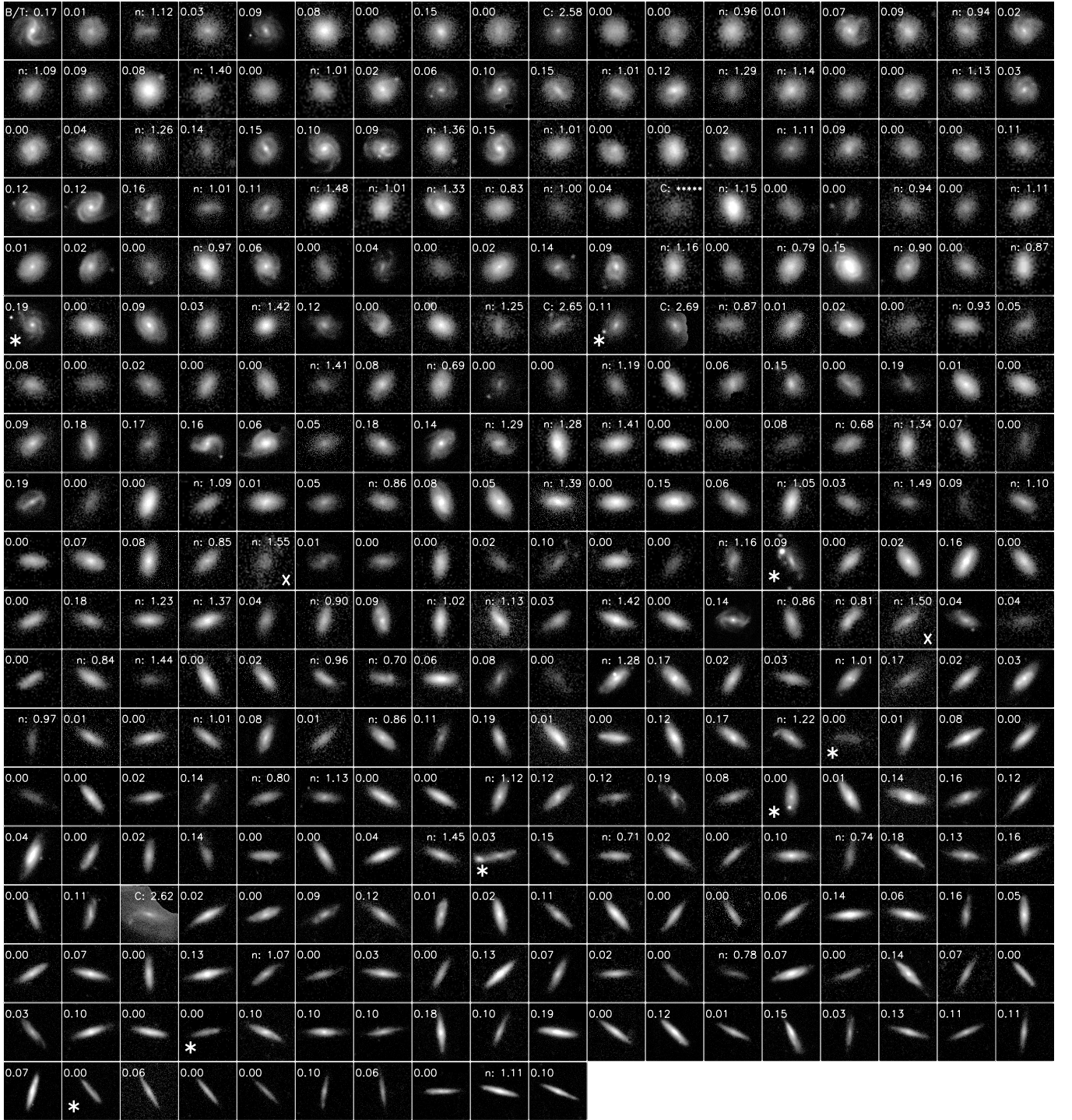


**Figure C6.** *I*-band postage-stamp images, cleaned from bright neighboring objects, of ZENS galaxies classified as late-type galaxies. To fall into this class galaxies must have *I*-band  $B/T < 0.2$  or  $n < 1.5$  (or  $C < 2.8$  if also the Sérsic index is missing), when no valid bulge+disk decomposition is available. As in Figure C5, outliers in the bottom panels of Figure 18 are marked with an asterisk. Two galaxies with high concentration, highlighted with a 'X' sign, were kept in this class after further visual inspection (respectively they have  $C=3.23$  and corrected Sérsic index  $n = 1.55$ . For the first galaxy the concentration index is likely affected by a bright star lying close to the galaxy).



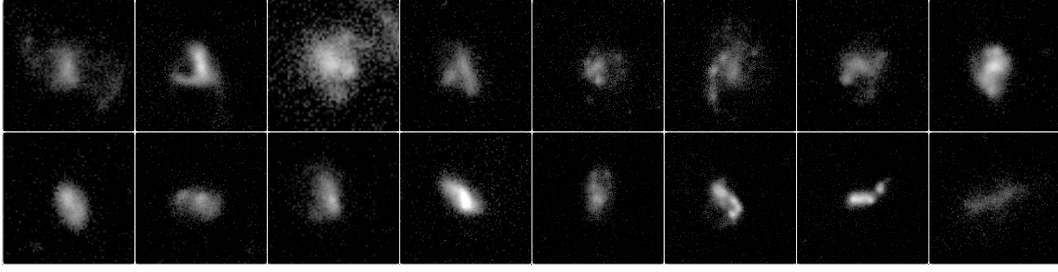


**Figure C7.** *B*-band postage-stamp images, cleaned from bright neighboring objects, of ZENS galaxies classified as irregular/interacting systems. These galaxies were visually identified as systems with disturbed morphologies.

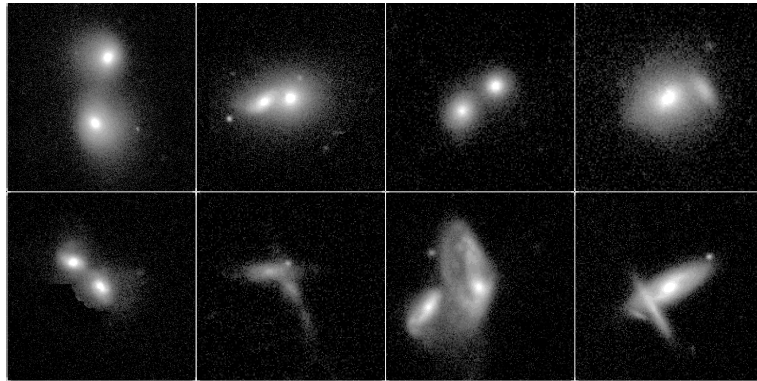


**Figure C8.** *I*-band postage-stamp images of the ZENS galaxy-pairs which are plausibly undergoing a merger.